DESIGN AND ANALYSIS OF OPTICAL WIRELESS COMMUNICATION SYSTEMS UNDER ENERGY CONSTRAINTS

A Dissertation

by

Khadijeh Ali Mahmoodi

Submitted to the
Graduate School of Sciences and Engineering
In Partial Fulfillment of the Requirements for
the Degree of

Doctor of Philosophy

in the
Department of Electrical and Electronics Engineering

Özyeğin University
January 2024

Copyright © 2024 by Khadijeh Ali Mahmoodi

DESIGN AND ANALYSIS OF OPTICAL WIRELESS COMMUNICATION SYSTEMS UNDER ENERGY CONSTRAINTS

Approved by:

Professor Murat Uysal, Advisor
Department of Electrical and Electronics Engineering
Özyeğin University

Assistant Professor Çağatay Edemen
Department of Electrical and Electronics Engineering
Özyeğin University

Associate Professor Evşen Yanmaz Adam
Department of Electrical and Electronics Engineering
Özyeğin University

Assistant Professor Tahsin Yılmaz
Department of Electrical and Electronics Engineering
Istanbul Yeni Yüzyıl University

Date Approved: 28 December 2023

Associate Professor Eylem Erdoğan
Department of Electrical and Electronics Engineering
Istanbul Medeniyet University

I dedicate this dissertation to my beloved husband and son, who have been a continuous source of inspiration. Their consistent support and uplifting energy have played pivotal roles in my personal and academic growth.

ABSTRACT

Optical Wireless Communication (OWC) is a field in communication that employs light waves (i.e.,Light Emitting Diodes (LEDs), or Laser Diodes (LDs)) for wireless data transmission, and provides a Line of Sight (LOS) link with a capacity comparable to fiber optics and much higher than those that can be supported by Radio Frequency (RF) counterparts. In addition, since they operate in optical spectrum, they are immune to interference. Furthermore, unlike RF links which require either area or link license for operation, no licensing fee is required in OWC communication systems.

OWC encompassing sub-branches like Free Space Optical (FSO) and Underwater Optical Wireless Communication (UOWC). FSO uses laser transmitters operating at infrared wavelengths through free space. It specifically offers faster data rates, improved security, and cost-effective connectivity suitable for high-data-throughput applications and scenarios where physical cables or RF networks are impractical. UOWC addresses the limitations of RF and acoustic signals in water, facilitating reliable and high-speed communication for marine applications.

In OWC systems, particularly in underwater and outdoor environments, energy efficiency becomes a critical design criterion due to reliance on batteries with limited capacity, requiring regular and costly recharging or replacement. This dissertation focuses on the significance of energy efficiency in OWC, specifically targeting airborne and underwater networks facing energy resource limitations.

In underwater environments, Underwater Sensor Networks (USNs) are deployed for collaborative tasks such as pollution monitoring, ocean currents analysis, equipment control, and mineral exploration. Sensor nodes are scattered throughout the marine environment, and data is collected at a gateway node, typically a buoy or support vessel. Data

transmission can occur through single-hop or multi-hop routes, with multi-hop transmissions posing the risk of disruptions from individual node failures. In the case of multi-hop data transmission, sensor nodes consume power for data relaying and routing. To address this, the dissertation proposes the utilization of Autonomous Underwater Vehicles (AUVs) for data collection, eliminating the need for data relaying and reducing energy consumption. The proximity of AUV to each sensor node also decreases the power required for their own data transmission. However, AUVs face challenges like latency in data delivery and high-power consumption. The dissertation explores the implementation of efficient trajectories in AUV-assisted data collection within USNs.

Furthermore, the dissertation introduces solar-powered AUVs to further enhance energy efficiency in underwater environments. By incorporating solar panels, AUVs achieve longer endurance, cost-effective operations, and environmentally friendly solutions. We model the energy harvesting from the Sun considering different geographical locations, different days of a year, different times in a day at different depths and types of water including pure see, clear water, coastal water, harbor water to asses the energy harvesting made possible from the Sun in underwater environments. The research addresses the challenge of charging batteries during the day and conducting surveys at night, presenting an optimal Three-Dimensional (3D) trajectory that maximizes energy harvesting and survey efficiency.

In outdoor environments, Unmanned Aerial Vehicles (UAVs) present versatile and cost-effective solutions for communication networks. This study explores both fixed-wing UAVs and rotary-wing UAVs for backhaul connectivity, with a particular emphasis on energy-efficient approaches utilizing solar-powered UAVs. Specifically, solar-powered rotary-wing UAVs are investigated for their potential to enable efficient backhauling in cellular networks, leveraging FSO technology. The dissertation introduces an altitude optimization problem aimed at striking a balance between energy harvesting and consumption. Additionally, the research includes an assessment of High Altitude Platforms (HAPs) which

is a specific type of fixed-wing UAVs operating at high altitudes in the stratosphere layer (17km-20km). The evaluation focuses on analyzing the energy harvesting and consumption aspects of these platforms.

Additionally, to enhance the energy efficiency of airborne networks, laser power beaming is proposed to charge the UAVs/HAPs wirelessly. This technology is gaining attention due to its high efficiency and ability to transfer power over long distances. It involves using powerful laser beams to transfer energy to a receiver equipped with a photovoltaic cell that converts the laser energy into electricity.

In addition to that, to further enhance the efficiency of OWC systems, Simultaneous Lightwave Information and Power Transfer (SLIPT) is investigated. SLIPT utilizes light intensity to transfer both power and data at the same time. By combining power and data transfer in the same OWC link, SLIPT has the potential to enhance the performance and lifespan of the backhaul link.

ÖZETÇE

OWC, iletişim alanında, kablosuz veri iletimi için ışık dalgalarını kullanır (yani, LEDs veya LDs) ve fiber optiklere kıyasla kapasitesi çok daha yüksek ve RF rakipleri tarafından desteklenemeyen bir LOS bağlantısı sunar. Optik spektrumda çalıştıkları müdahaleye karşı bağışıktırlar. Ayrıca, işletim için alan veya bağlantı lisansı gerektiren RF bağlantılarına kıyasla OWC iletişim sistemlerinde lisans ücreti gerekmemektedir.

OWC, FSO ve UOWC gibi alt dalları içerir. FSO, serbest uzayda kızılötesi dalga boylarında çalışan lazer vericilerini kullanır. Özellikle daha hızlı veri hızları, gelişmiş güvenlik ve fiziksel kablolar veya RF ağları uygun olmayan yüksek veri geçişi uygulamaları ve senaryoları için maliyet etkili bağlantı sunar. UOWC, suda RF ve akustik sinyallerin sınırlamalarını ele alarak, deniz uygulamaları için güvenilir ve yüksek hızlı iletişimi kolaylaştırır.

OWC sistemlerinde, özellikle sualtı ve açık hava ortamlarında, enerji verimliliği, sınırlı kapasiteli pillere dayanma gerekliliği nedeniyle kritik bir tasarım kriteri haline gelir ve düzenli şarj veya değiştirme gerektirir. Bu tez, OWC içinde enerji verimliliğinin önemine odaklanır ve özellikle enerji kaynakları sınırlamalarıyla karşılaşan hava ve sualtı ağlarını hedefler.

Sualtı ortamlarda, USNs, kirlilik izleme, deniz akıntıları analizi, ekipman kontrolü işbirliği gerektiren görevler için dağıtılır. Sensör düğümleri deniz çevresine yayılmıştır ve veri genellikle bir kapı düğümünde toplanır, genellikle bir batık veya destek gemisidir. Veri iletimi tek atlamalı veya çoklu atlamalı rotalar aracılığıyla gerçekleşebilir ve çoklu atlamalı iletimler, bireysel düğüm arızalarından kaynaklanan kesinti riskini taşır. Çoklu atlamalı veri iletimi durumunda, sensör düğümleri veri aktarma ve yönlendirme için enerji tüketir. Bu sorunu ele almak için tez, veri iletimi gereksinimini ortadan kaldıran AUVs kullanımını

önerir ve enerji tüketimini azaltır. AUV'lerin her bir sensör düğümüne yakınlığı ayrıca kendi veri iletimleri için gereken enerjiyi azaltır. Ancak, AUVs, veri iletiminde gecikme ve yüksek enerji tüketimi gibi zorluklarla karşılaşır. Tez, USNs içinde AUV destekli veri toplama için verimli rotaların uygulanmasını araştırır.

Ayrıca, sualtı ortamlarında enerji verimliliğini daha da artırmak için güneş enerjisiyle çalışan AUVs tanıtır. Güneş panellerini entegre ederek, AUVs, daha uzun dayanıklılık, maliyet etkili işletmeler ve çevre dostu çözümler elde eder. Güneşten enerji toplamanın mümkün olduğu farklı coğrafi konumlar, yılın farklı günleri, günde farklı saatlerde ve saf deniz, temiz su, sahil suyu, liman suyu gibi farklı su türlerinde modellenir. Araştırma, gündüzleri pilları şarj etme ve geceleri anket yapma zorluğunu ele alır ve enerji toplama ve anket verimini en fazla artıran en uygun 3D rotayı sunar.

Açık hava ortamlarında, UAVs, iletişim ağları için çok yönlü ve maliyet etkili çözümler sunar. Geri bağlantı bağlantısı için sabit kanatlı UAVs ve döner kanatlı UAVs'lerin her ikisini de araştırır ve özellikle güneş enerjisiyle çalışan UAVs'ler kullanarak enerji verimliliği sağlayan yaklaşımlara vurgu yapar. Özellikle, güneş enerjisiyle çalışan döner kanatlı UAVs'ler, hücresel ağlarda verimli geri bağlantı sağlama potansiyelini araştırır ve FSO teknolojisini kullanır. Tez, enerji toplama ve tüketimi arasında denge sağlamayı amaçlayan bir yükseklik optimizasyon sorununu tanıtır. Ayrıca, bu platformların enerji toplama ve tüketim yönlerini analiz eden bir değerlendirmeyi içerir.

Ayrıca, havadaki ağların enerji verimliliğini artırmak için, UAVs/ HAPs kablosuz olarak şarj etmek için lazer enerjisi iletimi önerilir. Bu teknoloji, yüksek verimliliği ve uzun mesafelere enerji iletim yeteneğini kullanması nedeniyle dikkat çekmektedir. Bu, güçlü lazer ışınlarını, lazer enerjisini elektriğe dönüştüren bir fotovoltaik hücre ile donatılmış bir alıcıya kablosuz olarak iletmek anlamına gelir.

OWC bağlantılarının enerji verimliliğini artırmak için SLIPT kullanılabilir. SLIPT, hem güç hem de veri transferini aynı anda kablosuz olarak iletmek için ışık yoğunluğunu kullanır. Güç ve veri transferini aynı OWC bağlantısında birleştirerek, SLIPT, geri bağlantı

bağlantısının performansını ve ömrünü artırma potansiyeline sahiptir.

ACKNOWLEDGEMENTS

I would like to extend my heartfelt gratitude to my advisor, Prof. Murat Uysal, for his invaluable wisdom, friendship, encouragement, support, patient guidance, and insightful suggestions throughout my journey as a PhD student. Without his consistent backing and direction, the completion of this thesis would not have been possible. Working with him has been a truly great opportunity, and I have learned so much from him during my PhD studies.

I express my sincere gratitude to the individuals on my dissertation committee, Assoc. Prof. Evşen Yanmaz, Assoc. Prof. Eylem Erdoğan, Asst. Prof. Çağatay Edemen, and Asst. Prof. Tahsin Yılmaz, for generously dedicating their time to serve on my committee and reviewing my dissertation. Additionally, I am grateful for the productive collaboration and enriching conversations with Asst. Prof. Mohammed Elamassie.

I wish to express my profound appreciation to the European Union's Horizon 2020 research and innovation program for providing funding for my PhD through the Marie Skłodowska Curie grant agreement ENLIGHTEM No. 814215.

I am forever indebted to my loving husband, Mojtaba, and my son, Mehrzad, who have supported me unconditionally throughout my academic journey and for their willingness to stand by me through the challenges and stresses of my endeavors. I also want to lovingly thank my parents for their encouragement and positive energy that has kept me going.

ACRONYMS

AC	Alternating Current
AUV	Autonomous Underwater Vehicle
CdTe	Cadmium Telluride
CIGS	Copper Indium Gallium Selenide
DC	Direct Current
DD	Direct Detection
EH	Energy Harvesting
FSO	Free Space Optical
GA	Genetic Algorithm
GaAs	Gallium Arsenide
HAP	High Altitude Platform
IM	Intensity Modulation
LD	Laser Diode
LED	Light Emitting Diode
LEO	Low Earth Orbit
LOS	Line of Sight
OWC	Optical Wireless Communication
PAT	Pointing-acquisition-tracking
PD	Photodiode
PDF	Probability Density Function
QoS	Quality of Service
RF	Radio Frequency
RL	Reinforcement Learning

SLIPT	Simultaneous Lightwave Information and Power Transfer
TSP	Travelling Salesman Problem
2D	Two-Dimensional
3D	Three-Dimensional
UAV	Unmanned Aerial Vehicle
USN	Underwater Sensor Network
UOWC	Underwater Optical Wireless Communication
VLC	Visible Light Communication
VoI	Value Of Information
VTOL	Vertical Takeoff and Landing

TABLE OF CONTENTS

DEDICATION . . . . . **iii**

ABSTRACT . . . . . **iv**

ÖZETÇE . . . . . **vii**

ACKNOWLEDGEMENTS . . . . . **x**

ACRONYMS . . . . . **xi**

LIST OF TABLES . . . . . **xvi**

LIST OF FIGURES . . . . . **xvii**

LIST OF ALGORITHMS . . . . . **xix**

I INTRODUCTION **1**

1.1 Potential Solutions For Energy Management 6

II ENERGY HARVESTING TECHNIQUES **9**

2.1 Introduction 9

2.2 Energy Harvesting From the Sun 9

2.2.1 Energy Harvesting Model in Outdoor Environments 10

2.2.2 Results and Discussions 14

2.2.3 Energy Harvesting Model in Underwater Environments 19

2.2.4 Results and Discussions 21

2.3 Energy Harvesting From Laser Power Beaming 25

2.3.1 Results and Discussions 28

2.4 Energy Harvesting From SLIPT 30

2.4.1 Results and Discussions 31

2.5 Extended Operation Time of the Autonomous Vehicles (AUVs/UAVs/ HAPs) 33

III ENERGY MANAGEMENT SOLUTIONS IN UOWC SYSTEMS **36**

3.1 Introduction 36

3.2 Two-Dimensional (2D) Trajectory Optimization of AUVs 37
3.2.1 Motion Model 39
3.2.2 Energy Consumption Model 40
3.2.3 Communication Model 41
3.2.4 Optimization Problem Formulation 42
3.2.5 Results and Discussions 43
3.3 3D Trajectory Optimization of Solar Powerered AUVs 47
3.3.1 Motion Model 49
3.3.2 Energy Consumption Model 52
3.3.3 Communication Model 53
3.3.4 Optimization Problem Formulation 54
3.3.5 Results and Discussions 59
IV ENERGY MANAGEMENT SOLUTIONS IN AIRBORNE NETWORKS . 68
4.1 Introduction 68
4.1.1 Rotary-Wing UAVs 68
4.1.2 Fixed wing UAVs and HAPs 69
4.2 Rotary-Wing UAV Based Communication Systems 70
4.2.1 Energy Consumption Model 73
4.2.2 Communication Model 76
4.2.3 Optimization Problem Formulation 77
4.2.4 Results and Discussions 78
4.2.5 Comprehensive Energy Assessment of Solar Powered UAVs . . . 83
4.3 HAP Based Communication Systems 89
4.3.1 Energy Consumption Model 91
4.3.2 Communication Model 94
4.3.3 Comprehensive Energy Assessment of Solar Powered HAPs . . . 96
V CONCLUSIONS AND FUTURE WORK 106
5.1 Conclusions 106

5.2 Future Work 107

REFERENCES **110**

VITA **120**

LIST OF TABLES

1 Parameters for calculating Energy Harvesting (EH) from the Sun by the UAV/HAP 14

2 Parameters for calculating EH from the Sun by the AUV 21

3 Parameters for Calculating EH from Laser Power Beaming 28

4 System and channel parameters 43

5 Specifications of the AUV 44

6 Flowchart for the proposed EH-aware trajectory planning algorithm 58

7 System and channel parameters 60

8 Specifications of the solar-powered AUV 60

9 Sensor locations 64

10 Specifications of the solar-powered rotary-wing UAV 79

11 Air density variables 79

12 Energy consumption of rotary-wing UAV 86

13 Specifications of the solar-powered HAP 96

14 Energy consumption of a m=75kg HAP in different modes 102

15 Energy consumption of a m=300kg HAP in different modes 103

LIST OF FIGURES

1 The relative location of the sun with respect to the earth. 11

2 Different locations of interest. 15

3 Factors impacting the amount of energy harvested by the UAV/HAP (a) Maximum elevation angle, (b) Maximum instantaneous radiation intensity. . 15

4 Daylight duration for the representative climate types 16

5 Instantaneous radiation intensity with respect to time ($d = 150^{\text{th}}$ day of the year is assumed) 17

6 Harvested energy from the Sun in different days of the year in climate type of (a) Tropical, (b) Subarctic, (c) Midlatitude. 18

7 Solar irradiance and various effects on it in its way of reaching the destination. 20

8 Hourly variation of harvested power on the sea surface for different days in climate type of (a) Tropical, (b) Subarctic, (c) Midlatitude. 23

9 Average amount of harvested power with respect to depth for different water types on (a) 1^{st} day, (b) 90^{th} day, (c) 180^{th} day, (d) 270^{th} day of the year. 24

10 Laser Power Beaming and SLIPT for powering airborne nodes. 25

11 Energy harvested using laser power beaming by a rotary wing UAV at an altitude of (a) $h = 100\,\text{m}$, and (b) $h = 5\,\text{km}$ 28

12 Energy harvested by a HAP using laser power beaming. 29

13 Energy harvested by rotary wing UAV using SLIPT at an altitude of (a) $h = 100\,\text{m}$, and (b) $h = 5\,\text{km}$ 32

14 Energy harvested by HAP using SLIPT at an altitude of $h = 20\,\text{km}$. 33

15 AUV-assisted USN 40

16 AUV trajectories for uniformly distributed sensors: a) Straight trajectory (i.e., only large-scale optimization), b) Optimum trajectory. 44

17 AUV trajectories for randomly distributed sensors: a) Straight trajectory (i.e., only large-scale optimization), b) Optimum trajectory. 45

18 Effect of the number of sensor nodes on the mission time and energy consumption 46

19 Effect of AUV velocity on the mission time and energy consumption (Only optimal trajectory is considered.) 47

20 Solar powered AUV assisted USN under consideration. 50
21 Operation modes of AUV. 51
22 (a) Optimal 3D EH-aware trajectory, (b) Benchmarking 2D trajectory. . . . 61
23 Consumed, harvested and net energy levels over the mission duration (a) optimal 3D trajectory, (b) benchmark 2D trajectory. 63
24 Effect of velocity on the harvested energy, consumed energy, and net energy. 65
25 Comparison of net energy levels for different operation days under consideration in (a) Tropical, (b) Subarctic, and (c) Mid-latitude climate types. . . 66
26 LOS link between the solar-powered rotary-wing UAV and the ground base station in an urban area. 72
27 Probability of LOS with respect to the altitude of the UAV 80
28 Net energy with respect to altitude for rotary-wing UAVs with different weights. 81
29 Optimum altitude versus UAV weight for different values of solar panel efficiency. 82
30 Optimum altitude versus solar panel size for different values of solar panel efficiency. 83
31 Percentage of power distribution of rotary wing UAV in (a) Ascending, (b) straight and level, and (c) hovering flight status. 85
32 Distribution of energy consumption in vertical ascent flight, straight and level flight and hovering in different modes of operation. 87
33 Circular trajectory of HAPs while providing backhauling connectivity. . . . 92
34 HAP-based FSO communications system. 95
35 Percentage of power distribution of m=300kg HAP in (a) Ascending, (b) straight and level, and (c) circular flight status. 97
36 Percentage of power distribution of m=75kg HAP in (a) Ascending, (b) straight and level, and (c) circular flight status. 98
37 Energy consumption of the HAP in steady climb flight with respect to velocity (a) m=75kg, (b) m=300kg. 100
38 Energy consumption of the HAP in straight level flight with respect to velocity (a) m=75kg, (b) m=300kg. 101
39 Energy consumption of the HAP in circular flight with respect to velocity . 102
40 Distribution of energy consumption in three phases of flight of the HAP . . 103

LIST OF ALGORITHMS

1 Total Operation Time Calculation with Continuous Power Harvesting . . . 34

CHAPTER I

INTRODUCTION

Optical wireless communication (OWC) is a rapidly advancing field that utilizes light waves, such as LEDs or LDs, for wireless data transmission [1]. These innovative systems offer a line-of-sight (LOS) link with data capacity comparable to fiber optics, far surpassing the capabilities of traditional RF counterparts. Notably, OWC boasts immunity to interference due to its operation in the optical spectrum, providing a reliable and secure communication medium. Moreover, the absence of costly licensing fees and extensive regulatory requirements makes OWC systems attractive for a broad range of applications [2].

OWC technology finds utility in diverse environments, including indoor, outdoor, and underwater scenarios. FSO, a prominent sub-branch of OWC, utilizes laser transmitters operating at infrared wavelengths enabling high-speed data transfer through free space. It excels in delivering faster data rates, improved security, and cost-effective connectivity, making it especially suitable for situations where physical cables or RF networks are impractical or challenging to deploy [3]. In contrast, UOWC addresses the limitations of conventional RF and acoustic signals in underwater environments, unlocking the potential for reliable and high-speed communication in various marine applications [4].

In underwater environments, USNs play a pivotal role in collaborative tasks, ranging from pollution monitoring and ocean currents analysis to equipment control and mineral exploration [5]. Strategically deployed sensor nodes throughout the marine environment relay data to a gateway node, typically a buoy or support vessel. Data transmission may occur through single-hop or multi-hop routes, with the latter introducing the risk of disruptions caused by individual node failures [6]. AUVs are employed for data acquisition in USNs to ensure uninterrupted communication and extended operational lifespans for

sensor nodes. This is achievable as AUVs can approach each sensor node closely for data collection, thereby minimizing energy transmission from the nodes.

In AUV operations, the major limiting constraint is energy consumption since they rely on batteries with limited capacity. Therefore, the choice of efficient trajectories directly impacts the mission time of AUVs, which directly affects the energy consumption of AUVs and their endurance. Predefined trajectories, as the name implies, are planned before the AUV starts its mission. In previous studies [7–10], elliptical, circular, and lawnmower patterns were investigated as predefined AUV trajectories in acoustic USNs. However, the energy efficiency of predefined trajectories remains low, particularly for large mission areas with randomly distributed sensor nodes. Another choice is reactive trajectories, where the AUV path is corrected in real-time and refined to cope with sudden changes during the operation. In the literature, there have been works on reactive trajectory optimization assuming both acoustic [11–14] and Visible Light Communication (VLC) [15] signaling. Trajectory planning is formulated as a Travelling Salesman Problem (TSP) to minimize AUV travel time in some studies [11, 12], while in others [13, 14], the TSP algorithm is proposed to define the path of the AUV with the objective of maximizing the Value Of Information (VoI) from the sensors. In another work [15], the trajectory finding problem of the AUV is solved using a greedy algorithm under VoI constraints. However, these studies assume that the AUV follows a straight path between each two sensor nodes without any deviations, neglecting real-life conditions such as ocean currents. Trajectory optimization of stand-alone AUVs in the presence of ocean currents has been addressed [16–18], but these focus on AUVs moving from a pre-defined start point to an endpoint and do not consider the distribution of sensors in USN or signaling aspects between the AUV and the sensor.

In addition to the trajectory design, energy consumption of AUVs is influenced by the type of deployed AUV. Propelled AUVs can reach higher speeds, but their power consumption can be large due to the continuous use of propeller engines [19]. In contrast,

non-propelled AUVs (gliders) use little to no power but operate at much lower speeds [20]. Floating up and diving in operations in non-propelled AUVs are also possible by changing their buoyancy with little power consumption [21]. Hybrid versions [22] use their buoyancy engine for floating up and diving and their propeller engine for going forward. In the operation of AUVs, the main power consumption source is therefore the propeller engine, making the choice of trajectories directly impact mission time and energy consumption.

In an effort to enhance the energy efficiency of AUV-aided USNs, solar-powered AUVs have been proposed for long-term deployments to address the energy limitations of battery-powered counterparts [23]. They can harvest power from sunlight and use the harvested power to perform the mission or store it for later use. In the current literature [23, 24], it is commonly assumed that the solar-powered AUV resurfaces during daylight hours and recharges its batteries using solar energy on the water surface while conducting its assigned mission during the nighttime hours. However, recent progress in solar cell technology enables efficient harvesting of sunlight for submerged nodes [25]. This makes it possible for solar-powered AUVs to harvest energy during their mission.

Similarly, in outdoor environments, airborne vehicles, including both fixed-wing UAVs and rotary-wing UAVs, present a wealth of opportunities in surveillance, monitoring, data collection, wireless communications, and disaster management. Their inherent capabilities, such as rapid deployment, high mobility, and adaptive altitude, make them promising candidates for future airborne backhaul communication infrastructures [26]. In the realm of airborne networks, there has been a surge of interest, as evidenced by recent papers on airborne networks [27–29]. These papers have delved into various aspects of airborne networks, including network topology, routing protocols, and security. However, one critical factor that has been conspicuously absent from these discussions is energy efficiency, a paramount consideration that can profoundly impact the operational capabilities of airborne networks. Since, airborne wireless networks demand a continuous and reliable supply of energy to remain functional during flight.

Rotary wing UAVs can be equipped with a radio base station and deployed as an aerial base station providing wireless access to end users [30–33]. For example, in [30], optimum 3D deployment of multiple UAV base stations is investigated with the goal of improving the coverage rate while satisfying the Quality of Service (QoS) requirements of each user. In [31], an aerial base station placement algorithm is proposed to reduce the number of required UAVs to serve a desired coverage area. In [32], optimum UAV trajectory design is investigated to minimize its mission completion time while ensuring that each ground node receives the required information within a given time. In [33], 3D trajectory optimization of multiple UAVs is pursued with the goal of optimizing the coverage while maximizing the sum of QoSs requirements of ground users.

In addition to the line of research on UAV-based wireless access discussed above, it is also possible to utilize UAVs as backhaul links to the ground base station. Rotary-wing UAVs have the capability of hovering and might be particularly attractive for small cell backhauling. They can be positioned as a complementary solution to terrestrial backhaul links in dense areas with high-peak traffic demands. For UAV-based backhauling, the operation frequency can be selected from RF band [34–36] or optical band (in particular, infrared) [26, 37–39].

In [37], with the goal of minimizing the capital cost of the FSO-based aerial backhaul network, the problem of minimizing the number of UAVs is investigated. In [38], to improve the energy efficiency of the UAV-based backhaul networks, a hybrid RF-FSO system is proposed with simultaneous harvesting capability. In [39], to improve the energy efficiency of the UAV-based backhaul networks, a modulating retro-reflector based FSO system is proposed which leads to an increase in the maneuverability and flight time of UAVs. In [40], solar-powered rotary-wing UAVs are considered, and the problem of UAV placement in a dense urban environment is investigated to ensure backhaul connectivity. To maximize the harvested energy, the UAVs are placed in sunny spots between the buildings. In an urban area with many buildings, the operation altitude of a solar-powered UAV plays

an important role in the energy efficiency of the aerial backhaul link. It has a significant effect on the endurance of the solar-powered UAV (which can be quantified in terms of net energy defined as the difference between energy consumption and harvesting) as well as the probability of establishing the LOS link. Some earlier works on RF-based UAV backhauling discussed the optimal selection of altitude. For example, in [35], a mathematical model is presented to determine an optimal altitude with the goal of providing maximum radio coverage on the ground assuming an in-band frequency of 2 GHz. In [41], optimal altitude is selected to maximize the coverage area for a targeted outage probability.

Recent advances in autonomous avionics and the development of lightweight composite materials have ushered in a new era in the realm of aerial technology. Among the remarkable innovations born of these advancements are HAPs [42]. These fixed-wing UAVs are poised at the forefront of modern aviation, operating at altitudes between 17 and 22 kilometers, comfortably nestled within the stratospheric layer. This altitude range adopted for the HAP's operation is motivated by the fact that in this altitude, the wind speed is less intense, and as a consequence, the HAP requires less power to maintain position. Compared to their rotary-wing UAV counterparts, which predominantly cover lower and middle altitudes, typically up to a few kilometers, HAPs have captured the imagination of the aerospace community for several compelling reasons. One of their most striking attributes is their potential to deliver significantly lower latency and higher data rate capacity per unit area, making them an appealing alternative to traditional Low Earth Orbit (LEO) satellites.

In light of the challenges and solutions provided above, this dissertation endeavors to emphasize the profound significance of enhancing energy efficiency in OWC networks, with a specific focus on applications in both airborne and underwater domains. By addressing the energy resource limitations faced in these environments, this research aims to pave the way for more sustainable and resilient communication systems. To this end, we aim to explore innovative approaches and methodologies to achieve these essential energy efficiency goals in OWC systems.

1.1 Potential Solutions For Energy Management

To address the critical challenge of energy efficiency in OWC networks, various innovative solutions have been proposed. These solutions aim to harvest energy from external power sources, optimize the trajectories of autonomous vehicles (i.e., UAVs and AUVs) involved in these networks under communications constraints. In this section, we present some potential solutions that pave the way for sustainable and energy-efficient OWC networks as follows

- **Energy Harvesting from External Sources:** One promising approach to enhance energy efficiency in autonoumous vehicles involved in OWC networks (i.e., UAVs and AUVs) is to harvest energy from external power sources wirelessly. Solar-powered UAVs have demonstrated remarkable potential in extending mission endurance by capturing solar energy during daylight hours [43]. By integrating solar panels into their design, these vehicles can recharge their batteries while in flight, reducing reliance on traditional power sources. Similarly, for underwater applications, underwater solar panels can be employed to harvest sunlight, providing a continuous energy supply to AUVs during their missions [44].

  Laser power beaming is another promising energy harvesting technique in the realm of OWC systems [45]. It involves deploying high-power lasers to wirelessly transmit energy to the OWC systems, especially for charging airborne vehicles. By adopting this innovative approach, airborne vehicles can maintain prolonged operational capabilities without the burden of frequent battery replacements, enhancing their endurance and mission efficiency [46]. The fundamental principle of laser power beaming revolves around converting light energy into electrical power. Powerful lasers are directed from a centralized location towards airborne vehicles equipped with specialized photovoltaic receivers. These receivers efficiently capture the incoming laser energy and convert it into electrical power, directly replenishing the vehicles' onboard

batteries. One of the key advantages of laser power beaming is its ability to achieve long-range power transfer with minimal energy losses, making it highly suitable for OWC systems operating over vast distances.

Furthermore, SLIPT is an innovative technology that holds great promise for energy harvesting in OWC systems. By integrating specialized photovoltaic cells within the communication system, SLIPT enables the OWC network to harvest energy from the light signals used for data transmission [47]. This approach not only facilitates efficient data communication but also empowers the system to become more self-sufficient by capturing energy simultaneously. This enhanced energy sustainability is particularly valuable in scenarios where access to external power sources is limited, offering a more autonomous and greener solution for OWC systems [48].

- **Trajectory Optimization for Improving Energy Efficiency:** Optimizing the trajectory of autonomous vehicles plays a crucial role in minimizing their energy consumption [49]. For AUVs in underwater sensor networks, trajectory optimization techniques in both 2D and 3D environments can significantly improve energy efficiency while considering communication constraints [50,51]. By identifying energy-efficient paths, AUVs can navigate efficiently through underwater environments, reducing power consumption and extending mission durations. Similarly, for UAVs in outdoor environments, optimizing parameters like flight altitude can lead to substantial gains in energy efficiency. By identifying the optimal operation altitude specifically for solar powered UAVs, they can reduce energy consumption while maximizing solar energy harvesting. This approach ensures that solar powered UAVs can maintain longer missions and perform tasks in a more sustainable manner [52].

In summary, improving energy efficiency in underwater and airborne networks requires innovative approaches that harvest energy from external sources and optimize vehicle trajectories. By harnessing solar energy, utilizing laser power beaming, and exploring SLIPTs

techniques, UAVs and AUVs can achieve longer and more sustainable missions. Additionally, trajectory optimization strategies for both AUVs and UAVs enable energy-efficient operations, reducing their environmental impact and contributing to the advancement of airborne communication technologies.

CHAPTER II

ENERGY HARVESTING TECHNIQUES

2.1 Introduction

A persistent obstacle in the implementation of OWC systems has been the constrained accessibility of power sources in remote outdoor settings and underwater environments. Improving energy efficiency of these networks is critical to the sustainable operation of OWC systems, particularly in scenarios where constant power supply may be impractical or cost-prohibitive. To address this challenge, we have explored various energy harvesting techniques. These techniques harness energy from external sources to supplement or replace conventional power sources, thereby improving the overall energy efficiency and sustainability of OWC systems.

In this chapter, we delve into three prominent energy harvesting techniques that hold immense potential for enhancing the energy efficiency of OWC systems. These techniques include: Solar Energy Harvesting, Laser Power Beaming, and SLIPT.

Each of these energy harvesting techniques has the potential to make OWC systems more resilient, efficient, and sustainable. In the following subsections, we delve deeper into each technique, discussing real-world applications in both outdoor and underwater settings.

2.2 Energy Harvesting From the Sun

Recent developments in solar cell technology have made it possible to capture more energy from the sun than ever before. Solar cells have undergone three generations of development for optimizing their energy efficiency, reducing their cost, and their flexibility. The first generation of solar cells is made of single-crystalline and multi-crystalline silicon,

which are still the most used types in applications where space is limited, such as rooftops or small-scale solar projects. Polycrystalline solar cells, on the other hand, have efficiencies ranging from around 13 percent to 16 percent. They are made from multiple silicon crystals and are generally less expensive to produce than monocrystalline cells. Polycrystalline cells are often used in large-scale solar projects, where cost is a major consideration [53]. Second-generation solar cells are made of thin-film materials such as Gallium Arsenide (GaAs), Cadmium Telluride (CdTe), and Copper Indium Gallium Selenide (CIGS). These materials have several advantages over silicon, including higher efficiency in low-light conditions, and the ability to be deposited onto flexible or lightweight substrates. However, they are more expensive to produce and are typically used in space satellites, military operations, or remote or off-grid locations where traditional power sources may not be available. The third generation consists of amorphous, dye-sensitized, organic/polymer, and hybrid organic-inorganic substances such as the perovskite-based solar cells, which are lightweight, flexible, and can be manufactured at a lower cost than traditional silicon-based solar cells [54]. Amongst all, GaAs solar cells are one such development that is rapidly gaining attention [55]. GaAs is a second-generation solar cell material that has advantages over some third-generation materials, including high efficiency (up to 40 percent), stability, and durability over time, and good performance in low light conditions. As a result, GaAs solar cells are rapidly gaining attention, particularly for use in airborne and underwater networks where high efficiency, durability, and lightweight properties are critical.

In general, there are various factors that can affect energy harvesting from the Sun, including the size of the solar panel, its efficiency, and its altitude from the sea level, day of the year, time in the day, and geographical location.

2.2.1 Energy Harvesting Model in Outdoor Environments

In this section, we provide the necessary concepts to model the energy harvested by the solar panel which can be attached to the UAVs, or HAPs. The intensity of solar radiation

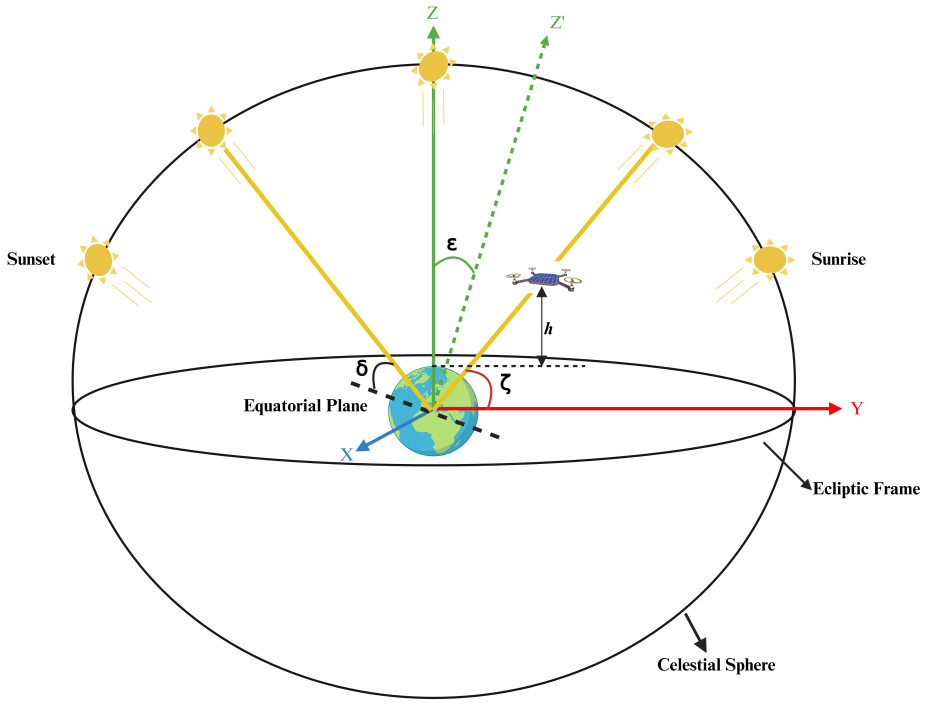


Figure 1: The relative location of the sun with respect to the earth.

on a horizontal surface is dependent on the latitude of the geographical location and the position of the sun in the sky.

As illustrated in Figure 1, X, Y, and Z are coordinates axes at an observation point on earth. The earth orbits the Sun on a particular angle and its orbit is elliptical in shape. The ecliptic frame describes the plane of the earth's orbit. The earth rotates around an axis Z' tilted towards the ecliptic of the Sun by an angle of $\varepsilon = 23.44°$ known as axial tilt [56]. The celestial sphere is an imaginary sphere of an arbitrary large radius concentric with earth. It helps us visualize the motion of celestial bodies in the entire sky including the motion of the Sun in relation to the earth. In other words, it visualizes the movement of the Sun in relation to the earth which creates days and nights. In the figure, ξ is the solar elevation angle and represents the measurement of the height of the sun in the sky. δ is known as solar declination angle and represents the angle between the line joining the centres of the sun and the earth and its projection on the equatorial plane. h is the altitude of the UAV. The maximum instantaneous radiation intensity at solar noon (Solar noon is the moment

when the Sun reaches its highest position in the sky) is given by

$$G_{\mathrm{m}} = G_{\mathrm{sc}}\left(1+0.033\cos\left(\frac{360d}{365}\right)\right)\times\left(\sin\left(\xi_{\mathrm{m}}+\delta\right)\cos\left(\delta\right)-\cos\left(\xi_{\mathrm{m}}+\delta\right)\sin\left(\delta\right)\right), \tag{2.1}$$

where d is the specific day of the year. In Eq. (2.1), δ is the solar declination angle and is given by

$$\delta = -23.45\times\cos\left(\frac{360}{365}\left(10+d\right)\right), \tag{2.2}$$

In Eq. (2.1), ξ_{m} is the maximum elevation angle of the sun. It depends on the latitude of the location of interest L, and varies with day of the year. It is given by $\xi_{\mathrm{m}} = 90^{\circ}+L-\delta$.

Let η_{sc} and A_{s} respectively denote the efficiency and the area of the solar panel attached to the UAV/HAP. If the airborne duration is T hours, the total harvested energy (in Watt-hour) is given by [57]

$$E_{\mathrm{h}} = \int_{t=t_{\mathrm{start}}}^{t_{\mathrm{start}}+T} \psi A_{\mathrm{s}}\eta_{\mathrm{sc}}G_{\mathrm{in}}\left(t\right)dt, \tag{2.3}$$

where t_{start} is the start time of the flight. In Eq. (2.3), $G_{\mathrm{in}}\left(t\right)$ is the instantaneous solar intensity and given by [57]

$$G_{\mathrm{in}}\left(t\right) = \begin{cases} G_{\mathrm{m}}\cos\left(\dfrac{\pi}{2}-\dfrac{2\xi_{\mathrm{m}}}{\tau}\left(t-t_{\mathrm{sunrise}}\right)\right), & t_{\mathrm{sunrise}} < t < 12 \\ G_{\mathrm{m}}\cos\left(\dfrac{\pi}{2}-\left(2\xi_{\mathrm{m}}-\dfrac{2\xi_{\mathrm{m}}}{\tau}\left(t-t_{\mathrm{sunset}}\right)\right)\right), & 12 < t < t_{\mathrm{sunset}} \end{cases}, \tag{2.4}$$

where τ is the daylight duration in hours, which is given by

$$\tau = 24\left(1-\frac{1}{\pi}\cos^{-1}\left(\tan\left(L\right)\right)\times\left(\frac{\sin\left(\varepsilon\right)\sin\left(\varphi\right)}{\sqrt{1-\sin^{2}\left(\varepsilon\right)\sin^{2}\left(\varphi\right)}}\right)\right), \tag{2.5}$$

where φ is the azimuthal angle of the sun. It is calculated as

$$\varphi = -1.3411+M+0.0334\sin\left(M\right)+0.0003\sin\left(2M\right) \tag{2.6}$$

where M is the mean anomaly and is calculated as a function of the day as $M = -0.041+0.017202d$. In Eq. (2.6), $t_{\mathrm{sunrise}} = 12-\tau/2$ is the time when the sun rises, and $t_{\mathrm{sunset}} = 12+$

$\tau/2$ is the time when the sun sets. In Eq. (2.3) on the previous page, ψ is the atmospheric transmittance, which varies with respect to altitude and is calculated by [58]

$$\psi = 0.8978 - 0.2804 \exp\left(-\frac{h}{3500}\right). \tag{2.7}$$

Assume that the UAV/HAP becomes airborne $T/2$ hours before solar noon which is typically observed at 12:00 pm, i.e., $t_{\text{start}} = 12 - T/2$. By substituting Eq. (2.4) on the preceding page in Eq. (2.3) on the previous page and solving the resulting integral, we find the harvested energy as

$$\begin{aligned} E_{\text{h}} = & \frac{180\tau\psi A_{\text{s}}\eta_{\text{sc}}G_{\text{m}}}{\xi_{\text{m}}\pi} \\ & \times \left[\cos\left(\frac{2\xi_{\text{m}}}{\tau}\left(12 - t_{\text{sunset}}\right)\right)\left(\cos\left(\frac{\xi_{\text{m}}}{\tau}T\right) - 1\right) + \sin\left(\frac{2\xi_{\text{m}}}{\tau}\left(12 - t_{\text{sunrise}}\right)\right)\sin\left(\frac{\xi_{\text{m}}}{\tau}T\right)\right]. \end{aligned} \tag{2.8}$$

If the mission spans the whole day, the harvested energy takes the form of

$$E_{\text{in}} = \int_{t=t_{\text{sunrise}}}^{t_{\text{sunset}}} A_{\text{s}}.\eta_{\text{sc}}.G_{\text{in}}(t).dt \tag{2.9}$$

Substituting Eq. (2.4) on the preceding page into Eq. (2.9), we have

$$\begin{aligned} E_{\text{in}} = & \int_{t=t_{\text{sunrise}}}^{12} \left(A_{\text{s}}.\eta_{\text{sc}}.G_{\text{m}}\cos\left(\frac{\pi}{2} - \frac{2\xi_{\text{m}}}{\tau}\left(t - t_{\text{sunrise}}\right)\right)\right)dt \\ & + \int_{t=12}^{t_{\text{sunset}}} \left(A_{\text{s}}.\eta_{\text{sc}}.G_{\text{m}}\cos\left(\frac{\pi}{2} - \left(2\xi_{\text{m}} - \frac{2\xi_{\text{m}}}{\tau}\left(t - t_{\text{sunset}}\right)\right)\right)\right)dt \end{aligned} \tag{2.10}$$

Integrating the triangular function over the entire range t_{sunrise} to t_{sunset} is equivalent to integrating only over half, e.g., $t_{\text{sunrise}} - 12$, and multiplying the result by 2. Therefore, Eq. (2.10) can be simplified as follows

$$E_{\text{in}} = 2A_{\text{s}}\eta_{\text{sc}}G_{\text{m}} \int_{t=t_{\text{sunrise}}}^{12} \cos\left(\frac{\pi}{2} - \frac{2\xi_{\text{m}}}{\tau}\left(t - t_{\text{sunrise}}\right)\right)dt \tag{2.11}$$

Table 1: Parameters for calculating EH from the Sun by the UAV/HAP

Parameter	**Variable**	**Value**
Solar Area of the UAV/HAP	$\mathrm{A_s}\ \left(\mathrm{m}^2\right)$	4/76
Solar Constant	$G_{\mathrm{sc}}\ \left(\mathrm{W/m}^2\right)$	1366.1
Efficiency of the Solar Cell	η_{sc} (%)	37.5
Mission Time of the UAV/HAP	T (hour)	1/24

Solving the integral in Eq. (2.11) on the previous page yields the harvested energy for the whole day

$$E_{\mathrm{in}} = \frac{A_{\mathrm{s}}\eta_{\mathrm{sc}}G_{\mathrm{m}}\tau}{\xi_{\mathrm{m}}}\left(1-\cos\left(\xi_{\mathrm{m}}\right)\right) \tag{2.12}$$

2.2.2 Results and Discussions

To assess the energy harvested by the solar-powered rotary wing UAV/HAP, we consider three climate types including tropical (also known as equatorial, which is close to the equator), mid-latitude (which is a spatial region on earth located between the latitudes of $L = 23^\circ$ and $L = 66^\circ$ in the north and between the latitudes of $L = -23^\circ$ and $L = -66^\circ$ in the south polar region of earth), and subarctic (region in the northern hemisphere near the arctic ocean). Unless otherwise stated system parameters are provided in Table 1.

We consider three representative locations for different climate types under consideration as shown in Figure 2 on the next page.

Namely, we consider

- Ankara, Turkey with the latitude of $L = 39.86^\circ$ (representative of mid-latitude climate type),
- Kuala Lumpur, Malaysia with the latitude of $L = 3.11^\circ$ (representative of tropical climate type), and
- Victoria Island, Canada with the latitude of $L = 70.8^\circ$ (representative of subarctic climate type).

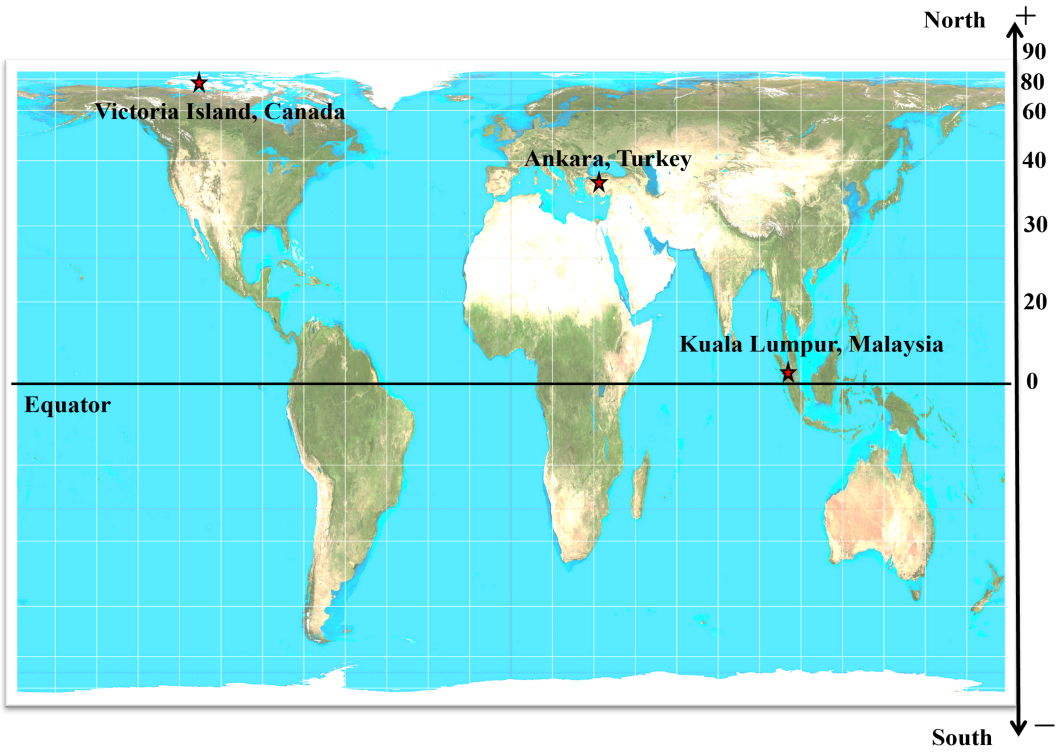
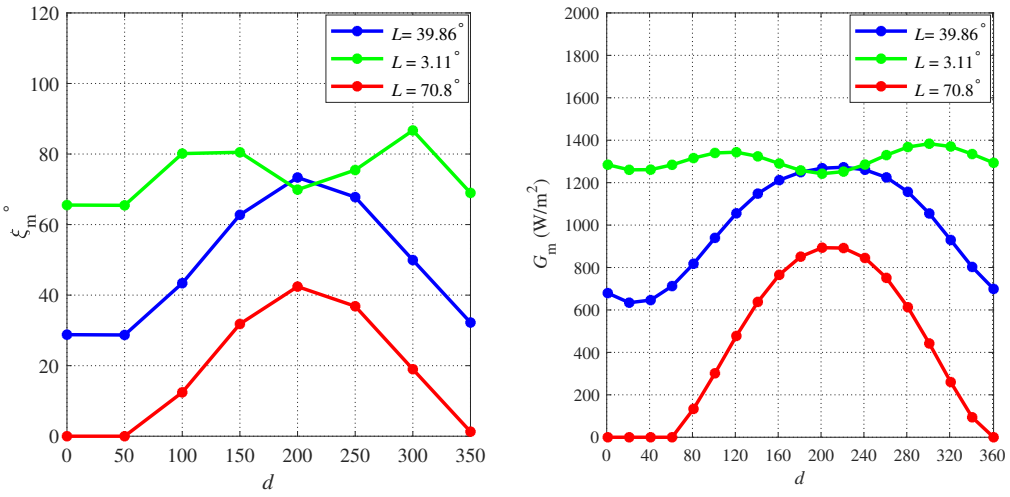


Figure 2: Different locations of interest.



(a) (b)

Figure 3: Factors impacting the amount of energy harvested by the UAV/HAP (a) Maximum elevation angle, (b) Maximum instantaneous radiation intensity.

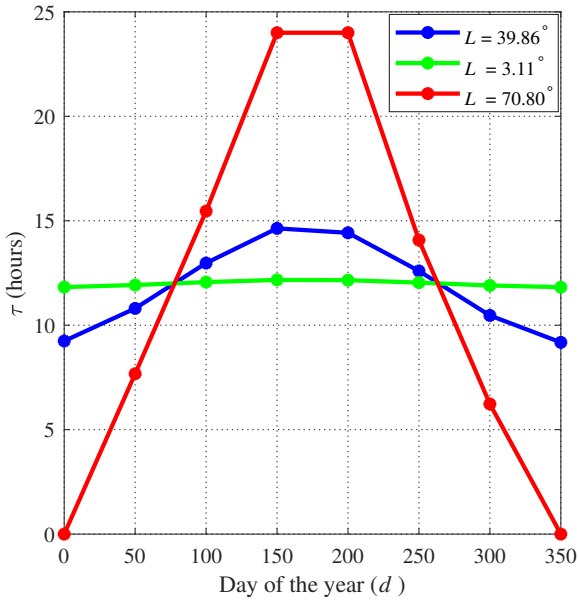


Figure 4: Daylight duration for the representative climate types .

Two most important factors that impact energy harvesting from the Sun based on the latitude of the location of interest and different days of the year include the maximum elevation angle of the sun, ξ_{m} illustrated in Fig. 3(a) on the preceding page, and the maximum instantaneous radiation intensity, G_{m} depicted in Fig. 3(b) on the previous page obtained from Eq. (2.1) on page 12.

Based on Eq. (2.5) on page 12, Fig. 4 illustrates the daylight duration in different days of a year and for the representative climate types. It can be readily seen from the figure that the daylight duration is highly dependent on the climate type and the specific day in the year. For example, on $d = 150^{\mathrm{th}}$ day of the year, the maximum daylight duration is $\tau = 14.64$, $\tau = 12.17$, and $\tau = 24$ hours for midlatitude, tropical, and subarctic climate types, respectively. Whereas, on $d = 350^{\mathrm{th}}$ day of the year, the daylight duration for midlatitude, tropical, and subarctic is $\tau = 9.17$, $\tau = 11.82$, and $\tau = 0$ hours, respectively. Moreover, it is obvious from the figure that the daylight duration does not face a significant change in tropical climate type, and it is around $\tau = 12$ hours during the whole year.

Based on Eq. (2.4) on page 12, Fig. 5 on the following page shows the instantaneous

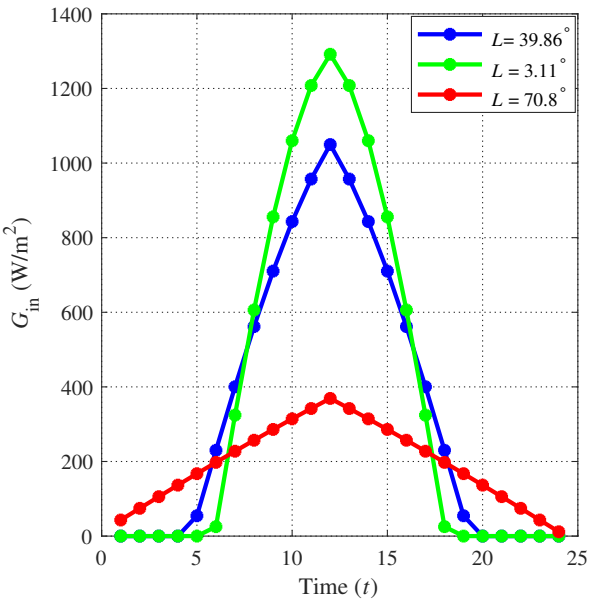


Figure 5: Instantaneous radiation intensity with respect to time ($d = 150^{\text{th}}$ day of the year is assumed)

solar intensity with respect to time in a day on $d = 150^{\text{th}}$ day of the year and in the three climate types under consideration. Note that the corresponding maximum instantaneous radiation intensity is given by $G_{\text{m}} = 1049.6\,\text{W/m}^2$, $G_{\text{m}} = 1291.67\,\text{W/m}^2$, and $G_{\text{m}} = 369\,\text{W/m}^2$ for midlatitude, tropical, and subarctic climate types, respectively which can be observed at $t = 12$.

Using a GaAs solar panel with an efficiency of $\eta_{\text{sc}} = 37.5\%$ and at the mentioned geographical location in midlatitude, subarctic, and tropical climate types, Fig. 6 on the next page illustrates the energy harvesting by the airborne nodes on different days of the year. The HAP has a solar panel of the size of $\text{A}_{\text{s}} = 76\text{m}^2$ attached to its wings, whereas the rotary wing UAV has a solar panel of the size of $\text{A}_{\text{s}} = 4\text{m}^2$. The mission time for the rotary wing UAV is considered to be $T = 1$ hour and for the HAP, it is assumed to be $T = 24$ hours. The energy harvesting for the rotary wing UAV is shown for two altitudes $h = 100$m and $h = 5$km.

According to Fig. 6 on the following page, in midlatitude climate type on March 20th

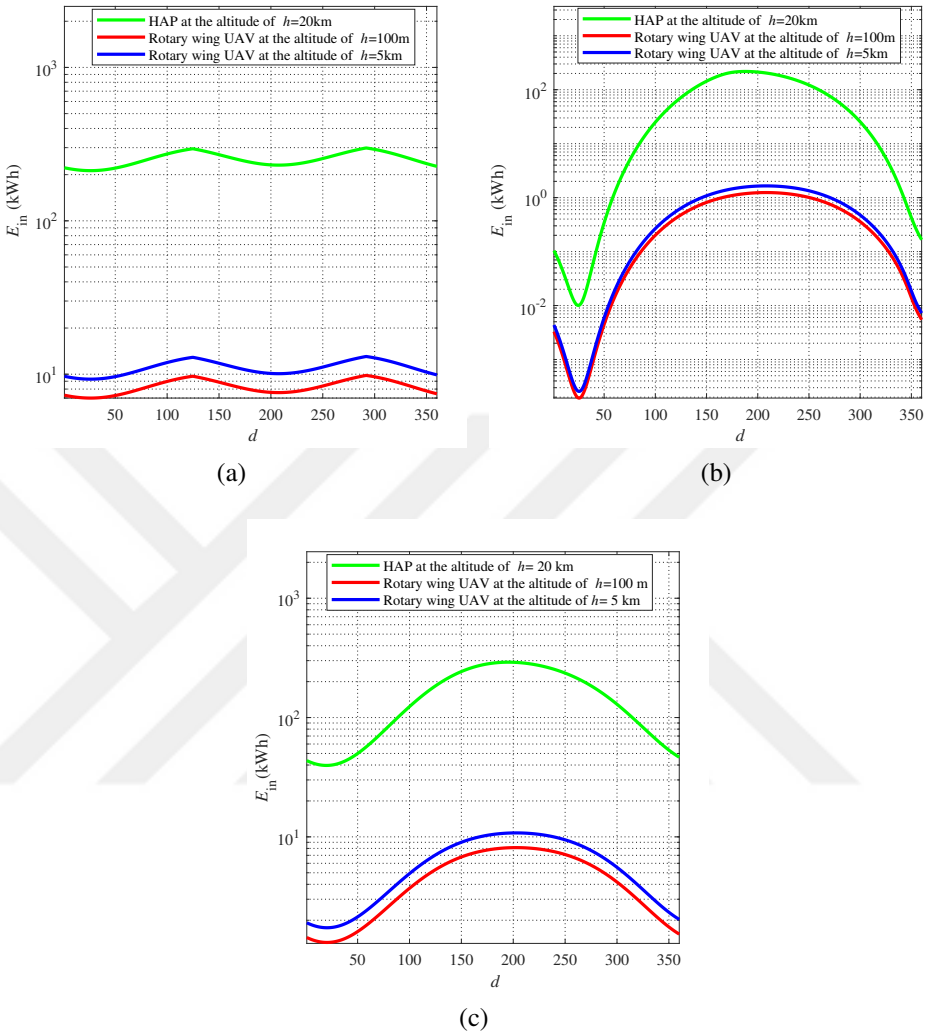


Figure 6: Harvested energy from the Sun in different days of the year in climate type of (a) Tropical, (b) Subarctic, (c) Midlatitude.

during the spring equinox, which is the 80th day of the year, the HAP harvests $E_{\text{in}} =$ 81.6kWh of energy. In comparison, the rotary wing UAV in a one-hour mission harvested $E_{\text{in}} = 190$Wh, $E_{\text{in}} = 430$Wh, and $E_{\text{in}} = 190$Wh, of energy at altitudes of $h = 100$m during morning (8:30 am to 9:30 am), noon (from 11:30 am to 12:30 pm) and afternoon (from 3:30 pm to 4:30 pm) respectively. If the operation altitude is at $h = 5$km, the rotary wing UAV harvested $E_{\text{in}} = 285$Wh, $E_{\text{in}} = 571$Wh, and $E_{\text{in}} = 285$Wh of energy during the same noon and afternoon time periods respectively.

Moving on to the summer solstice on June 21st, which is the 173rd day of the year,

the HAP harvested $E_{\text{in}} = 243.35$kWh. In comparison, the rotary wing UAV in a one-hour mission harvested $E_{\text{in}} = 500$Wh, $E_{\text{in}} = 1$kWh, and $E_{\text{in}} = 500$Wh of energy at altitudes of $h = 100$m during morning (8:30 am to 9:30 am), noon (from 11:30 am to 12:30 pm) and afternoon (from 3:30 pm to 4:30 pm) respectively. If the operation altitude is at $h = 5$km, the rotary wing UAV harvested $E_{\text{in}} = 702$Wh,$E_{\text{in}} = 1.4$kWh and, $E_{\text{in}} = 702$Wh during the same noon and afternoon time periods respectively.

As we approach the fall equinox on September 23rd, which is the 266th day of the year, the HAP harvests $E_{\text{in}} = 196.7$kWh. In comparison, the rotary wing UAV in a one-hour mission harvested $E_{\text{in}} = 405$Wh , $E_{\text{in}} = 983$Wh, and $E_{\text{in}} = 405$Wh of energy at altitudes of $h = 100$m during morning (8:30 am to 9:30 am), noon (from 11:30 am to 12:30 pm) and afternoon (from 3:30 pm to 4:30 pm) respectively. If the operation altitude is at $h = 5$km, the rotary wing UAV harvested $E_{\text{in}} = 650$Wh, $E_{\text{in}} = 1.3$kWh, and $E_{\text{in}} = 650$Wh during the same noon and afternoon time periods respectively.

Finally, during the winter solstice on December 22nd, which is the 357th day of the year the HAP harvested $E_{\text{in}} = 48$kWh. In comparison, the rotary wing UAV in a one-hour mission harvested $E_{\text{in}} = 90$Wh, $E_{\text{in}} = 321$Wh, and $E_{\text{in}} = 90$Wh of energy at altitudes of $h = 100$m during morning (8:30 am to 9:30 am), noon (from 11:30 am to 12:30 pm) and afternoon (from 3:30 pm to 4:30 pm) respectively. If the operation altitude is at $h = 5$km, the rotary wing UAV harvested $E_{\text{in}} = 110$Wh, $E_{\text{in}} = 427$Wh, $E_{\text{in}} = 110$Wh and during the same noon and afternoon time periods, respectively.

It can be observed that on $d = 215$th day of the year, the nodes are able to harvest maximum energy from the Sun and on $d = 25$th day of the year, they can harvest the lowest amount of energy from the sun.

2.2.3 Energy Harvesting Model in Underwater Environments

In this section, we offer essential principles for modeling the energy acquisition from a solar panel that can be affixed to an AUV in underwater settings. In this context, beyond the

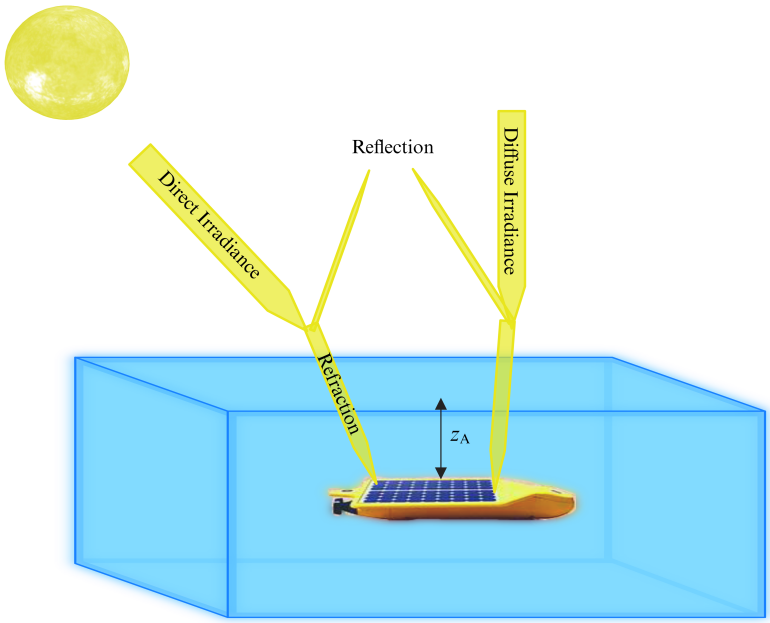


Figure 7: Solar irradiance and various effects on it in its way of reaching the destination.

factors that influence solar intensity in outdoor conditions, the extinction coefficient of the water, the operational depth of the AUV, as well as absorption and scattering phenomena also contribute to determining the intensity reaching a particular depth. As depicted in Fig. 7, the overall solar intensity above the water includes direct and diffuse irradiance. A portion of direct and diffuse irradiance reflects from the air-water interface and a portion of it is refracted through the surface to the water [59]. The refracted portion will then pass through the water while facing attenuation in its way to reach the AUV. Thus, the received solar energy at a specific depth is affected by many factors including attenuation of the light intensity due to absorption and scattering, active surface area of the solar panel attached to the vehicle, and the solar panel's efficiency [60]. Mathematically speaking, the harvested energy by the AUV during the mission time is given by [61]

$$E_{\text{h,underwater}} = \int_{t=t_{\text{start}}}^{t_{\text{start}}+T} \Phi_{\text{in}}(t)dt, \tag{2.13}$$

Table 2: Parameters for calculating EH from the Sun by the AUV

Parameter	**Variable**	**Value**
Solar Area of the AUV	$A_s\ (m^2)$	1
Solar Constant	$G_{sc}\ (W/m^2)$	1366.1
Efficiency of the Solar Cell	$\eta_{sc}\ (\%)$	20
Refractive index of air	n_1	1
Refractive index of water	n_2	1.33
Extinction coefficient for pure sea	c	0.056 m^{-1}
Extinction coefficient for clear ocean	c	0.015 m^{-1}
Extinction coefficient for coastal water	c	0.305 m^{-1}
Extinction coefficient for harbor water	c	2.17 m^{-1}

where $\Phi_{in}(t)$ is the harvested power at time t and is given by

$$\Phi_{in}(t) = \psi A_s \eta_{sc} G_{in}(t)(1-\Upsilon_{tot})\exp(-cz_A(t)) \tag{2.14}$$

where z_A is the depth of the AUV, c is the extinction coefficient of the water. In Eq. (2.13) on the preceding page, Υ_{tot} is the overall reflection of the solar direct irradiance from the ocean surface. Assuming that the light in unpolarized and the water surface is flat, it can be calculated as the average of the reflectivity of the s-polarized and p-polarized light, i.e., $\Upsilon_{tot} = 0.5\left(\Upsilon_s(t) + \Upsilon_p(t)\right)$ where $\Upsilon_s(t)$ and $\Upsilon_p(t)$ are respectively given by

$$\Upsilon_s(t) = \left[\frac{n_1 \sin(\xi(t)) - n_2 g(t)}{n_1 \sin(\xi(t)) + n_2 g(t)}\right]^2. \tag{2.15}$$

$$\Upsilon_p(t) = \left[\frac{n_1 g(t) - n_2 \sin(\xi(t))}{n_1 g(t) + n_2 \sin(\xi(t))}\right]^2. \tag{2.16}$$

In the above, $g(t) = \sqrt{1 - \left[(n_1/n_2)\cos(\xi(t))\right]^2}$, n_1 and n_2 are the indexes of refraction for air and water, respectively.

2.2.4 Results and Discussions

In this section, we present the potential levels of underwater harvested power for a given operation depth, water type, and geographical location. Considering the parameters provided in Table 2, we provide the results concerning the amount of power that can be received by the solar-powered AUV while on the water surface and while on the mission at different

depths of the water. The amount of harvested energy is obviously dependent on the time of the day and geographical location. We assume four representative days of the year, namely January 1st (i.e., $d = 1$), March 30th ($d = 90$), June 28th ($d = 180$), and September 26th ($d = 270$). In addition, we consider three climate types including tropical, mid-latitude, and subarctic. As examples, we consider

- Indian Ocean with latitude of $L = 0.06^{\circ}$ (representative of tropical climate type),
- Arctic Ocean with latitude of $L = 65.24^{\circ}$ (representative of subarctic climate type), and
- Black Sea with latitude of $L = 41.8^{\circ}$ (representative of mid-latitude climate type).

The solar-powered AUV is assumed to be located on the sea surface, i.e., $z_{\mathrm{A}} = 0$. Fig. 8 on the following page illustrate the hourly variations of the harvested power using Eq. (2.14) on the previous page in tropical, subarctic, and mid-latitude climate types under consideration for different seasons. A comparison of these figures reveals that there might be significant differences in the amount of harvested energy depending on the time of the day, specific season, and geographical location. For geographical locations and the representative days under consideration, the maximum harvested power is obtained around $w_{\max} = 12$ (when the zenith angle is at a minimum level or equivalently the solar elevation angle is at the maximum level). The determination of $w_{\max}$ is critical to achieving the best performance in terms of energy harvesting while planning the mission. If the AUV's mission time takes T hours, the AUV should start its mission $T/2$ hours before $w_{\max}$ so it can hit $w_{\max}$ just in the middle of the mission. The best start time is then determined as $t_{\mathrm{start}} = |w_{\max} - T/2|$. It should also be noted that the daylight hours are different for these locations. In tropical climates, the daylight duration is almost the same (12 hours) for all the representative days. Moreover, there is not much difference between the amount of harvested power on different days of the year for this location, while for subarctic and mid-latitude locations, the specific season has a significant effect.

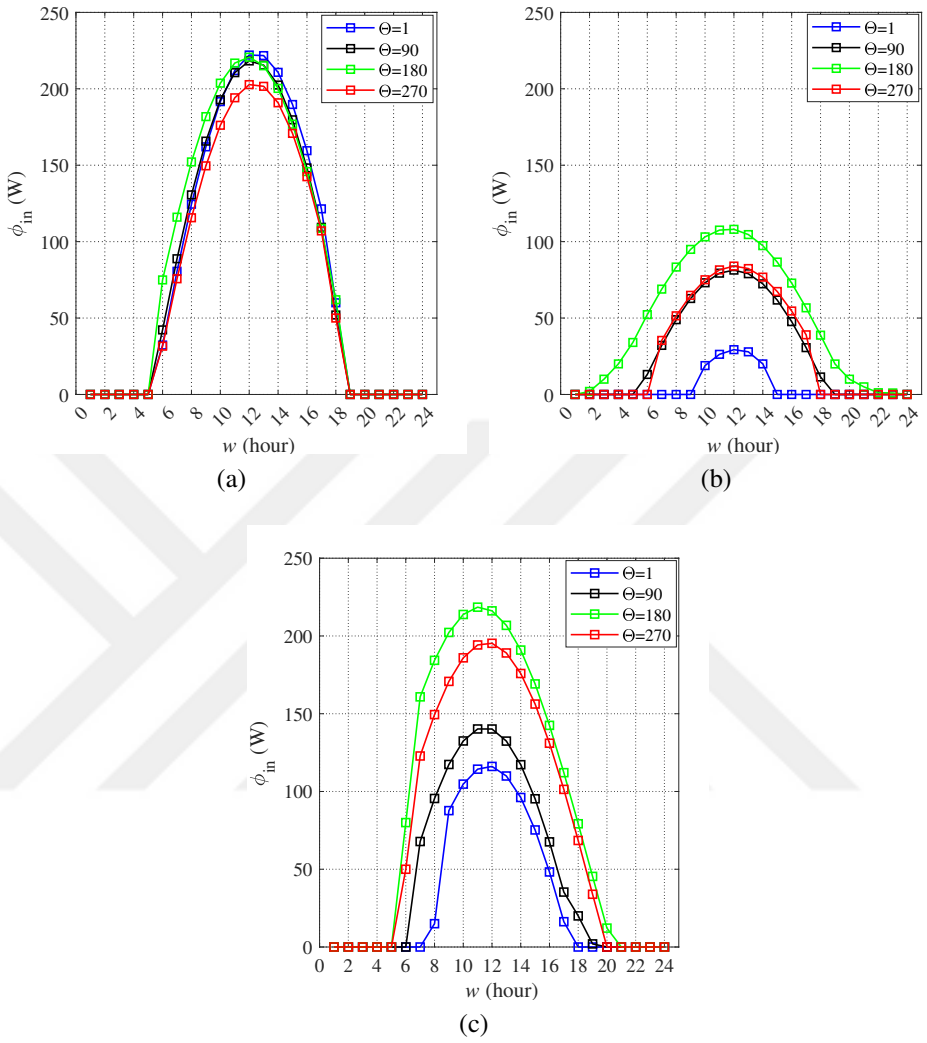


Figure 8: Hourly variation of harvested power on the sea surface for different days in climate type of (a) Tropical, (b) Subarctic, (c) Midlatitude.

For example, maximum and minimum levels of harvested power are $\Phi_{\text{in,max}} = 222.1\,\text{W}$ and $\Phi_{\text{in,min}} = 202.7\,\text{W}$ respectively for $d = 1^{\text{st}}$ and $d = 270^{\text{th}}$ day of the year for tropical climate type. These significantly decrease for the representative subarctic location where maximum and minimum levels are observed as $\Phi_{\text{in,max}} = 108.1\,\text{W}$ and $\Phi_{\text{in,min}} = 29.31\,\text{W}$ respectively for $d = 180^{\text{th}}$ and $d = 1^{\text{st}}$ day of the year.

In the following, we assume the mid-latitude climate type (Black Sea location) as an example. Fig. 9 on the following page illustrates the average amount of harvested power (averaged over daytime hours) with respect to operation depth for different water types. For

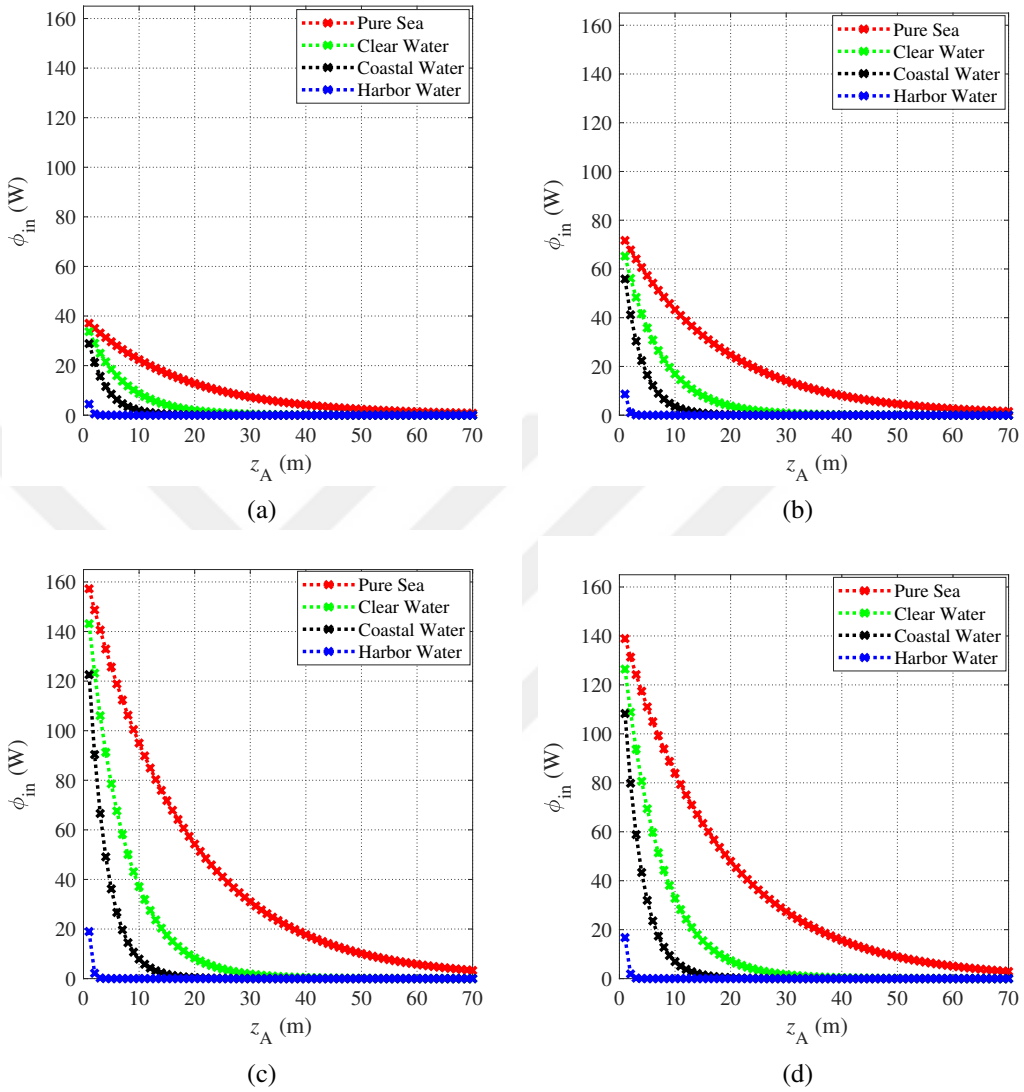


Figure 9: Average amount of harvested power with respect to depth for different water types on (a) 1st day, (b) 90th day, (c) 180th day, (d) 270th day of the year.

example, on the $d = 180^{\text{th}}$ day of the year, when the AUV is close to the sea surface (i.e., $z_{\text{A}} \leq 1\,\text{m}$), it is capable of harvesting an average amount of $\Phi_{\text{in}} \geq 161\text{W}$, $\Phi_{\text{in}} \geq 146.5\text{W}$, $\Phi_{\text{in}} \geq 125.5\text{W}$, and $\Phi_{\text{in}} \geq 19.4\text{W}$ in pure sea, clear water, coastal water, and harbor water, respectively. As the depth increases, the harvested energy diminishes. For example, in pure sea, when the depth is less than 70 m, the harvested energy becomes negligible. As turbidity increases, the required depth further decreases. The harvested energy becomes zero for $z_{\text{A}} \geq 70\,\text{m}$, $z_{\text{A}} \geq 35\,\text{m}$, $z_{\text{A}} \geq 15\,\text{m}$, and $z_{\text{A}} \geq 2\,\text{m}$, respectively, for clear water,

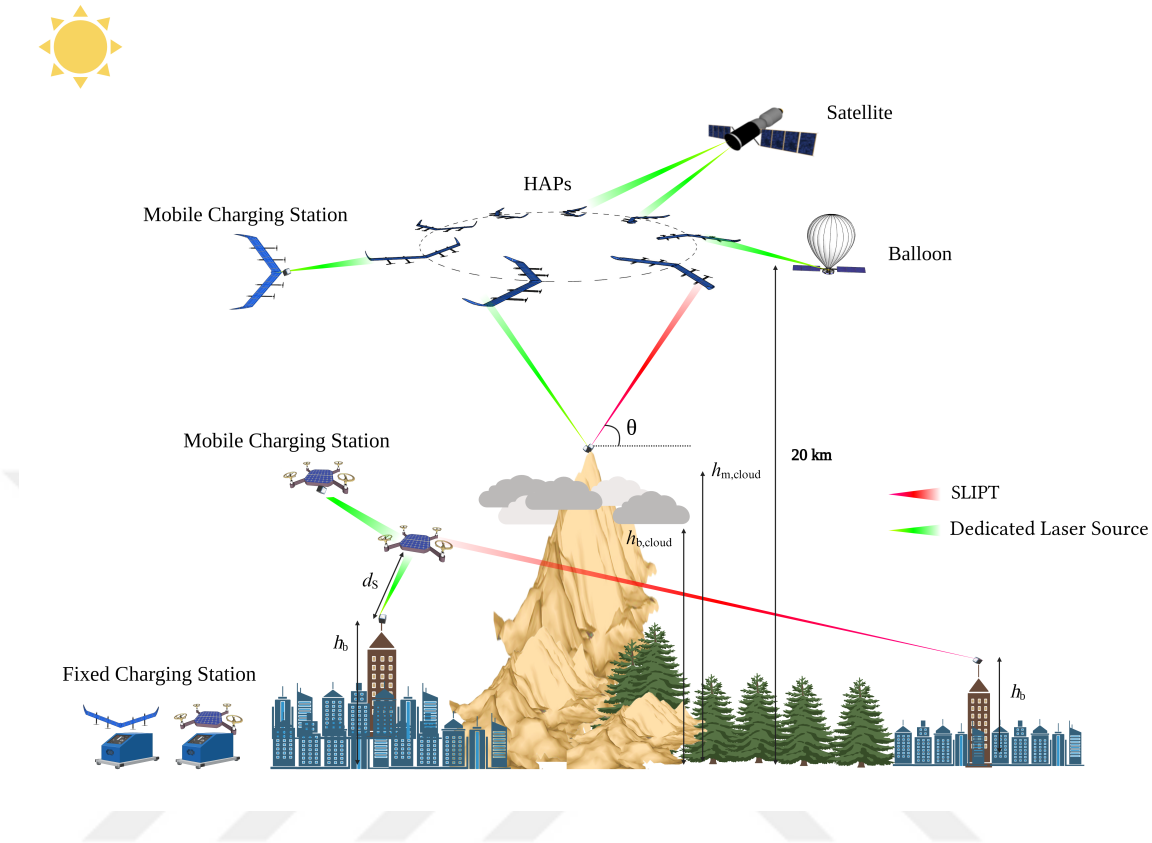


Figure 10: Laser Power Beaming and SLIPT for powering airborne nodes.

coastal water, and harbor water. These results indicate that the AUV is indeed capable of harvesting power even when operating underwater. However, the amount of harvested energy is significantly dependent on the water type as well as the operation depth.

2.3 Energy Harvesting From Laser Power Beaming

Integrating laser power beaming into OWC networks offers numerous benefits. Firstly, it eliminates the need for physical connections or cables to recharge airborne vehicles, streamlining operations and enhancing vehicle autonomy for prolonged missions and remote deployments. Additionally, real-time power replenishment ensures a continuous and uninterrupted power supply for airborne vehicles, particularly crucial in mission-critical applications like disaster response and surveillance. Furthermore, adopting laser power beaming aligns with global efforts for greener and sustainable operations.

The laser beam originating from the charging station is subjected to attenuation caused

by several factors before it reaches the UAV/HAP. Two primary factors that affect the laser beam are: (i) geometrical loss due to the optical beam's divergence, and (ii) atmospheric loss due to the absorption and scattering by air molecules [62].

The geometric loss is given by

$$L_{\mathrm{G}} = \frac{{D_{\mathrm{r}}}^2}{\left(D_{\mathrm{r}} + d_{\mathrm{S}}\Delta\theta\right)^2} \tag{2.17}$$

where D_{r} is the diameter of the receiver, d_{S} is the distance between the laser source and the UAV/HAP, and $\Delta\theta$ is the angular spread of the laser beam. The atmospheric loss is given by

$$L_{\mathrm{P}} = e^{-\alpha d_{\mathrm{S}}} \tag{2.18}$$

where α is the medium attenuations coefficient (extinction coefficient). Consequently, the received laser power at the UAV/HAP during a given time slot is formulated as

$$P_{\mathrm{H}} = \frac{P_{\mathrm{L}} D_{\mathrm{r}}^2 \chi e^{-\alpha d_{\mathrm{S}}}}{\left(D_{\mathrm{r}} + d_{\mathrm{S}}\Delta\theta\right)^2} \tag{2.19}$$

where P_{L} is the power of the laser beam, and χ is the laser power conversion efficiency.

In rainy conditions, the distance between the laser power source and the UAV/HAP is divided into three different segments. This division takes into account the base cloud height and the maximum cloud height, as shown in Fig. 10 on the previous page. The angle between the laser beam and the horizontal plane is denoted as

$$\theta = \tan^{-1}\left(\frac{(h - h_{\mathrm{b}})}{d_{\mathrm{S}}}\right) \tag{2.20}$$

where h_{b} is the altitude of the building/mountain at which the transmitter is located, and d_{S} is the slant link distance between the transmitter and the UAV/HAP.

We consider the base cloud height to be $h_{\mathrm{b,cloud}}$ and the maximum cloud height to be $h_{\mathrm{m,cloud}}$ [63]. In this case, the slant link, d_{S}, from the ground-based laser source to an altitude of $h_{\mathrm{b,cloud}}$ experiences rain, with an extinction coefficient of $\alpha_{\mathrm{r}} = 0.12\,\mathrm{km}^{-1}$. As a result, the slant distance between the laser source and the cloud at $h_{\mathrm{b,cloud}}$ altitude will

be $d_{\mathrm{r}} = h_{\mathrm{b,cloud}}/\sin(\theta)$ leading to an atmospheric loss of $L_{\mathrm{r}} = e^{-\alpha_{\mathrm{r}} d_{\mathrm{r}}}$. From $h_{\mathrm{b,cloud}}$ to $h_{\mathrm{m,cloud}}$ altitude, the weather conditions are considered foggy with an extinction coefficient of $\alpha_{\mathrm{f}} = 1.7\,\mathrm{km}^{-1}$. Consequently, the slant distance between the base cloud height of $h_{\mathrm{b,cloud}}$ and the cloud at $h_{\mathrm{m,cloud}}$ altitude will be $d_{\mathrm{f}} = (h_{\mathrm{m,cloud}} - h_{\mathrm{b,cloud}})/\sin(\theta)$, resulting in an atmospheric loss of $L_{\mathrm{f}} = e^{-\alpha_{\mathrm{f}} d_{\mathrm{f}}}$. Beyond $h_{\mathrm{m,cloud}}$ altitude up to the UAV/HAP level, the weather conditions are assumed to be clear with an extinction coefficient of $\alpha = 0.01\,\mathrm{km}^{-1}$. Therefore, the slant distance between the cloud at $h_{\mathrm{m,cloud}}$ altitude and the UAV/HAP at higher altitudes is considered clear, with a slant link of $d_{\mathrm{c}} = (h - h_{\mathrm{m,cloud}})/\sin(\theta)$. This segment incurs an atmospheric loss of $L_{\mathrm{c}} = e^{-\alpha d_{\mathrm{c}}}$.

The total atmospheric loss from the ground to the UAV/HAP is then $L_{\mathrm{total}} = L_{\mathrm{r}} L_{\mathrm{f}} L_{\mathrm{c}} = e^{-(\alpha_{\mathrm{r}} d_{\mathrm{r}} + \alpha_{\mathrm{f}} d_{\mathrm{f}} + \alpha d_{\mathrm{c}})}$.

In the presence of fog, we take into account the maximum cloud height of $h_{\mathrm{m,cloud}}$. The extinction coefficient for the ground-to-cloud altitude is assumed to be the same as the extinction coefficient of $\alpha_{\mathrm{f}} = 1.7\,\mathrm{km}^{-1}$. The slant link in this case is $d_{\mathrm{f}} = h_{\mathrm{m,cloud}}/\sin(\theta)$. From the altitude of $h_{\mathrm{m,cloud}}$ up to the UAV/HAP level, the weather is considered clear, resulting in a slant distance of $d_{\mathrm{c}} = (h - h_{\mathrm{m,cloud}})/\sin(\theta)$. The total atmospheric loss will be $L_{\mathrm{total}} = L_{\mathrm{f}} L_{\mathrm{c}}$.

If the altitude of the transmitter is higher than the maximum altitude of the cloud (i.e., $h_{\mathrm{b}} > h_{\mathrm{m,cloud}}\,\mathrm{m}$), we use the following formula for rainy conditions:

$$P_{\mathrm{H}} = \frac{P_{\mathrm{L}} D_{\mathrm{r}}^2 \chi e^{-\frac{1}{\sin(\theta)}(h_{\mathrm{b,cloud}}\alpha_{\mathrm{r}} + (h_{\mathrm{m,cloud}} - h_{\mathrm{b,cloud}})\alpha_{\mathrm{f}} + (h - h_{\mathrm{m,cloud}})\alpha)}}{(D_{\mathrm{r}} + d_{\mathrm{S}}\Delta\theta)^2} \tag{2.21}$$

For the fog, we use the following formula

$$P_{\mathrm{H}} = \frac{P_{\mathrm{L}} D_{\mathrm{r}}^2 \chi e^{-\frac{1}{\sin(\theta)}(h_{\mathrm{m,cloud}}\alpha_{\mathrm{f}} + (h - h_{\mathrm{m,cloud}})\alpha)}}{(D_{\mathrm{r}} + d_{\mathrm{S}}\Delta\theta)^2} \tag{2.22}$$

If the altitude of the transmitter is lower than the maximum altitude of the cloud (i.e., $h_{\mathrm{b}} < h_{\mathrm{m,cloud}}$), we use the same formula as provided in Eq. (2.19) on the preceding page for any conditions (clear, rainy, foggy). If the mission time is T hours, the harvested energy

Table 3: Parameters for Calculating EH from Laser Power Beaming

Parameter	**Variable**	**Value**
Transmit power	P_{L} (kW)	1-10
Photovoltaic laser power converter	χ (%)	68.9
diameter of the receiver	D_{r} (m)	0.4
Size of the initial laser beam	D_L (m)	0.15
Angular spread	$\Delta\theta$	3.4×10^{-5}
altitude of the building	h_{b} (m)	30
Horizontal distance	d_{H} (m)	200 (UAV)/8000 (HAP)
Extinction coefficient of clear weather	α (km^{-1})	0.01
Extinction coefficient of rainy weather	α_{r} (km^{-1})	0.12
Extinction coefficient of foggy weather	α_{f} (km^{-1})	1.7

is calculated by $E_{\mathrm{h,laser}} = P_{\mathrm{H}}T$.

2.3.1 Results and Discussions

We consider a dedicated laser source on top of a building with an altitude of $h_{\mathrm{b}} = 30\,\mathrm{m}$ as a charging station to charge the rotary wing UAV while in the mission, and a dedicated laser source on top of a mountain with $h_{\mathrm{b}} = 1\,\mathrm{km}$ height as the charging station to charge the HAP while in the mission.

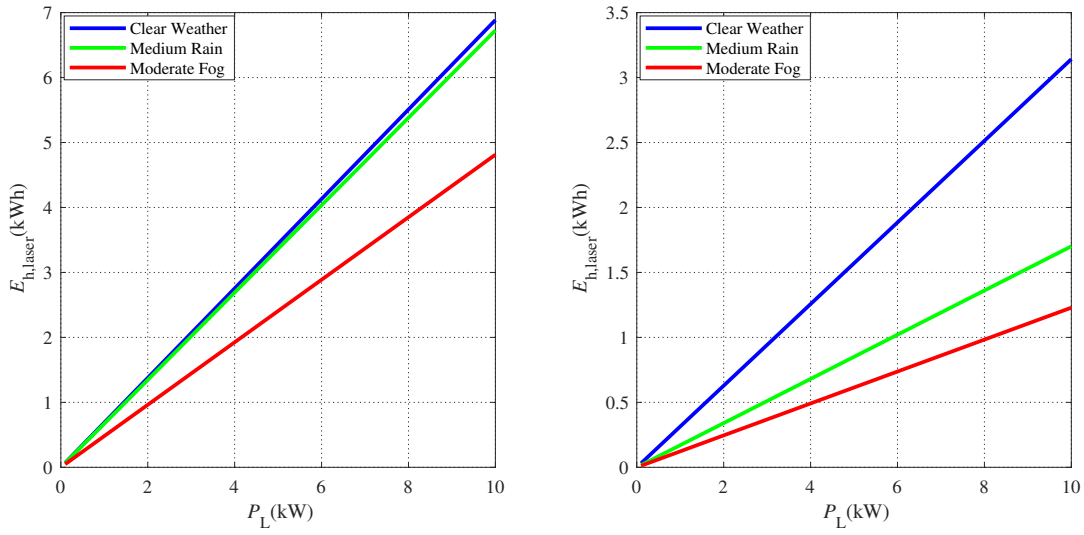


Figure 11: Energy harvested using laser power beaming by a rotary wing UAV at an altitude of (a) $h = 100\,\mathrm{m}$, and (b) $h = 5\,\mathrm{km}$

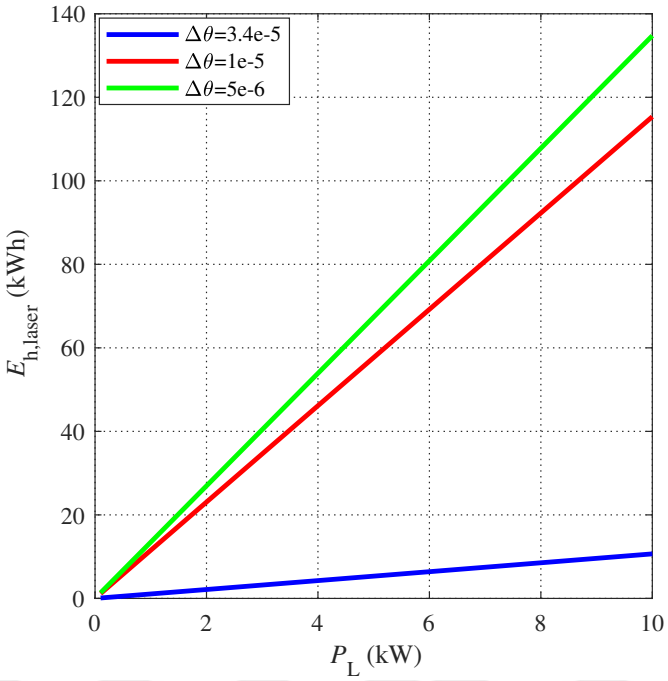


Figure 12: Energy harvested by a HAP using laser power beaming.

Considering the parameters given in Table 3 on the previous page, Fig. 11 on the preceding page, illustrate the energy harvesting from the laser power beaming in an one hour mission of the rotary wing UAV at altitude of $h = 100\,\text{m}$ and $h = 5\,\text{km}$, respectively. We have considered the three weather conditions including clear weather, rain, and fog with extinction coefficient values given in Table 3 on the previous page. Obviously, in clear weather the harvested energy is higher than in the other two weather conditions.

Fig. 12 displays the energy acquired through laser power beaming when factoring in a designated laser source positioned at an elevation of $h_\text{b} = 1\,\text{km}$ while the HAP is engaged in a 24-hour mission at an altitude of $h = 20\,\text{km}$. We explore various angular spreads of the laser beam, which impact the geometric loss of the laser beam, in order to evaluate the power harvesting capacity via laser power beaming. Clearly, as the angular spread of the laser beam diminishes, the geometric loss decreases, leading to an increase in the amount of harvested energy.

We also consider another fixed charging station for the rotary wing UAVs/HAPs, allowing them to pause for their desired duration and undergo recharging. In this scenario, the laser power source is in close proximity to the vehicle, ensuring that weather conditions do not influence the amount of energy they can harvest. In this case, the most important factors influencing the amount of power harvested are the power of the laser source and the laser power conversion efficiency. Considering a laser power of $P_{\mathrm{L}} = 4\,\mathrm{kW}$, the harvested energy in $T = 1$ hour for rotary-wing UAVs/HAPs is equal to $E_{\mathrm{h,laser}} = 2.75\mathrm{kWh}$.

In the scenario involving a mobile charging station, we contemplate the use of another rotary-wing UAVs/HAPs to supply power to the UAVs/HAPs currently on a mission. In this setup, the mobile charging station can approach the UAVs/HAPs in need of charging. With the slant distance of $d_{\mathrm{S}} = 1\mathrm{m}$, and a transmit power of $P_{\mathrm{L}} = 4\mathrm{kW}$, the UAV in mission can harvest energy equal to almost $E_{\mathrm{h,laser}} = 2.76\mathrm{kWh}$ in all the weather conditions under consideration. Regarding the HAPs, we take into account the presence of another HAP as the mobile charging station that can supply power to the one currently engaged in the mission. This supporting HAP can approach the circular trajectory area where the HAPs are positioned during the mission. At $d_{\mathrm{S}} = 1\mathrm{km}$ and with a laser power source outputting $P_{\mathrm{L}} = 4\mathrm{kW}$, the HAP in the mission can harvest an amount of energy totalling $E_{\mathrm{h,laser}} = 66$ kWh over $T = 24$ hours.

2.4 Energy Harvesting From SLIPT

The fundamental principle of SLIPT lies in the dual-purpose utilization of lightwaves. The same lightwave that carries data is also used to generate electrical power through the photovoltaic cells integrated into the OWC system. This concurrent data transmission and energy harvesting optimize resource utilization and minimize energy losses, making the system more efficient. In OWC systems with SLIPT capability, a main design issue is the choice of receiver. The receiver can be either the common choice of Photodiode (PD), which produces a high data rate, or an alternative choice, i.e., solar cells, which provide

obvious advantages in terms of energy harvesting efficiency. networks. In order to enable energy harvesting and information decoding at the same time, there are some strategies that have been proposed so far. In time splitting strategy, during a portion of time, the received signal is solely used for either energy harvesting or information decoding [64], while the power splitting technique is based on the division of the signal power into two streams to obtain separated signals where one portion is used for energy harvesting and the other one is used for information decoding [65]. The photoelectric converters technique refers to multiple PDs that are employed at the receiver and some of them are used for energy harvesting while the rest are used for information decoding using a switching key [66], and Alternating Current (AC)/Direct Current (DC) separator is the simplest method in which a capacitor is used to block the DC components and an inductance is used to block the AC components of the received signal [67].

In our analysis, we explore the possibility of using a FSO laser beam as a charging system for UAVs/HAPs considering SLIPT with the method of power splitting. We assume that the transmitted laser power is divided into two parts. Considering ρ as the power splitting factor used to separate the energy transfer link and the communication link, the harvested power in SLIPT is [62]

$$P_{\mathrm{S}} = (1-\rho)\, P_{\mathrm{H}} \tag{2.23}$$

Here, P_{H} represents the received power from the transmitter, which is computed using the same method described in the preceding section. This method is used to determine the laser power beaming under various weather conditions, with detailed calculations. If the mission time is T hours, the harvested energy using SLIPT is calculated by $E_{\mathrm{h,SLIPT}} = P_S T$.

2.4.1 Results and Discussions

Fig. 13(a) on the next page and Fig. 13(b) on the following page depict the energy harvested by the rotary-wing UAV at altitudes of $h = 100\,\mathrm{m}$ and $h = 5\,\mathrm{km}$, respectively. considering a horizontal distance of d_{H} =5km from the FSO transmitter to the rotary-wing UAV and

other parameters provided in Table 3. These figures showcase the energy harvested for different transmit powers.

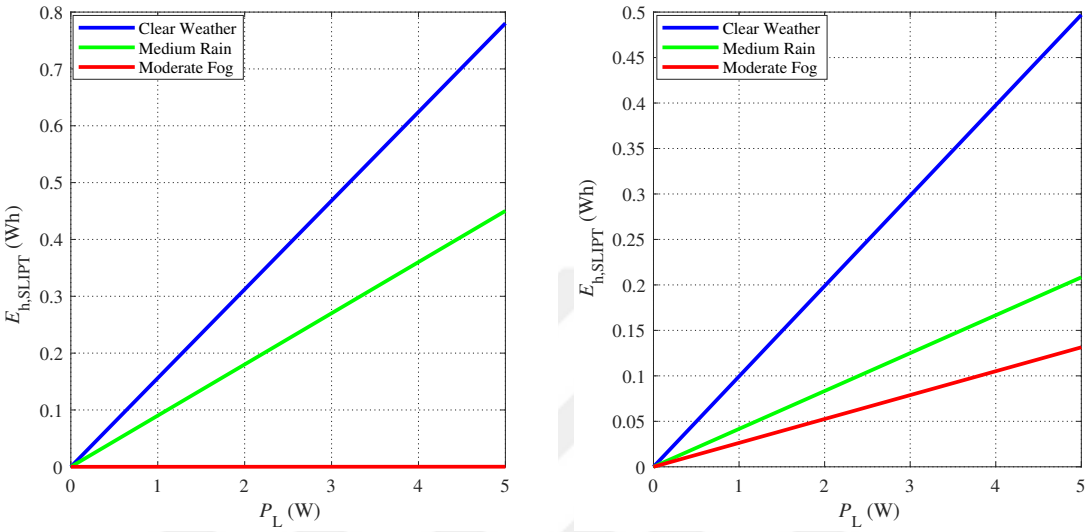


Figure 13: Energy harvested by rotary wing UAV using SLIPT at an altitude of (a) $h =$ 100 m, and (b) $h = 5$ km

Considering the horizontal distance of d_H =8km from the FSO transmitter to the HAP, Fig. 14 on the next page illustrates the energy harvested by the HAP operating in the stratosphere using SLIPT over a 24-hour period using Eq. (2.23) on the preceding page. It considers various practical values of angular spreads of the laser beam. The graph shows that the energy harvested is influenced by the angular spread of the laser beam. When the angular spread of the laser beam is lower, a higher amount of energy can be harvested. This outcome is a result of the opposite impact on the geometrical loss, which increases with lower angular spread amounts. In simpler terms, a narrower beam allows for more focused and efficient energy transfer, leading to greater energy harvesting compared to a wider beam with more energy dispersion.

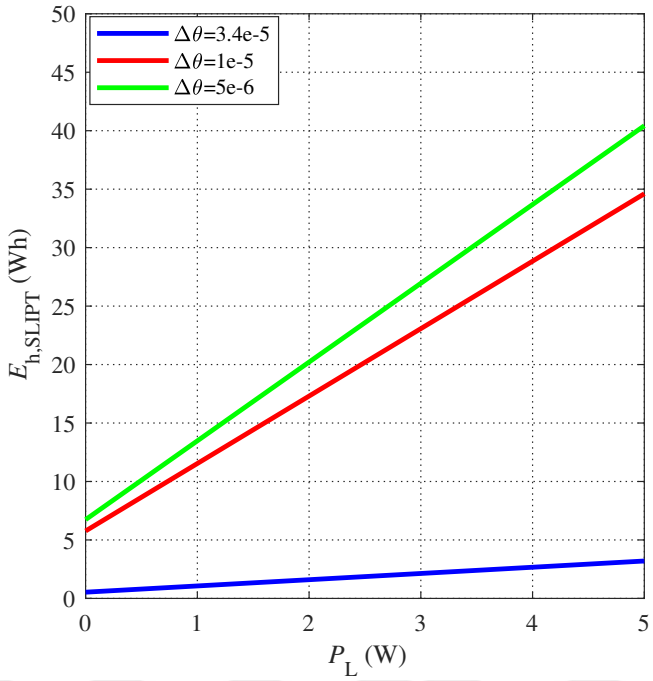


Figure 14: Energy harvested by HAP using SLIPT at an altitude of $h = 20\,\text{km}$.

2.5 Extended Operation Time of the Autonomous Vehicles (AUVs/UAVs/HAPs)

The extended operation time calculation is crucial for vehicles with energy harvesting capabilities. To accurately determine the total operation time, we employ an iterative approach that considers continuous power harvesting throughout the operation. This method guarantees precision in estimating the total operation duration, accounting for energy harvested during both the initial operation phase and subsequent extended operation segments. The initial operation time, representing the duration without energy harvesting, is calculated using the following formula

$$T_{\text{i}} = \frac{E_{\text{b}}}{P_{\text{out}}} \tag{2.24}$$

where E_{b} is the battery's initial capacity in Wh, and P_{out} is the power consumption in W. To consider the continuous power harvesting during the extended operation of the vehicle, we need to use an iterative approach as in Algorithm 1 on the next page.

Algorithm 1 Total Operation Time Calculation with Continuous Power Harvesting

Inputs:

- E_b (Battery Capacity in Wh)
- P_{out} (Power Output in W)
- P_{in} (Power Harvesting in W)

Outputs:

- T_{tot} (Total Operation Time in hours)

Calculate the initial operation time using T_{i} in Eq. (2.24) on the preceding page
Set remaining capacity as battery capacity: $E_{\text{remaining}} = E_b$
Set total operation time as initial operation time: $T_{\text{tot}} = T_{\text{i}}$
Calculate the energy harvested during the initial operation time, $E_{\text{in}} = P_{\text{in}} T_{\text{i}}$
Update remaining capacity as, $E_{\text{remaining}} = E_{\text{in}}$
while remaining capacity $E_{\text{remaining}} \geq 0$ **do**
    Calculate the extended operation time using $T_{\text{ex}} = E_{\text{remaining}} / P_{\text{out}}$
    Update total operation time by adding the extended operation time: $T_{\text{tot}} = T_{\text{tot}} + T_{\text{ex}}$
    Update energy harvested during the extended operation time
    Update remaining capacity as the energy harvested
end while
Return total operation time: T_{tot}

This algorithm computes the total operation time of a vehicle with energy harvesting capabilities. It takes three inputs including battery capacity, E_{b}, power consumption, P_{out}, and power harvesting input, P_{in}. The process begins by initializing ”energy harvested” to zero and calculating the initial operation time. It then enters an iterative loop, continuously updating the operation time, energy harvested, and remaining capacity until energy runs low. In each iteration, it calculates the extended operation time and updates the total operation time. The algorithm accounts for energy harvested during the mission.

Upon completion, it returns the total operation time, providing an accurate estimate that considers both energy harvesting and power consumption dynamics.

CHAPTER III

ENERGY MANAGEMENT SOLUTIONS IN UOWC SYSTEMS

3.1 Introduction

The vastness of our planet's oceans, covering about 71 percent of the Earth's surface, holds a wealth of untapped knowledge and potential resources. However, our understanding of these vast underwater realms remains limited, leaving a significant portion of it unexplored. The exploration of oceans is of paramount importance, not only for security but also for managing ocean resources, studying weather and climate patterns, and supporting life on Earth.

To efficiently delve into the depths of the oceans and unlock their mysteries, USNs have emerged as indispensable tools. These networks consist of groups of sensors and vehicles deployed underwater, communicating through optical or acoustic signaling, and working collaboratively to perform various crucial tasks. Among the tasks undertaken by USNs are pollution monitoring, ocean currents tracking, equipment monitoring and control, underwater oil field detection, and valuable mineral explorations.

AUVs play a particularly instrumental role in USNs, facilitating the retrieval of vital data from the sensor nodes. As unmanned and untethered vehicles, AUVs can conduct their survey missions without the need for operator intervention. Once the mission is complete, they autonomously return to pre-programmed locations, where the collected data can be downloaded and processed. Equipped with video cameras, lights, and robotic arms, AUVs can venture into areas that humans cannot safely access, enabling us to safely study and comprehend the intricate complexities of the ocean.

However, AUV operations are constrained by the challenge of power consumption, as these vehicles rely on batteries with limited lifetimes. Consequently, the choice of efficient

trajectories becomes a critical factor that directly impacts AUV mission planning. Two primary trajectory types are commonly considered: predefined trajectories and reactive trajectories.

Predefined trajectories, such as elliptical, circular, and lawnmower patterns, are planned before the AUV embarks on its mission. While straightforward, these trajectories often prove less energy-efficient, as the AUV must adhere to the predefined path regardless of the presence or absence of sensor nodes in the vicinity. On the other hand, reactive trajectories are designed to adapt and respond to sudden changes during the mission, providing more flexibility and potential for energy savings.

In this chapter, our main goal is to address the limitation of AUV operations related to power consumption by focusing on the development of efficient trajectories. Specifically, we aim to determine the optimal trajectory of the AUV in the presence of ocean currents while adhering to communication requirements. By formulating the trajectory optimization problem, we seek to minimize the energy consumption of the AUV while ensuring seamless data retrieval from sensor nodes using optical wireless communication systems in underwater environments. The outcome of this research promises to enhance the energy efficiency and overall performance of underwater sensor networks, contributing to more sustainable and effective exploration of the ocean's depths.

In the subsequent sections, we will delve into the system model, communication requirements, trajectory optimization methodologies, and numerical results.

3.2 2D Trajectory Optimization of AUVs

As we noted in the introduction part, in AUV operations, the major limiting constraint is power consumption since they rely on batteries with limited lifetime. Therefore, the choice of efficient trajectories directly impacts the mission planning of AUVs. Predefined trajectories, as the name implies, are planned before the AUV starts its mission. In [7–10],

elliptical, circular and lawnmower patterns were investigated as predefined AUV trajectories in acoustic USNs. Since the AUV must complete the defined trajectory, whether or not there are sensors around, the energy efficiency of predefined trajectories remains low in particularly for large mission areas with randomly distributed sensor nodes. Another choice is reactive trajectories where the AUV path is corrected in real-time and refined to cope with the sudden changes during the operation. In the literature, there have been some works on reactive trajectory optimization assuming both acoustic [11–14] and VLC [15] signaling. In [11, 12], trajectory planning of the AUV is formulated as a TSP to minimize the AUV travel time and the ant colony algorithm is applied to solve the TSP. In [13, 14] TSP algorithm is proposed to define the path of the AUV with the objective of maximizing the VoI from the sensors. In [15], the trajectory finding problem of the AUV is solved using a greedy algorithm under VoI constraints. The abovementioned papers on reactive trajectories [11–15] simply assume that the AUV follows a straight path between each two sensor nodes without any deviations. However, in real-life conditions, due to ocean currents, that might not be possible. Trajectory optimization of stand-alone AUVs in the presence of ocean currents was addressed in [16–18]. However, these papers focus on stand-alone AUVs which move from a pre-defined start point to an endpoint. They do not take into account either the distribution of sensors in USN or signaling aspects between the AUV and the sensor.

In our work, we consider a VLC-based USN network where the AUV is used for data retrieval from the sensors. Our objective is to determine the optimal trajectory of the AUV in the presence of ocean currents under the constraints of communication requirements. For trajectory definition, we formulate an optimization problem to minimize the energy consumption of the AUV. The communication constraint imposes a minimum required data rate for the VLC link between the AUV and each sensor node. This therefore dictates that the AUV needs to be at a certain distance from the sensor node. The optimal solution for the general case (i.e., where the order of sensor node visits is not defined) is very difficult,

if not impossible. Therefore, we resort to a sub-optimal solution where we first determine the optimum sequence order of the sensor nodes to be visited, then optimize the trajectory between each pair of adjacent nodes for the given order of node visits. Our numerical results demonstrate that the proposed trajectory bring energy savings and decrease mission time in the presence of ocean currents.

3.2.1 Motion Model

As illustrated in Fig. 15 on the next page, we consider a USN with F sensors located at a depth of Z_{s} in an area of $G\,(\mathrm{km}) \times H\,(\mathrm{km})$.The location of the sensor S_i, $i = 1,2,...,F$is defined by the position vector $\mathbf{p}_{\mathrm{S_i}} = (x_{\mathrm{S_i}}, y_{\mathrm{S_i}}, z_{\mathrm{S_i}})$. AUV visits each sensor node once to retrieve data and returns to the initial point to transmit the aggregated data to a central node. Let T_i denote the travel time of the AUV from the sensor$\mathrm{S}_i$to the sensor S_{i+1}. This is divided into N equal-length time slots with a duration of $\Delta t_i = T_i/N$. If Δt_i is chosen sufficiently small, the location of the AUV can be assumed to be fixed during each time slot. Thus, the position of the AUV at the n^{th} slot, $n = 1,2,...,Q$, during its travel from S_i to S_{i+1} can be described by the vector $\mathbf{p}_{\mathrm{A}_i}[n] = (x_{\mathrm{A}_i}[n], y_{\mathrm{A}_i}[n], z_{\mathrm{A}_i}[n])$. Under the assumption that the AUV moves at a fixed depth, we can set $z_{\mathrm{A}_i}[n] = Z_{\mathrm{A}} > Z_{\mathrm{s}}$. Furthermore, we assume that the AUV moves with a constant speed at the horizontal plane [6]. Therefore, the velocity of the AUV is given by $v_{\mathrm{A}} = \left[v_{\mathrm{A}_x}, v_{\mathrm{A}_y}, 0\right]$. Accordingly, we formulate the discrete AUV state as

$$\mathbf{p}_{\mathrm{A}_i}[n] = \mathbf{p}_{\mathrm{A}_i}[n-1] + (\|v_{\mathrm{o}} + v_{\mathrm{A}}\|)\,\Delta t_i[n] \quad ,\forall \tag{3.1}$$

where $\|.\|$ denotes the Euclidean vector norm and $v_{\mathrm{o}} = \left[v_{\mathrm{o}_x}, v_{\mathrm{o}_y}\right]$ is the random vector quantifying the ocean current speed in a 2D space. Specifically, v_{o_x} and v_{o_y} are modeled as independent Gaussian random variables with mean value of $\alpha\,(\mathrm{m/s})$ and variance of β [18].

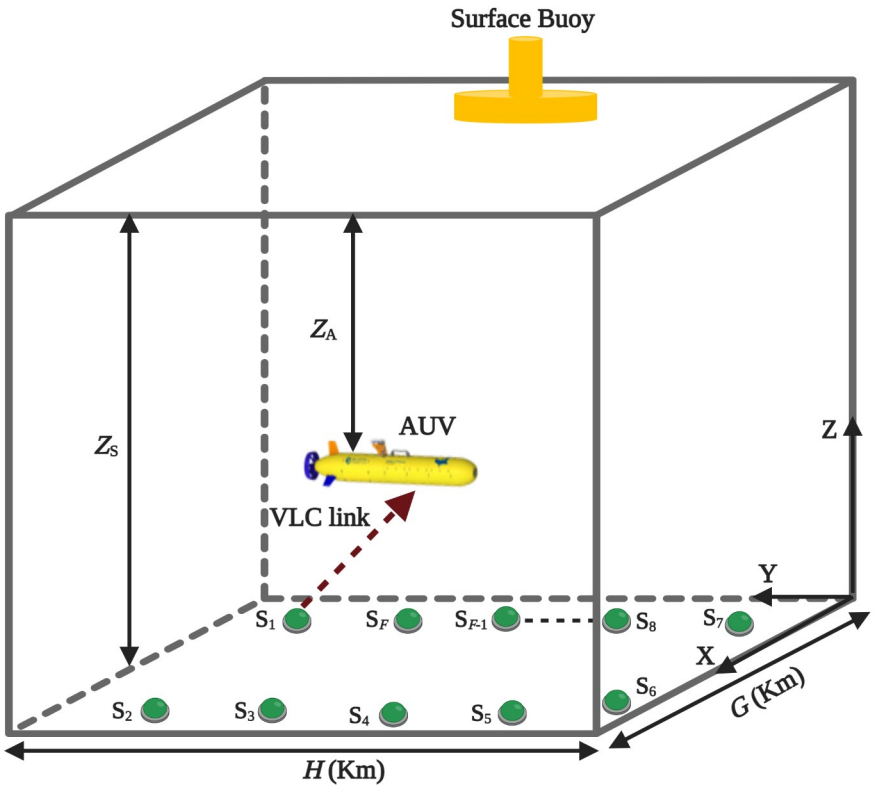


Figure 15: AUV-assisted USN

3.2.2 Energy Consumption Model

The power consumption of an AUV in each time slot n can be calculated by the summation of propulsion power $\Phi_{\text{prop}}$and hotel load Φ_{H} as [68]g

$$\Phi_{\text{A}}[n] = \Phi_{\text{prop}}[n] + \Phi_{\text{H}} \tag{3.2}$$

Hotel load is the power consumed by all subsystems other than propulsion and can be typically ignored with respect to Φ_{prop} [69]. Propulsion power can be calculated as [70]

$$\Phi_{\text{prop}}[n] = \frac{\rho}{2\eta_{\text{p}}} C_{\text{D}} A_{\text{s}} \|v_{\text{A}}\|^3 \tag{3.3}$$

where ρ is the density of water, η_{p} is the efficiency of the propulsion system, and C_{D} is the drag coefficient of the AUV. A_{s} is the wetted surface area of the AUV and is given by [68]

$$A_{\mathrm{s}} = 2\pi \frac{{D_{\mathrm{s}}}^2}{4} \left(1 + \frac{L}{D_{\mathrm{s}}\sqrt{1-{D_{\mathrm{s}}}^2/L^2}} \sin^{-1}\left(\sqrt{1-{D_{\mathrm{s}}}^2/L^2}\right)\right) + A_{\mathrm{wings}} \tag{3.4}$$

where $D_{\mathrm{s}} = \sqrt{6m/\rho\pi L}$, is the mass, is the length of the AUV, and A_{wings} is the surface area of the AUV's wings.

The total energy consumption of the AUV to complete the mission (i.e., visiting F sensors in the mission area) can be calculated as

$$E_{\mathrm{tot}} = \sum_{i=1}^{F} \sum_{n=1}^{Q} \Phi_{\mathrm{A}}[n] \Delta t_i[n] \tag{3.5}$$

3.2.3 Communication Model

Each sensor is equipped with a VLC transmitter while the AUV is equipped with a PD as the VLC receiver. We assume an intensity modulation-direct detection (Intensity Modulation (IM)/Direct Detection (DD)) system. The transmitted optical signal goes through the underwater propagation medium and reaches the destination. Based on the Beer Lambert formula [71], the path loss term between the AUV and S_i is given by

$$h_i[n] = \exp\left(-c d_i[n]\right), \; n = 1, 2, ..., Q \tag{3.6}$$

where c is the extinction coefficient and $d_i[n] = \|\mathbf{p}_{\mathrm{A}_i}[n] - \mathbf{p}_{\mathrm{S}_i}\|$ is the link distance between the AUV and S_i in the n^{th} time slot.

A closed-form expression for information rate in IM/DD systems is not available in the literature [72]. A lower bound of the information rate (in bits/s/Hz) is expressed as [73]

$$R_i[n] \geq \frac{1}{2}\log_2\left(1 + \frac{e}{2\pi}\left(\frac{r h_i[n] P_t}{\sigma}\right)^2\right) \tag{3.7}$$

where r is the detector responsivity, P_{t} is the transmit power, and $\sigma^2 = N_0 B$ is the noise variance. Here, B is bandwidth of the receiver, and N_0 is the noise power spectral density.

3.2.4 Optimization Problem Formulation

Since the AUV speed is assumed to be constant, the time-optimal trajectory is equal to energy-optimal trajectory [18]. In other words, our optimization problem reduces to the minimization of mission time. Let $T = \sum_{i=1}^{F} T_i$ denote the mission time which defines the total travel time starting from the first sensor node S_1 and returning to it after completing the mission. Let

$\mathbf{P}_{\mathrm{A}} = [\mathbf{p}_{\mathrm{A}_1}[1]\,\mathbf{p}_{\mathrm{A}_1}[2]...\mathbf{p}_{\mathrm{A}_1}[Q]\,\mathbf{p}_{\mathrm{A}_2}[1]\,\mathbf{p}_{\mathrm{A}_2}[2]...\mathbf{p}_{\mathrm{A}_2}[Q].....\mathbf{p}_{\mathrm{A}_F}[1]\,\mathbf{p}_{\mathrm{A}_F}[2]...\mathbf{p}_{\mathrm{A}_F}[Q]\,\mathbf{p}_{\mathrm{A}_1}[1]]$

denote the AUV trajectory. Accordingly, we can express the optimization problem as

$$\begin{aligned} &\min_{\mathbf{p}_{\mathrm{A}}} T = \sum_{i=1}^{F}\sum_{n=1}^{Q} \Delta t_i[n] \\ &\text{s.t. } \mathrm{C}: R_i[n] \geq R_{\mathrm{th}} \end{aligned} \tag{3.8}$$

The constraint imposes a minimum required data rate (denoted by R_{th}) for transfer between the AUV and each sensor node. Therefore, the AUV needs to be at a certain distance d_{th} from the sensor nodes to satisfy this condition, i.e., $\|\mathbf{p}_{\mathrm{A}_i}[n] - \mathbf{p}_{\mathrm{S}_i}\| \leq d_{\mathrm{th}}$. Based on previous equations, we can obtain d_{th} as

$$d_{\mathrm{th}} \leq \frac{1}{2c} \ln \left[\left(\frac{2\pi\sigma^2}{er^2 P_{\mathrm{t}}} \left(2^{R_{\mathrm{th}}} - 1\right) \right)^{-1} \right] \tag{3.9}$$

To find the optimal solution of Eq. (3.8), first, we determine the optimum sequence order of the sensor nodes to be visited, which can be considered as a large-scale trajectory optimization. Once the order of sensor node visits is determined, we deal with the small-scale optimization problem that optimizes the path between each pair of adjacent nodes to minimize the overall mission time. It should be noted that if ocean currents are ignored, our solution reduces to large-scale optimization. For large-scale optimization, we formulate the problem as a TSP to minimize the mission time assuming direct path between two nodes [74]. For the solution of TSP, we use the Genetic Algorithm (GA) toolbox in MATLAB [75] which yields the order of sensor node visits. Then, for the determined order of sensor nodes, we numerically solve Eq. (3.8) using fmincon function of the MATLAB

Table 4: System and channel parameters

Parameter	**Variable**	**Value**
Mission area	G×H (Km^2)	20×20 [73]
Number of sensor nodes	F	20
Depth of the sensors	Z_{s} (m)	250
Number of time slots	N	20
Mean of ocean current speed	α (m/s)	0.6 [71]
Variance of ocean current speed	β	0.01 [18]
Transmit power	P_{t} (W)	0.01 [77]
Detector responsivity	r	0.5 [77]
Noise power spectral density	N_0 (W/Hz)	10^{-19} [77]
Bandwidth of the receiver	B (MHz)	100
Extinction coefficient for clear ocean	c (m^{-1})	0.15 [77]

optimization toolbox [76]. This function is based on the trust-region algorithm and is defined to carry out the optimization by using the present information and to then repeat the process over and over. Accordingly, with knowledge of the start and the endpoints of the movement and the underwater current speed in each time slot, the best trajectory between two sensor nodes is determined.

3.2.5 Results and Discussions

In this section, we present our numerical results for the optimal trajectory and discuss the energy and time savings made possible through the optimization. We consider an area of $G \times H = 20\,\mathrm{Km} \times 20\,\mathrm{Km}$ where the sensors are located at the seabed with a depth of $Z_{\mathrm{s}} = 250\,\mathrm{m}$ and the AUV swims at a fixed depth of $Z_{\mathrm{A}} = 220\,\mathrm{m}$. Unless otherwise stated, system and channel parameters are provided in . AUV specifications are further provided in . For the solution of TSP algorithm, the number of populations and the number of iterations in the genetic algorithm are set as 100 and 10000, respectively.

In , we consider a USN where $F = 20$ sensor nodes are uniformly distributed on a rectangular grid pattern. As a benchmark, we include the case where AUV follows a straight trajectory between each two nodes as illustrated in Figure 15. a (i.e., this is

Table 5: Specifications of the AUV

Parameter	**Variable**	**Value**
Length of the AUV	L (m)	1.8 [78]
Mass of the AUV	m (kg)	50 [78]
Diameter of the AUV	D_{s} (m)	0.2 [78]
Wetted surface area	A_{s} (m^2)	47.18 [78]
Drag coefficient	C_{D}	0.0064
Efficiency of the propulsion system	η_{p} (%)	100
Velocity of the AUV	$\|\nu_{\mathrm{A}}\|$ (m/s)	0.5
Depth of the AUV	Z_{A} (m)	220
Water density	ρ ($\mathrm{Kg/m}^3$)	997

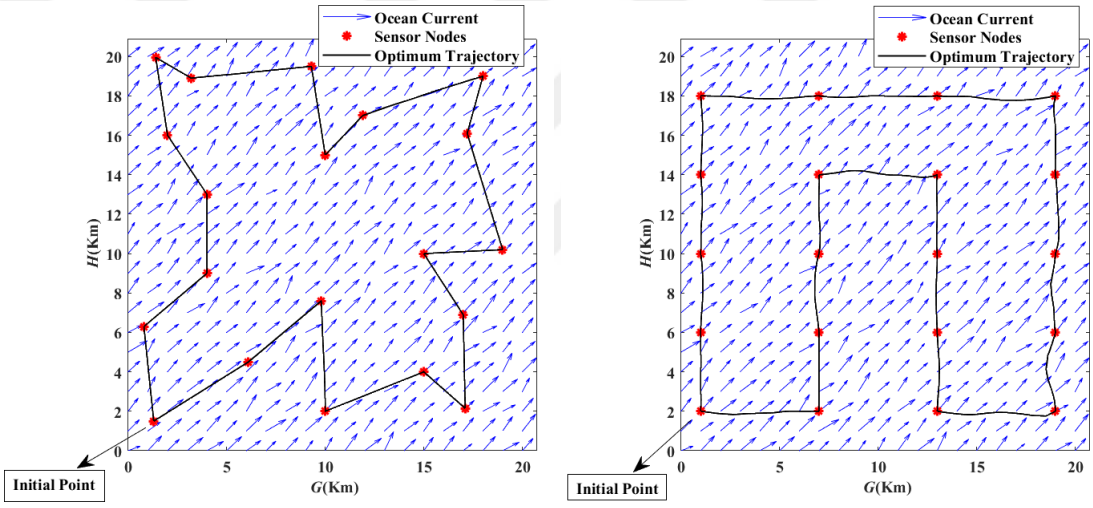


Figure 16: AUV trajectories for uniformly distributed sensors: a) Straight trajectory (i.e., only large-scale optimization), b) Optimum trajectory.

simply based on the large-scale optimization results). Under the assumption of AUV velocity of $\|\nu_{\mathrm{A}}\| = 0.5\,\mathrm{m/s}$, it takes $T = 60$ hours to complete the mission, which means $E_{tot} = 4.06\,\mathrm{MJ}$ of energy consumption. Our proposed trajectory found from the solution of Eq. (3.8) on page 42 is presented in Fig. 16(b). It is observed that the AUV does not any longer follow a straight path because the AUV selects its path reactive to ocean currents. In particular, the AUV avoids to swim towards the opposite direction of ocean currents whenever possible to save energy. Using the proposed trajectory, it takes $T = 57.5$ hours and $E_{tot} = 3.91\,\mathrm{MJ}$ of energy consumption to complete the mission. Comparison with the

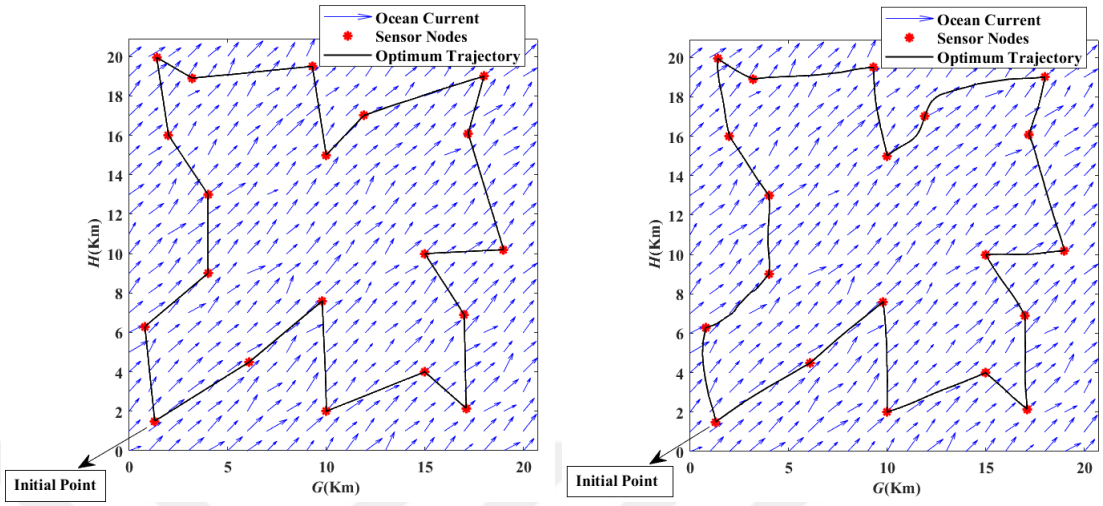


Figure 17: AUV trajectories for randomly distributed sensors: a) Straight trajectory (i.e., only large-scale optimization), b) Optimum trajectory.

benchmark in Fig. 16(a) demonstrates that the AUV saves 2.5 hours to complete its mission, which means 169 KJ of saving energy. This obviously indicates the superiority of the proposed trajectory.

In Fig. 17, we consider an USN where $F = 20$ sensors are randomly distributed. The results in the following are obtained based on averaging over 100 trials while the figure shows only one trial as an example. In each trial, we change the location of randomly distributed sensor nodes while the ocean currents distribution remains the same. For the AUV velocity of $\|v_{\mathrm{A}}\| = 0.5\,\mathrm{m/s}$, it takes $T = 57.5$ hours and $E_{\mathrm{tot}} = 3.89\,\mathrm{MJ}$ of energy consumption to complete the mission for straight trajectory (i.e., only large-scale optimization which effectively ignores the ocean currents). This reduces to $T = 54.9$ hours and $E_{\mathrm{tot}} = 3.72\,\mathrm{MJ}$ for the proposed trajectory. This indicates an average of 2.6 hours reduction in the mission time and an average energy saving of 180 KJ.

In Fig. 18 on the following page, we investigate the effect of number of sensor nodes on the energy consumption and mission time. Results are averaged of 100 trials and the same conditions in Fig. 17 are considered. The number of sensor nodes ranges from $F = 5\,\mathrm{to}\,F = 50$ .For $F = 5$ sensor nodes, the mission time and the corresponding energy

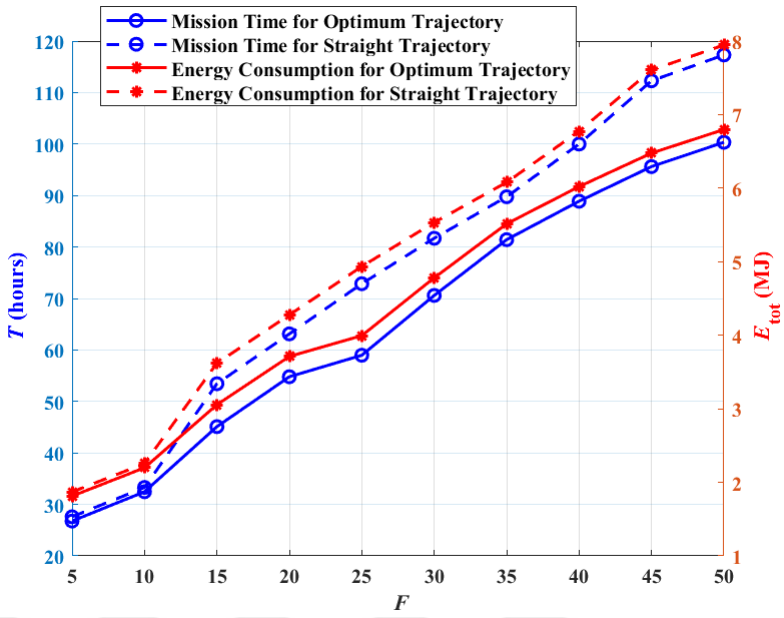


Figure 18: Effect of the number of sensor nodes on the mission time and energy consumption

consumption for the straight trajectory are respectively $T = 27.6$ hours and $E_{\text{tot}} = 1.86\,\text{MJ}$. These reduce to $T = 26.7$ hours and $E_{\text{tot}} = 1.81\,\text{MJ}$ for the proposed trajectory. This indicates an improvement of 3.3 % in travel time and 2.7 % in energy consumption. For $F = 50$ sensor nodes, it requires $T = 117.3$ hours and $T = 100.1$ hours respectively for straight and optimum trajectories, indicating an improvement of 14.7 % in travel time. We have $E_{\text{tot}} = 7.94\,\text{MJ}$ and $E_{\text{tot}} = 6.7\,\text{MJ}$ for straight and proposed trajectories which yields an improvement of 15.6 % in energy consumption. It can be readily checked that the improvement increases as the number of sensor nodes increases.

In Fig. 19 on the following page, we investigate the effect of AUV's velocity on the energy consumption and mission time. Other assumptions are the same as in those in Fig. 17 on the previous page. It is observed that as the velocity increases, the mission time decreases while the energy consumption increases. For example, the mission time for $\|v_{\text{A}}\| = 4\,\text{m/s}$ is $T = 6.2$ hours which is 48.3 hours less than that in $\|v_{\text{A}}\| = 0.5\,\text{m/s}$ (considered in Fig. 17 on the preceding page). Accordingly, the energy consumption reaches to $E_{\text{tot}} = 213\,\text{MJ}$ from $E_{\text{tot}} = 3.72\,\text{MJ}$. This also indicates the need to determine a trade-off

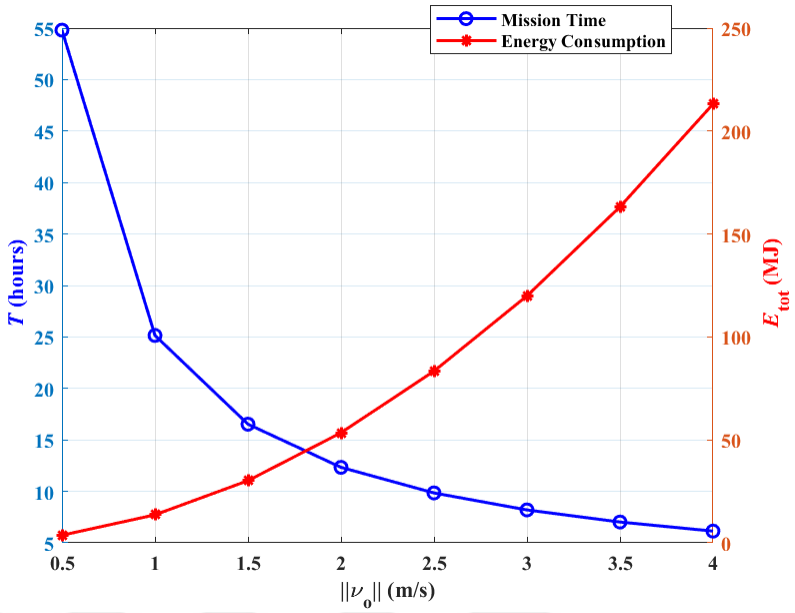


Figure 19: Effect of AUV velocity on the mission time and energy consumption (Only optimal trajectory is considered.)

between the energy and mission time requirements. For the given scenario under consideration, it can be readily checked from Figure 18 that $\|\nu_A\| = 1.8\,\mathrm{m/s}$ gives such a good trade-off where the plots of mission time and energy consumption intersect.

3.3 3D Trajectory Optimization of Solar Powerered AUVs

While an AUV-assisted USN offers significant advantages in network operations such as data collection and localization, the introduction of mobile nodes presents challenges such as sophisticated trajectory planning and energy-efficient operation of AUVs whose mission time are mainly limited with battery capacity. Energy consumption is also related to the type of deployed AUVs. Propelled AUVs can reach higher speeds, but their power consumption can be large due to the continuous use of propeller engine [19]. In contrary, non-propelled AUVs (gliders) use little to no power, but operate at much lower speeds [20]. Floating up and diving in operations in non-propelled AUVs is also possible by changing their buoyancy with little power consumption [21]. Hybrid versions [22] use their buoyancy engine for floating up and diving and use their propeller engine for going forward. In the

operation of AUVs, the main power consumption source is therefore propeller engine. The choice of trajectories therefore directly impacts the mission time and energy consumption.

Since the energy efficiency of predefined trajectories [79–83] remains low in particular for large mission areas with randomly distributed sensor nodes, recent efforts on trajectory optimization have focused on reactive trajectories [84–88] where the AUV path is corrected in real-time and refined to cope the sudden changes during the operation. In [84–87], assuming acoustic signaling for data transmission, trajectory planning of the data mule AUVs is formulated as a TSP to minimize the AUV's travel time [84, 85], or to maximize the VoI from the sensors [86, 87]. In [88], assuming VLC for data transmission, the trajectory finding problem of the AUV is solved using a greedy algorithm under VoI constraints. While the works in [84–88] simply assume that the AUV follows a straight path between each two sensor nodes, our previous work [23] further considers the effect of ocean currents and optimizes the trajectory between each two nodes.

The underlying assumption in above works [23, 79–88] is that the AUV is battery powered. Battery-powered AUVs are required to return to the shore or the support vessel after a certain period in order to get recharged whether or not their mission is complete. Solar-powered AUVs have been further proposed for long term deployments to address the energy limitations of battery-powered counterparts [23]. They can harvest power from the sun light and use the harvested power to perform the mission or to store it for later use. In the current literature [23, 24], it is commonly assumed that the solar-powered AUV resurfaces in the daylight hours and recharges its batteries using the solar energy on the water surface while conducting its assigned mission during the night time hours. However, the recent progress of solar cell technology enables to efficient harvest of sunlight for submerged nodes [25]. This therefore makes possible the solar-powered AUVs to harvest energy during its mission.

In previous works where battery-powered AUVs are considered [23, 79–88], the energy consumption is mainly related to the mission trajectory defined to cover a given area of

interest. EH aware trajectory optimization for solar-powered AUVs might indicate a conflicting trajectory to maximize the harvested energy, e.g., being closer to sea surface. In our work, we formulate 3D trajectory optimization for solar-powered AUVs with the goal of maximizing the harvested energy under constraints imposed by the data transmission. The optimization constraints include a fixed amount of data to be retrieved by the AUV from each node, therefore a corresponding transmission spectral efficiency and time duration. We formulate the problem as a bilevel optimization problem. The lower-level objective function is TSP which determines the optimum sequence order of the sensor nodes to be visited while the upper-level objective function is the optimization of the trajectory between each pair of adjacent nodes for the given order of node visits. Our numerical results demonstrate that the proposed trajectory significantly prolongs the mission time and autonomous operation of solar-powered AUV without the need to return to the home base.

3.3.1 Motion Model

As illustrated in Figure 20 on the next page, we consider a 3D USN scenario that covers a marine area of $X\,(\mathrm{km}) \times Y\,(\mathrm{km}) \times Z\,(\mathrm{km})$. It consists of a total of F randomly distributed sensor nodes, S_i $i = 1, 2, ..., F$, with position vector $\mathbf{p}_{\mathrm{S}_i} = (x_{\mathrm{S}_i}, y_{\mathrm{S}_i}, z_{\mathrm{S}_i})$ anchored to the bottom of the sea with different heights. It is assumed that the three-dimensional underwater space map and the sensors' locations are readily available at the AUV (Commercially available solutions are available, see e.g., [89], [90] for underwater positioning and navigation.

We assume the deployment of a hybrid AUV [22] which has both propeller engine and buoyancy engine. It uses propeller engine to operate at relatively high speeds while it uses buoyancy engine to glide (i.e., float up and dive in) [21]. As illustrated in Figure 21 on page 51, the AUV is assumed to operate in four different modes, namely *communication*, *floating*, *thrust*, and *diving*, modes which are elaborated below:

- **Communication mode**: When the AUV visits a sensor node for data gathering, it switches to the communication mode during which it maintains a certain distance

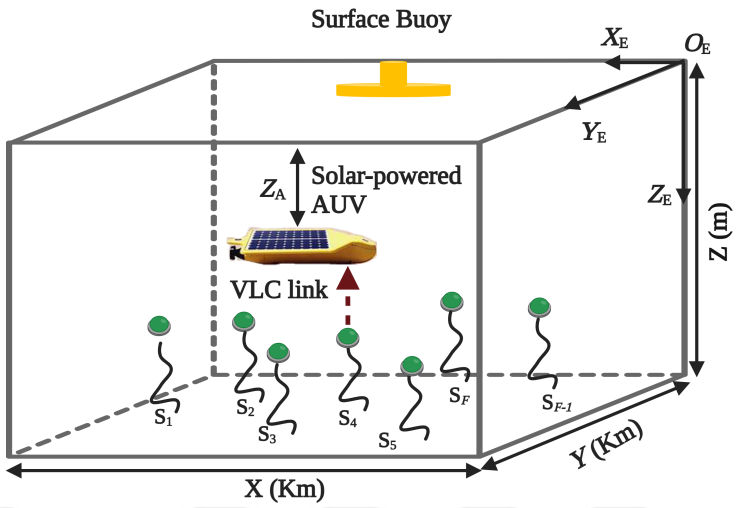


Figure 20: Solar powered AUV assisted USN under consideration.

with the sensor node during the data transfer. In this mode, the buoyancy of the vehicle is made equal to the buoyancy of the water at the desired depth [21], known as "neutrally buoyant" position to keep the AUV (nearly) motionless.

- **Floating mode**: After the communication link is terminated, the AUV uses buoyancy engine to climb up. For this purpose, the vehicle's buoyancy is made less than that of the seawater so that the vehicle can float up to reach a desired depth [21].

- **Thrust mode**: In the thrust mode, the AUV uses its propeller engine to go forward. During this mode, it possesses a high maneuverability capability but at the cost of consuming more power for the operation [19].

- **Diving mode**: To visit the next sensor node, the AUV stops the propeller engine and uses the buoyancy engine for diving. For this purpose, the vehicle's buoyancy is made greater than that of the seawater so that the vehicle can dive down to reach a desired depth [21].

Assume that the AUV starts from the node S_1, which is the closest node to its home base (i.e., support vessel, port, etc). Let $\mathbf{S} = \left(S_{1,1}, S_{2,i}, ..., S_{k,i}, ..., S_{F,i}\right)\ i \in \{2, ..., F\}$ denote the vector that describes the optimal sequence order of sensor node visits (see Section 3.3.4

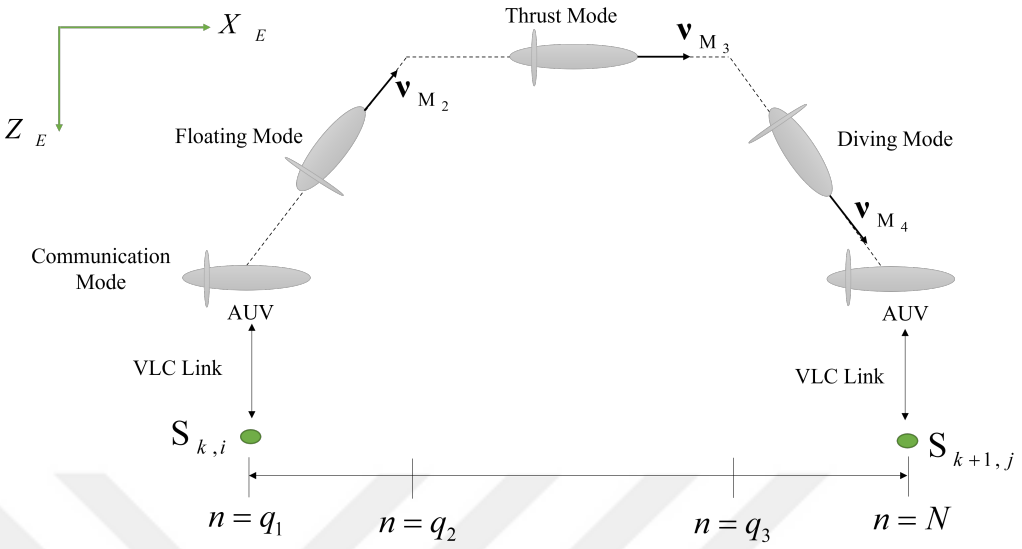


Figure 21: Operation modes of AUV.

for the related optimization). For example, $S_{k,i}$ indicates that the sensor S_i was visited in the k^{th} order. Let $T = \sum_{k=1}^{F} T_k$ denote the mission time of AUV where T_k is the travel time from the sensor $S_{k,i}$ to the sensor $S_{k+1,j}$, $k = 1,2,...,F$, $j \neq i$, $j = 1,2,...,F$. This is divided into N equal-length time slots each with a duration of $\delta t_k[n] = T_k/N$. If δt_k is chosen sufficiently small, the location of the AUV can be assumed to be fixed during each time slot. The position of the AUV during its travel from $S_{k,i}$ to $S_{k+1,j}$ can be therefore described by the vector $\mathbf{p}_{A,k}[n] = \left(x_{A,k}[n], y_{A,k}[n], z_{A,k}[n]\right)$, $n = 1,2,..,q_1,..,q_2,..,q_3,..,N$ where q_1, q_2, q_3, and N denote switching times between different modes of operation (see Figure 20). Let $v_M[n] = \left(v_{M,x}[n], v_{M,y}[n], v_{M,z}[n]\right)$ denote the velocity of the AUV for a given operation mode $M \in \{M_1, M_2, M_3, M_4\}$ where M_1, M_2, M_3, and M_4 respectively denote communication, floating, thrust, and diving modes. It can be noted that the vehicle remains nearly motionless in the communication mode, i.e., $v_{M_1}[n] = (0,0,0)$ (The AUV may be subject to sways due to ocean currents and other disturbances in underwater environments which cannot be completely compensated by the buoyant engine. This may result

in pointing errors as a result of misalignment between transmitter and receiver. Pointing-acquisition-tracking (PAT) methods can be used [91] to handle such residual pointing errors). Therefore, we can formulate the AUV state as

$$\mathbf{p}_{\mathrm{A},k}[n] = \begin{cases} \mathbf{p}_{\mathrm{A},k}[n-1], n = 1,2,...,q_1 \\ \mathbf{p}_{\mathrm{A},k}[n-1] + (\mathbf{v}_{\mathrm{o}}[n] + \mathbf{v}_{\mathrm{M}_2}[n])\,\delta t_k[n],\ n = q_1,...,q_2 \\ \mathbf{p}_{\mathrm{A},k}[n-1] + (\mathbf{v}_{\mathrm{o}}[n] + \mathbf{v}_{\mathrm{M}_3}[n])\,\delta t_k[n],\ n = q_2,...,q_3 \\ \mathbf{p}_{\mathrm{A},k}[n-1] + (\mathbf{v}_{\mathrm{o}}[n] + \mathbf{v}_{\mathrm{M}_4}[n])\,\delta t_k[n],\ n = q_3,...,N \end{cases}, \tag{3.10}$$

where $\mathbf{v}_{\mathrm{o}}[n] = [v_{\mathrm{o},x}[n], v_{\mathrm{o},y}[n], v_{\mathrm{o},z}[n]]$ is the random vector quantifying the ocean current speed [22]. Specifically, $v_{\mathrm{o},x}[n]$ and $v_{\mathrm{o},y}[n]$ are modeled as independent Gaussian random variables with mean value of α and variance of β. Since the velocity of the ocean currents in the Z_{E} direction is negligible, $v_{\mathrm{o},z}[n]$ is assumed to be zero [92].

3.3.2 Energy Consumption Model

The power consumption is calculated as the summation of power consumed for the movement of the vehicle and the power consumed by all other subsystems (i.e., communication, control, lighting, etc.) other than movement. The latter is called "hotel load" and is a negligible amount compared to the power consumption of the propeller engine [93]. Therefore, we assume the consumed power during communication mode is zero, i.e., $\Phi_{\mathrm{out}}[n] = 0$ for $n = 1,2,...,q_1$. In floating and diving modes, the power consumption for the vehicle's movement in the gliding process is the power used to pump the water in and out of the density control chamber to change the buoyancy and can be assumed negligible (In [94], assuming a velocity of $v_{\mathrm{M}_2} = v_{\mathrm{M}_4} = 0.4\,\mathrm{m/s}$ during floating and diving modes and a depth of $z_{\mathrm{A}} = 200\,\mathrm{m}$, the average energy consumption is reported to be less than 20 KJ. This is magnitudes of orders smaller than the energy consumption in the thrust mode (which is in the order of tens of MJ) and can be safely neglected in the analysis). Therefore, we have $\Phi_{\mathrm{out}}[n] = 0$ for $n = q_1,...,q_2$ and $n = q_3,...,N$. In the thrust mode, assuming that the AUV

moves with a constant speed [19], the consumed power is constant during each time slot and is given by

$$\Phi_{\text{out}} = \frac{\rho}{2\eta_{\text{p}}} C_{\text{D}} A_{\text{s}} \|v_{\text{M}_3}\|^3 , \tag{3.11}$$

where $\|.\|$ denotes the Euclidean vector norm, η_{p} is the efficiency of the propulsion system, ρ is the density of the water, and C_{D} is the drag resistance coefficient. In Eq. (3.11), A_{s} is the wetted surface area of the AUV and is given by [95]

$$A_{\text{s}} = 2\pi \frac{{D_{\text{s}}}^2}{4} \left(1 + \frac{L}{D_{\text{s}}\sqrt{1-{D_{\text{s}}}^2/L^2}} \sin^{-1}\left(\sqrt{1-{D_{\text{s}}}^2/L^2}\right)\right) + A_{\text{wings}}, \tag{3.12}$$

where $D_{\text{s}} = \sqrt{6m/\rho\pi L}$, m is the mass, L is the length of the AUV, and A_{wings} is the surface area of its wings.

The energy consumption in each time slot is

$$E_{\text{out},k}[n] = \Phi_{\text{out}} \delta t_k [n] \cdot \tag{3.13}$$

The total energy consumption of the AUV to complete the mission (i.e., visiting F sensors in the mission area) is then calculated as $E_{\text{out}} = \sum_{k=1}^{F} \sum_{n=q_2}^{q_3} E_{\text{out},k}[n]$.

3.3.3 Communication Model

Either LEDs or LDs can be used as transmitters in underwater VLC systems. LEDs can provide relatively lower data rates as compared to LD-based systems. However, their divergence angle can relax the PAT requirements [96]. Based on the intended data rate and the level of PAT sub-system complexity that can be afforded, both light sources can be used. While the location information of sensor nodes is available at the AUV based on a three-dimensional underwater space map, it still needs to scan an uncertainty region centered about this initial position estimate [97] before the optical communication link can be established. After the sensor node is located, the AUV points its aperture towards the node and initiates the data transfer.

The spectral efficiency of VLC link (in bits/sec per unit bandwidth) is given by [98]

$$R_k[n] \geq \frac{1}{2}\log_2\left(1+\frac{e(rh_k[n]P)^2}{2\pi\sigma^2}\right), \tag{3.14}$$

where r is the detector responsivity, P is the transmit power, and σ^2 is the noise variance. In Eq. (3.14), $h_k[n]$ is the path loss between the AUV and the sensor node $\mathrm{S}_{k,i}$ and is given by [99]

$$h_k[n] = \exp\left(-cd_{\mathrm{A},k}[n]\right), \tag{3.15}$$

where $d_{\mathrm{A},k}[n] = \left\|\mathbf{p}_{\mathrm{A},k}[n] - \mathbf{p}_{\mathrm{S}_{k,i}}\right\|$ is the link distance between the AUV and the sensor node $\mathrm{S}_{k,i}$. The communication mode spans a total of $t_{\mathrm{M}_1,k} = \sum_{n=1}^{q_1}\delta t_k[n]$ seconds during which the AUV stops and extracts data from the node. Given the link bandwidth of B, the retrieved data (in terms of bits) for this duration is

$$\Im_k = BR_k t_{\mathrm{M}_1,k}. \tag{3.16}$$

Let $\Im_{\mathrm{sc}}$ denote the storage capacity of each sensor node. The link parameters ($t_{\mathrm{M}_1,k}$ and R_k) need to be selected to support this data retrieval, i.e., $\Im_k = \Im_{\mathrm{sc}}$.

3.3.4 Optimization Problem Formulation

As described in the previous section, the AUV visits F sensor nodes and returns to the initial point after completing the mission. It takes N time slots to visit from one sensor node to the other. Therefore, the AUV's trajectory is defined by

$$\mathbf{P}_{\mathrm{A}} = \left\{ \underbrace{\mathbf{p}_{\mathrm{A},1}[1]\ldots\mathbf{p}_{\mathrm{A},1}[N]}_{\text{Firstnode}} \ldots \underbrace{\mathbf{p}_{\mathrm{A},k}[1]\ldots\mathbf{p}_{\mathrm{A},k}[N]}_{k^{\text{th}}\text{node}} \ldots\ldots \underbrace{\mathbf{p}_{\mathrm{A},F}[1]\ldots\mathbf{p}_{\mathrm{A},F}[N]}_{F^{th}\text{node}} \underbrace{\mathbf{p}_{\mathrm{A},1}[1]\ldots\mathbf{p}_{\mathrm{A},1}[N]}_{\text{Firstnode}} \right\}. \tag{3.17}$$

Let Q_{b} denote the initial battery energy (i.e., energy level at the start of the mission). The overall available energy in each time slot is $E_{\mathrm{c},k}[n] = Q_{\mathrm{b}} + E_{\mathrm{in},k}[n]$. We define the net energy at each time slot as

$$E_{\mathrm{net},k}[n] = E_{\mathrm{c},k}[n] - E_{\mathrm{out},k}[n]. \tag{3.18}$$

In our work, we aim to maximize the net energy defined as $E_{\text{net}} = \sum_{k=1}^{F} \sum_{n=1}^{N} E_{\text{net},k}[n]$. It is obvious that E_{net} is directly affected by the visit sequence of sensor nodes and the path followed between two consecutive nodes. We formulate the problem as a bilevel optimization problem. The lower-level objective function is the minimization of the mission length d_{tot}. It is defined as

$$d_{\text{tot}} = \sum_{i=1}^{F} \sum_{j \neq i, j=1}^{F} d_{ij} b_{ij}, \tag{3.19}$$

where $d_{ij} = \left\| \mathbf{p}_{\text{S}_i} - \mathbf{p}_{\text{S}_j} \right\|$ is the distance between sensor nodes S_i and S_j $j \neq i$, $j = 1, 2, ..., F$. b_{ij} is set as 1 when there is a path between sensor S_i to sensor S_j, otherwise set as $b_{ij} = 0$. The upper-level objective function is maximization of the net energy, E_{net}, during the mission for the optimized sequence order of node visits obtained from the lower-level optimization. Mathematically speaking, we have

$$\begin{aligned} &\max_{\mathbf{p}_{\text{A}}} \; E_{\text{net}} \\ &\text{s.t.} \;\; \text{C1} : \Im_k = \Im_{\text{sc}}, \qquad \forall k = 1, ..., F \\ &\qquad\quad \text{C2} : \Phi_{\text{in},k}[n] \geq \Phi_{\text{th}}, \; \forall n = q_2, ..., q_3 \end{aligned} \quad , \tag{3.20}$$

where the optimal visit sequence of sensor nodes is obtained from

$$\begin{aligned} &\min_{\mathbf{b}} \; d_{\text{tot}} \\ &\text{s.t.} \;\; \text{C3} : \sum_{j=1, j\neq i}^{F} \sum_{i=1}^{F} b_{ij} = 1 \,, \; \sum_{i=1, i\neq j}^{F} \sum_{j=1}^{F} b_{ij} = 1 \\ &\qquad\quad \text{C4} : \sum_{i \in \Xi} \sum_{j \neq i, j \in \Xi} b_{ij} \leq |\Xi| - 1, \; \forall \Xi \subseteq \{1, 2, ..., F\} \end{aligned} \quad . \tag{3.21}$$

The constraint C1 imposes that the full amount of data stored on each sensor node is completely retrieved during the period of communication mode. The transmission time duration ($t_{\text{M}_1,k}$) and transmission spectral efficiency (R_{th}) should be selected to support this data retrieval. For a fixed value for R_{th}, the required time duration for data transfer can be obtained using Eq. (3.16) on the previous page. To achieve the selected value of R_{th}, the AUV needs to maintain a certain distance of d_{th} from the sensor nodes, i.e., $\left\| \mathbf{p}_{\text{A},k} - \mathbf{p}_{\text{S}_{k,i}} \right\| = d_{\text{th}}$ during these $t_{\text{M}_1,k}$ seconds. Based on Eq. (3.14) on the preceding page and Eq. (3.15)

on page 54, we can write

$$d_{\text{th}} \leq \frac{1}{2c} \ln \left[\left(\frac{2\pi\sigma^2}{er^2P} \left(2^{2R_{\text{th}}} - 1 \right) \right)^{-1} \right]. \tag{3.22}$$

Accordingly, the operation depth of the AUV during the communication mode must satisfy $z_{\text{A,k}} \geq \Delta_{\min,k}$ where $\Delta_{\min,k}$ is given by

$$\Delta_{\min,k} = z_{\text{S}_{k,i}} - d_{\text{th}}. \tag{3.23}$$

The constraint C2 imposes a minimum required power (denoted by Φ_{th}), which dictates a maximum operation depth $\Delta_{\max}$ for the AUV in the thrust mode, i.e., $q_2 \leq n \leq q_3$, which is obtained as

$$\Delta_{\max} = \frac{1}{c} \ln \left(\frac{\Phi_{\text{th}}}{\xi \kappa \Psi_{0,\text{water}} \cos(\Omega)} \right)^{-1}. \tag{3.24}$$

Constraint C3 implies that each sensor is visited exactly once. In constraint C4, Ξ is any sequence of sensor nodes that can form a sub-tour instead of one single tour. It enforces that there is only a single tour covering all sensor nodes, and not multiple disjointed tours.

The lower level objective function is in the form of a TSP, which is an NP-hard problem [100]. It can be solved using nearest neighbor (or greedy) algorithms [82], [88] or evolutionary algorithms such as the genetic algorithm [101], particle swarm optimization [102], and ant colony algorithm [103]. Here, we use genetic algorithm due to the fact that the crossover feature of genetic algorithm makes it more powerful than other evolutionary algorithms in solving TSP [104]. The genetic algorithm relies on a population of individuals that simultaneously explores the search space and generates new solutions by recombining individuals of the current population. The output of lower-level optimization is a matrix with zero and one entry from which we extract the sequence order of sensor nodes to be visited and therefore construct the vector. Let $\mathbf{b}$ denote a matrix containing the

information on the sequence order of sensor nodes to be visited. It is given by

$$\mathbf{b} = \begin{pmatrix} b_{11} & \cdots & b_{1j} & \cdots & b_{1F} \\ \vdots & \vdots & \vdots & \vdots & \vdots \\ b_{i1} & \cdots & b_{ij} & \cdots & b_{iF} \\ \vdots & \vdots & \vdots & \vdots & \vdots \\ b_{F1} & \cdots & b_{Fj} & \cdots & b_{FF} \end{pmatrix}_{F\times F}, \tag{3.25}$$

where b_{ij} is set as 1 when there is a path between sensor S_i to sensor S_j, and set as $b_{ij} = 0$ otherwise. As an example, to obtain components of $\mathbf{S}$, (i.e., $\mathrm{S}_{k,i}$, $k = 1,2,...,F$, $i = 1,2,...,F$), we sort the non-zero entries of matrix $\mathbf{b}$ as follows

$$\mathbf{b} = \begin{pmatrix} 0 & 1 & 0 & \cdots & 0 & 0 \\ 0 & 0 & 0 & \cdots & 1 & 0 \\ \vdots & \vdots & \vdots & \vdots & \vdots & \vdots \\ 0 & 0 & 0 & \ldots & 0 & 1 \\ 0 & 0 & 1 & \cdots & 0 & 0 \end{pmatrix}_{F\times F}$$

From the information given in the matrix $\mathbf{b}$, we extract the sequence order of nodes to be visited as $\mathbf{S} = (\mathrm{S}_{1,1}, \mathrm{S}_{2,2}, \mathrm{S}_{3,F-1}, ..., \ \mathrm{S}_{F-1,F}, \mathrm{S}_{F,3})$. For instance, $b_{12} = 1$ means that the AUV's optimum route is from sensor S_1 to the sensor S_2 ($\mathrm{S}_{1,1} \rightarrow \mathrm{S}_{2,2}$) and, $b_{2F-1} = 1$ means the AUV should go from sensor S_2 to the sensor S_{F-1} ($\mathrm{S}_{2,2} \rightarrow \mathrm{S}_{3,F-1}$) and so on.

Having the optimum sequence order of the sensor nodes, we solve the upper-level objective function of Eq. (3.20) on page 55 numerically using the fmincon function [105] of the MATLAB optimization toolbox. This function is based on the trust-region algorithm and is defined to carry out the optimization by using the present information and then repeating the process over and over until it reaches convergence. Accordingly, with knowledge of the start and the end points of the movement and the underwater current speed in each time slot, the best trajectory between the two sensor nodes is determined.

The flowchart of the proposed algorithm for trajectory planning is provided in . The inputs of the upper-level optimization problem include the number of sensor nodes (F),

Table 6: Flowchart for the proposed EH-aware trajectory planning algorithm

Initialization:
Set F, N, $\Delta_{\min,k}$, $\Delta_{\max}$, $\|v_{\mathrm{M}}\|$, $\Im_{\mathrm{sc}}$
$\mathbf{S} \leftarrow \left(\mathrm{S}_{1,1}, \mathrm{S}_{2,i}, ..., \mathrm{S}_{k,i}, ..., \mathrm{S}_{F,i}\right),\ i \in \{2, ..., F\}$
Update and finding the optimal solution:
for $k = 1$ to F
if $z_{\mathrm{A},k}[n] \geq \Delta_{\min,k}$
$\mathrm{M} \leftarrow \mathrm{M}_1$ (switch to communication mode), $n \leftarrow 1$
end if
if $\Im_k = \Im_{\mathrm{sc}}$ (number of received bits)
$\mathrm{M} \leftarrow \mathrm{M}_2$ (switch to floating mode), $n \leftarrow q_1$
end if
if $z_{\mathrm{A},k}[n] \leq \Delta_{\max}$
$\mathrm{M} \leftarrow \mathrm{M}_3$ (switch to thrust mode), $n \leftarrow q_2$
end if
for $n = q_2$ to $n = q_3$
Update and interpolate the ocean current vector fields $v_{\mathrm{o}}[n]$
$\delta t_k[n] \leftarrow \frac{\left\|\mathbf{p}_{\mathrm{A},k}[n] - \mathbf{p}_{\mathrm{A},k}[n-1]\right\|}{\|v_{\mathrm{o}}[n] + v_{\mathrm{M}}[n]\|}$
Update the upper-level optimization problem of (16)
Maximize E_{net}
$\mathbf{p}_{\mathrm{A},k}[n] \leftarrow \left(x_{\mathrm{A},k}[n], y_{\mathrm{A},k}[n], z_{\mathrm{A},k}[n]\right)$
end for
if $z_{\mathrm{A},k+1} \leq \Delta_{\min,k+1}$
$\mathrm{M} \leftarrow \mathrm{M}_4$ (switch to diving mode), $n \leftarrow q_3$
else if
$\mathrm{M} \leftarrow \mathrm{M}_1$, $n \leftarrow N$
end if
end for
Output: $\mathbf{P}_{\mathrm{A}}$

the number of time slots (N), the minimum required depth ($\Delta_{\min,k}$) to satisfy the data rate constraint, the maximum depth ($\Delta_{\max}$) to satisfy the minimum levels of harvested power, the storage capacity of sensor nodes ($\Im_{\mathrm{sc}}$), the velocity of the AUV ($\|v_{\mathrm{M}}\|$) in addition to the optimum sequence order of sensors to be visited. The optimum sequence order of sensor nodes (denoted by $\mathbf{S}$) is the output of the lower-level optimization problem and is stored on the AUV before the mission starts. During the mission, the AUV executes the solution of the upper-level optimization problem in real-time which deals with the optimization of the path between each two adjacent sensors. The AUV starts from sensor $\mathrm{S}_{1,1}$ which

is the closest node to the base station. Driven by buoyancy engine, the AUV adaptively adjusts its depth until it satisfies the threshold data rate ($z_{\mathrm{A},k} \geq \Delta_{\min,k}$). It then switches to the communication mode ($\mathrm{M} \leftarrow \mathrm{M}_1$). The AUV sends a wake-up signal for the sensor to establish the link and start transferring the data. After it retrieves $\Im_k = \Im_{\mathrm{sc}}$ bits, the node goes to sleep and the AUV switches to floating mode ($\mathrm{M} \leftarrow \mathrm{M}_2$) at $n = q_1$. Using a buoyancy engine, it floats up until it reaches a suitable depth near the water surface ($z_{\mathrm{A},k} \leq \Delta_{\max}$). At time slot $n = q_2$, it switches to thrust mode ($\mathrm{M} \leftarrow \mathrm{M}_3$) during which the AUV is driven by the propeller engine until time slot $n = q_3$. It then switches to diving mode ($\mathrm{M} \leftarrow \mathrm{M}_4$) and gets close to the next sensor node using the buoyancy engine. During this mode, it adjusts its depth taking into account the required transmission distance for data transfer. At time slot $n = N$ (when its distance to the next sensor node is close enough to satisfy the threshold data rate), it switches to communication mode again, and the same process will be repeated until it visits all the sensor nodes.

3.3.5 Results and Discussions

Unless otherwise stated, system and channel parameters are provided in while AUV specifications are further provided in . The populations and the number of iterations in the genetic algorithm are set as 100 and 10000, respectively. The storage capacity of each sensor node is $\Im_{\mathrm{sc}} = 256\,\mathrm{Mbits}$ [106]. Therefore, the total data to be collected from $F = 18$ sensor nodes is equal to $\Im_{\mathrm{sc}} = 4.608\,\mathrm{Gbits}$.

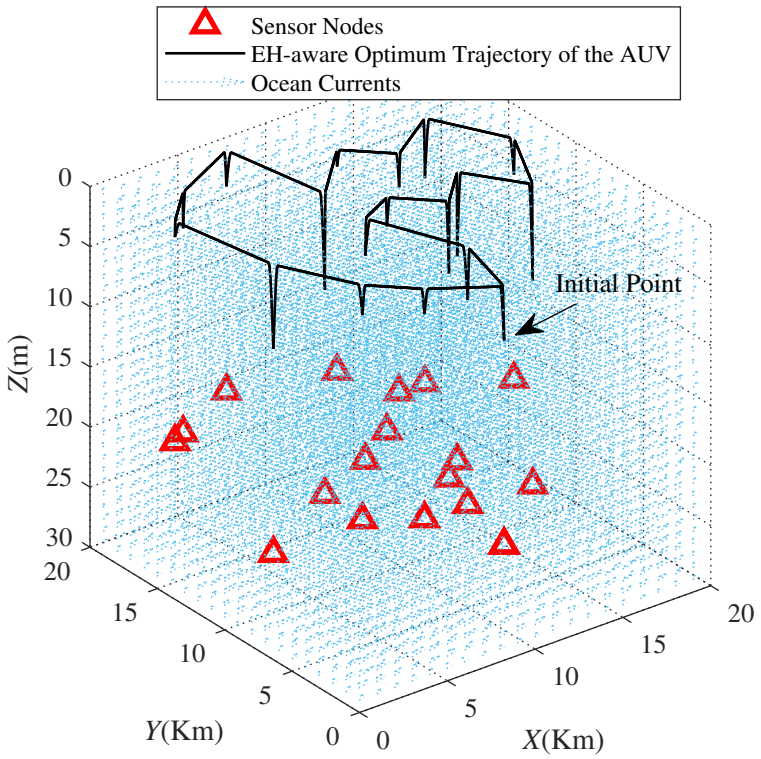
To demonstrate the benefits of trajectory optimization, we consider a coastal marine area with a size of $X \times Y \times Z = 20\,\mathrm{Km} \times 20\,\mathrm{Km} \times 30\,\mathrm{m}$ as an example with $F = 18$ sensors with location vectors provided in . We assume that the mission is done in Black Sea with latitude of $\vartheta = 41.8$ and longitude of $\theta = 37.6$, the date is June 28th ($\Theta = 180^{\mathrm{th}}$), the water is coastal type, and $w_{\max} = 11\,\mathrm{am}$. As discussed in the previous section, we first solve Eq. (3.21) on page 55 using genetic algorithm and obtain the optimum sequence order of sensor nodes as $\mathbf{S} = \big(\mathrm{S}_{1,1}, \mathrm{S}_{2,4}, \mathrm{S}_{3,2}, \mathrm{S}_{4,6}, \mathrm{S}_{5,5}, \mathrm{S}_{6,3}, \mathrm{S}_{7,17}, \mathrm{S}_{8,9}, \mathrm{S}_{9,10}, \mathrm{S}_{10,18}, \mathrm{S}_{11,8}, \mathrm{S}_{12,7},$

Table 7: System and channel parameters

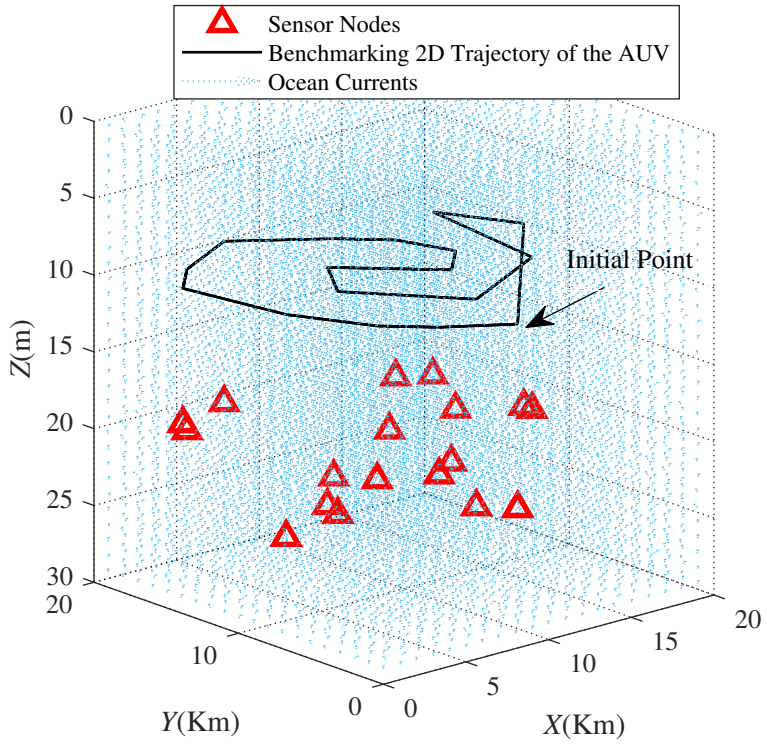
Parameter	Variable	Value
Mission area	$X \times Y \times Z$ (Km^3)	20×20×0.03
Number of sensor nodes	F	18
Number of time slots	N	1000
Mean of ocean current speed	$\alpha(\mathrm{m/s})$	0.6
Variance of ocean current speed	β	0.01
Transmit power	$P_{\mathrm{t}}(\mathrm{W})$	0.01
Detector responsivity	r	0.5
Noise variance	$\sigma^2(\mathrm{W})$	10^{-11}
Bandwidth of the channel	B (MHz)	100
Storage capacity of sensor nodes	$\Im_{\mathrm{sc}}$ (Mbits)	256
Minimum required spectral efficiency	$R_{\mathrm{th}}(\mathrm{bits/sec/Hz})$	8
Minimum level of harvested power	Φ_{th} (W)	80
Refractive index of air	n_1	1
Refractive index of water	n_2	1.33
Extinction coefficient for pure sea	c (m^{-1})	0.056
Extinction coefficient for clear ocean	c (m^{-1})	0.015
Extinction coefficient for coastal water	c (m^{-1})	0.305
Extinction coefficient for harbor water	c (m^{-1})	2.17
Latitude of the location of interest	ϑ	41.8
Longitude of the location of interest	θ	37.6
Day of the year	Θ	180
Solar constant	Ψ ($\mathrm{W/m}^2$)	1366.1

Table 8: Specifications of the solar-powered AUV

Parameter	Variable	Value
Length of the solar-powered AUV	L (m)	1.8 [107]
Mass of the solar-powered AUV	m (kg)	75.5 [107]
Diameter of the solar-powered AUV	D_{s} (m)	0.14 [107]
Surface area of the solar panel	κ (m^2)	1 [107]
Wing area	A_{wings} (m^2)	0.127 [22]
Drag coefficient	C_{D}	0.0064
Efficiency of the propulsion system	$\eta_{\mathrm{p}}(\%)$	73 [107]
Efficiency of the solar panel	$\xi(\%)$	20 [107]
Velocity of the AUV (thrust mode)	$\|v_{\mathrm{M}_3}\|$ (m/s)	2 [22]
Velocity of the AUV (gliding mode)	$\|v_{\mathrm{M}_2}\|, \|v_{\mathrm{M}_4}\|$ (m/s)	0.4 [22]
Initial battery storage size	Q_{b} (MJ)	36
Water density	$\rho(\mathrm{Kg/m}^3)$	997 [19]



(a)



(b)

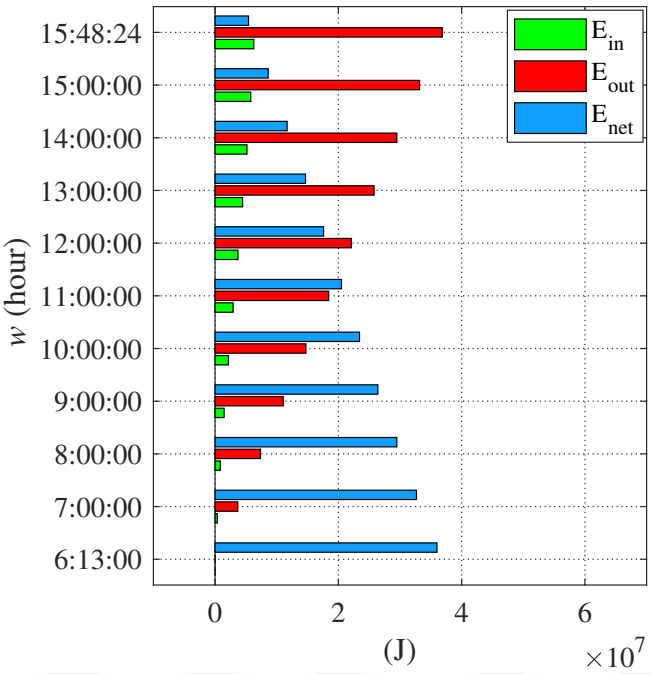
Figure 22: (a) Optimal 3D EH-aware trajectory, (b) Benchmarking 2D trajectory.

$S_{13,12}, S_{14,16}, S_{15,11}, S_{16,14}, S_{17,13}, S_{18,15}$).

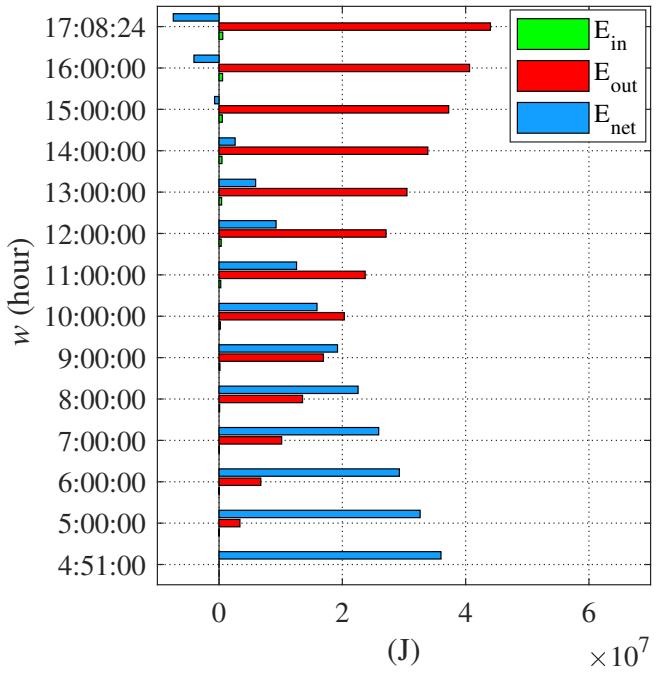
For the given order, we then solve Eq. (3.20) on page 55 to yield the optimal trajectory illustrated in Fig. 22(a) on the previous page The optimal operation depth at each sensor node is the minimum required depth for the AUV to satisfy the constraint C1 and is obtained in accordance with each sensor's height using Eq. (3.23) on page 56.

As a benchmark (see Fig. 22(b) on the previous page), we consider a two-dimensional 2D trajectory where the AUV works at a fixed operation depth and follows a straight path between sensor nodes. In this case, the sequence order of sensor nodes is determined by the nearest neighbor algorithm and is given by $\mathbf{S} = \big(S_{1,1}, S_{2,4}, S_{3,2}, S_{4,6}, S_{5,5}, S_{6,3}, S_{7,17}, S_{8,10}$, $S_{9,18}, S_{10,16}, S_{11,11}, S_{12,14}, S_{13,9}, S_{14,13}, S_{15,15}, S_{16,12}, S_{17,8}, S_{18,7}\big)$. The selection of fixed operation depth is made such that it guarantees a reliable transmission between the AUV and each of the nodes. For this example, the fixed operation depth is found as $z_{\mathrm{A}} = 9.5\,\mathrm{m}$ (In the USN scenario under consideration, the depth that guarantees the reliable transmission between the AUV and all the nodes (to satisfy the spectral efficiency of $R_k[n] \geq R_{\mathrm{th}}$) is $z_{\mathrm{A}} \geq 9.4\,\mathrm{m}$ which is dictated by the node with the highest depth amongst all. Therefore, in the benchmarking case with a fixed depth trajectory, we assume that the AUV swims at the depth of $z_{\mathrm{A}} = 9.5\,\mathrm{m}$). For the given bandwidth of $B = 100\,\mathrm{MHz}$ and required spectral efficiency of $R_{\mathrm{th}} = 8\,\mathrm{bits/sec/Hz}$, it can be calculated from Eq. (3.16) on page 54 that the required data of $\Im_{\mathrm{sc}} = 256\,\mathrm{Mbits}$ can be gathered in $t_{\mathrm{M}_1,k} = 0.32$ seconds. Moreover, to satisfy $R_{\mathrm{th}} = 8\,\mathrm{bits/sec/Hz}$, the distance between the AUV and the sensor node needs to be equal to d_{th} based on . In the 2D benchmarking case, since the operation depth is fixed, the distance between the AUV and each node to satisfy $R_{\mathrm{th}} = 8\,\mathrm{bits/sec/Hz}$ is less than d_{th} in most cases. The communication duration takes values in the range of $t_{\mathrm{M}_1,k} = 0.19 - 0.3$ seconds. The difference between the two cases is obviously negligible given the mission time in terms of hours.

In Fig. 23(a) on the next page, we illustrate the consumed and harvested energy levels as well as the net energy over the mission duration for the EH-aware 3D optimum trajectory.



(a)



(b)

Figure 23: Consumed, harvested and net energy levels over the mission duration (a) optimal 3D trajectory, (b) benchmark 2D trajectory.

Table 9: Sensor locations

Sensor S_i	$\mathbf{p}_{S_i}$ (Km, Km, m)	**Sensor** S_i	$\mathbf{p}_{S_i}$ (Km, Km, m)
S_1	$(9,1,25)$	S_{10}	$(11,16,23)$
S_2	$(4,5,19.5)$	S_{11}	$(12,9,19)$
S_3	$(3,17,21)$	S_{12}	$(16,8,19.4)$
S_4	$(6,3,22)$	S_{13}	$(6,10,20)$
S_5	$(1,15,19.3)$	S_{14}	$(10,11,20)$
S_6	$(2,9,20)$	S_{15}	$(10,5,24)$
S_7	$(19,12,25)$	S_{16}	$(14,11,19.8)$
S_8	$(17,16,20.1)$	S_{17}	$(7,19,22)$
S_9	$(8,13,27)$	S_{18}	$(13,14,19.4)$

We assume that the initial battery energy is $Q_{\text{b}} = 36$MJ [53], so the net energy level at the start of the mission is $E_{\text{net}} = 36\,\text{MJ}$. Under the assumptions of $\|v_{\text{M}_3}\| = 2\text{m/s}$, $\|v_{\text{M}_2}\| = \|v_{\text{M}_4}\| = 0.4\,\text{m/s}$, and $\|v_{\text{M}_1}\| = 0\,\text{m/s}$, the required mission time is $T = 9.59$ hours, and the corresponding mission length is $d_{\text{tot}} = 73.44\,\text{Km}$. Assuming that the mission is initiated at the best start time of $t_{\text{start}} = 6:13:00$, the total harvested energy during the mission is $E_{\text{in}} = 6.28\,\text{MJ}$ while the total consumed energy is $E_{\text{out}} = 36.8\,\text{MJ}$. Therefore, at the end of the mission, the remaining net energy is $E_{net} = Q_b + E_{in} - E_{out} = 5.43$MJ. This indicates that the AUV does not run out of battery and, by the time the mission is completed, it has an additional amount of 5.43MJ remaining in its battery.

In Fig. 23(b) on the preceding page, we illustrate the consumed, harvested, and net energy levels for the benchmarking 2D trajectory. In this case, it takes $T = 12.29$ hours to complete the mission, and the corresponding mission length is $d_{\text{tot}} = 89.28\,\text{Km}$. The total consumed energy is $E_{\text{out}} = 44$MJ. Assuming that the mission starts at $t_{\text{start}} = 4:51:00$ (i.e., the best start time for this case), the total harvested energy is $E_{\text{in}} = 0.6\,\text{MJ}$. It can be readily seen that the AUV runs out of battery before $w = 15:00:00$. The net energy at the end of the mission is $E_{\text{net}} = -7.42\,\text{MJ}$, which indicates that the AUV would need this additional amount to complete the mission.

Fig. 24 on the next page illustrates the effect of thrust mode's velocity on the AUV performance. It is observed that energy consumption increases proportional to the cube

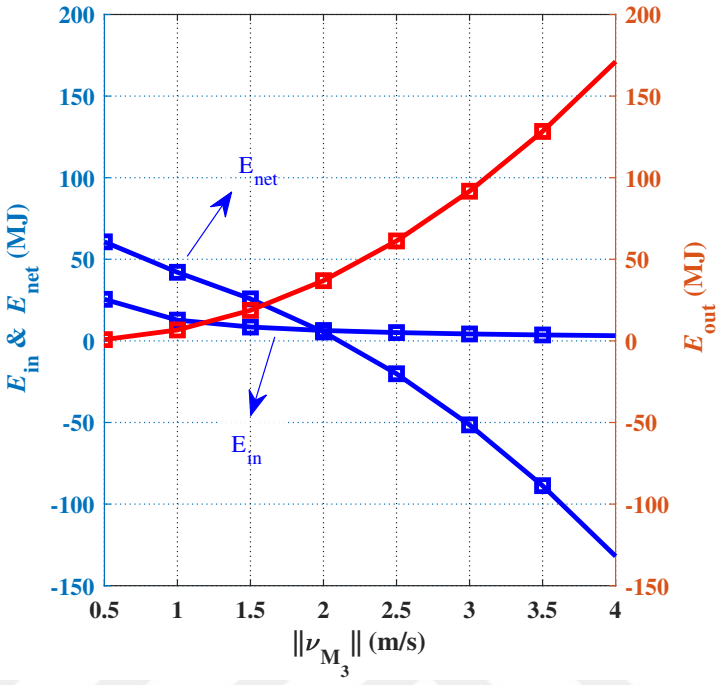


Figure 24: Effect of velocity on the harvested energy, consumed energy, and net energy.

of velocity based on Eq. (3.11) on page 53. It has also an indirect effect on the energy harvesting. According to Eq. (2.9) on page 13, with the increase in the velocity, the time taken to go from one sensor to the next decreases, and therefore less power can be harvested from the sun. Therefore, the net energy effectively decreases. For instance, assume a velocity of $\|v_{M_3}[n]\| = 3\,\mathrm{m/s}$. The required mission time is $T = 6.4$ hours. The total harvested energy during the mission is $E_{\text{in}} = 4.2\,\mathrm{MJ}$ while the total consumed energy is $E_{\text{out}} = 91.7\,\mathrm{MJ}$. Therefore, at the end of the mission, there is an energy shortage in the amount of $E_{net} = Q_b + E_{in} - E_{out} = -51.46\mathrm{MJ}$. On the other hand, if we decrease the velocity to $\|v_{M_3}[n]\| = 1\,\mathrm{m/s}$, the required mission time is $T = 19.4$ hours. The total harvested energy during the mission is $E_{\text{in}} = 12.74\,\mathrm{MJ}$ while the total consumed energy is $E_{\text{out}} = 6.7\,\mathrm{MJ}$. Therefore, at the end of the mission, the remaining net energy is $E_{net} = Q_b + E_{in} - E_{out} = 42\mathrm{MJ}$. However, the operation time ($T = 19.4$ hours) significantly increases from 6.4 hours to 19.4 hours. This indicates the importance of properly selecting the velocity value to find the best trade-off between the net energy and operation

time.

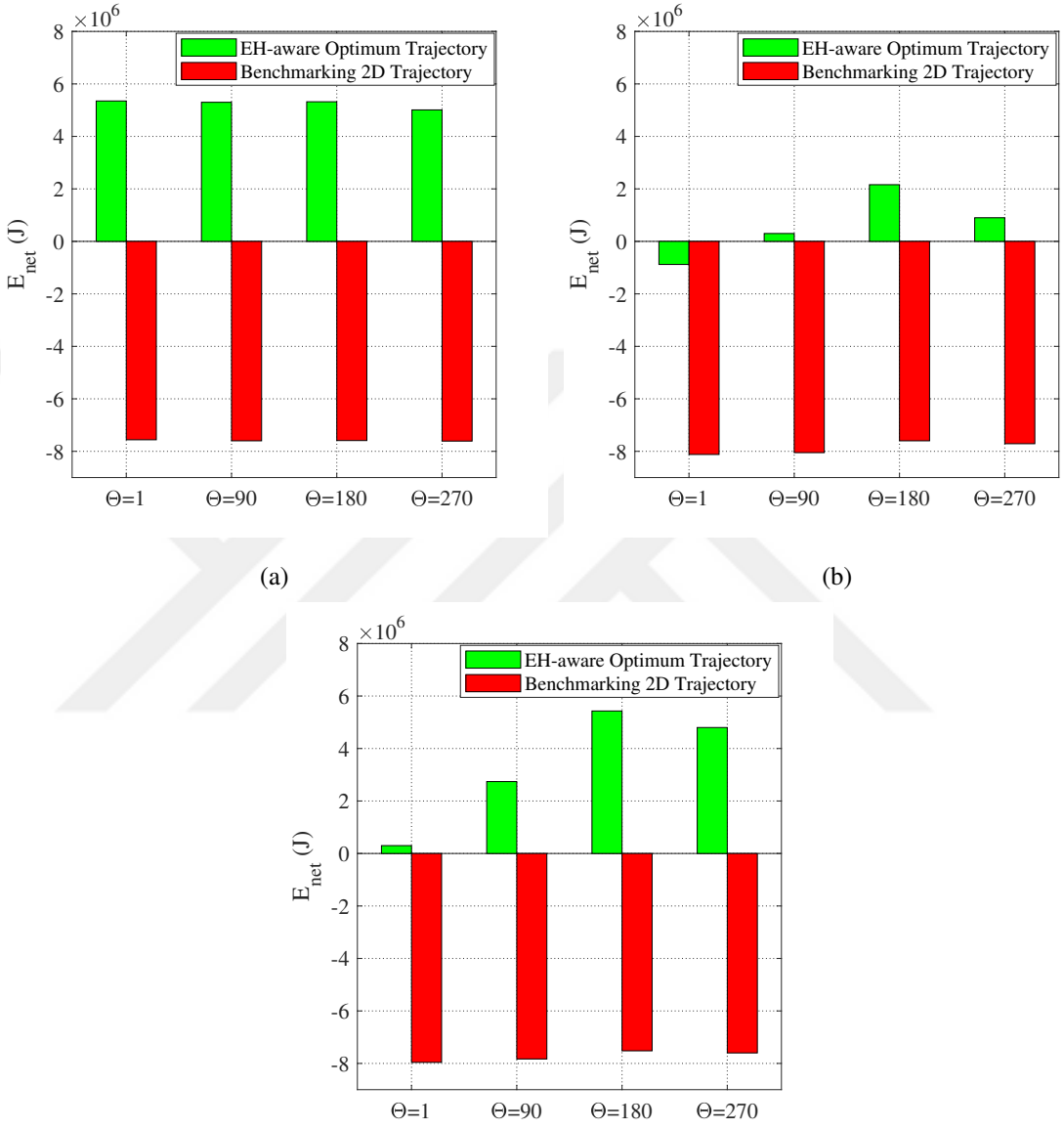


Figure 25: Comparison of net energy levels for different operation days under consideration in (a) Tropical, (b) Subarctic, and (c) Mid-latitude climate types.

In Fig. 25, we compare the net energy levels for the three climate types under consideration and the representative operation days. In the case of benchmarking 2D scheme, the harvested energy remains at very low values in all the climate types and, regardless of

the operation day, this trajectory yields negative values for net energy indicating that the battery runs out before the mission time for the given size of the area and the number of sensor nodes to be visited. In general, optimized trajectory yields much better performance in comparison to the 2D benchmarking scheme. The net energy level changes with the operation day since it is highly dependent on a harvested energy level. For all operation days under consideration except the $\Theta = 1^{\text{st}}$ day of the year for the subarctic location, net energy levels always take positive values indicating that the mission is successfully completed as a result of the adopted optimal EH-aware trajectory.

CHAPTER IV

ENERGY MANAGEMENT SOLUTIONS IN AIRBORNE NETWORKS

4.1 Introduction

In the fast-evolving world of communication technologies, rotary wing UAVs and fixed-wing UAVs have emerged as groundbreaking solutions for various applications. These airborne vehicles offer unparalleled opportunities in surveillance, monitoring, data collection, wireless communications, and disaster management. Their inherent capabilities, including rapid deployment, high mobility, and adaptive altitude, make them promising candidates for future airborne backhaul communication infrastructures. However, one major challenge that hinders their widespread adoption and efficiency is their reliance on batteries with limited capacities [108].

The limited operation time of UAVs constrained by their battery capacity, presents significant obstacles to realizing their full potential in extended missions and autonomous operations. Frequent battery replacements and the need to return to home bases for recharging disrupt their tasks, reducing their efficiency and cost-effectiveness. To address this critical issue and unlock the transformative potential of UAVs, we turn our attention to energy sustainability and innovative approaches to improve their energy efficiency [109].

4.1.1 Rotary-Wing UAVs

Rotary wing UAVs have gained significant prominence in various industries due to their unique capabilities and versatility. Unlike fixed-wing UAVs, which rely on a forward propulsion system, rotary-wing UAVs utilize rotating blades to generate lift and achieve controlled flight. This design allows them to take off and land vertically, hover in place,

and maneuver in confined spaces, making them well-suited for a wide range of applications.

Rotary-wing UAVs find extensive use in providing temporary connectivity solutions, particularly during large events or in scenarios where traditional infrastructure may be inadequate or unavailable. In such cases, these UAVs are deployed from the telecommunications operator's headquarters, which may be located some distance away from the event site or the area requiring connectivity.

To establish the necessary connectivity, rotary-wing UAVs follow a well-defined operational procedure. Initially, the UAV ascends vertically to reach the desired altitude, ensuring it is above potential obstacles and interference sources. Once the desired altitude is achieved, the UAV transitions into a state of straight and level flight to navigate efficiently to the designated area where connectivity is needed. This transition enables the UAV to cover the required distance effectively [110].

Upon reaching its destination, the rotary-wing UAV assumes a stationary position and hovers in place, remaining airborne for a specified period to fulfill its mission. During this time, it serves as a valuable communication relay platform, facilitating data transmission, wireless connectivity, and network support to users on the ground.

The unique capabilities of rotary-wing UAVs, such as their ability to hover and provide connectivity in remote or challenging environments, make them indispensable assets in wireless communication systems. Their flexibility and adaptability make them valuable tools in scenarios ranging from disaster recovery and public safety operations to enhancing network coverage during large gatherings or events. In the following sections, we will delve deeper into the diverse applications and use cases where rotary-wing UAVs play a pivotal role in wireless communication systems.

4.1.2 Fixed wing UAVs and HAPs

Fixed wing UAVs and HAPs (Here, we use the term high altitude platform station (HAPs) to describe UAVs that operate at the stratospheric altitude (17-22 km)) represent another

category of aerial platforms used in wireless communication systems. They have unique features that make them suitable for specific applications in wireless communication systems specially in Cellular backhauling for rural areas [42]. These platforms rely on aerodynamic principles and buoyancy to achieve their missions, offering extended endurance, broader coverage, and stable operation at high altitudes. This section will delve into the characteristics, capabilities, and use cases of fixed-wing UAVs and HAPs, highlighting their significance in enhancing wireless connectivity and communication systems.

4.2 Rotary-Wing UAV Based Communication Systems

UAV-based wireless links can be used as alternative or complementary backhaul and access solutions to terrestrial infrastructure taking advantage of UAV's inherent features such as rapid deployment, high mobility, and adaptive altitude [109].

UAVs can be equipped with a radio base station and deployed as an aerial base station providing wireless access to end users [30–33]. For example, in [30], optimum 3D deployment of multiple UAV base stations is investigated with the goal of improving the coverage rate while satisfying the QoS requirements of each user. In [31], an aerial base station placement algorithm is proposed to reduce the number of required UAVs to serve a desired coverage area. In [32], optimum UAV trajectory design is investigated to minimize its mission completion time while ensuring that each ground node receives the required information within a given time. In [33], 3D trajectory optimization of multiple UAVs is pursued with the goal of optimizing the coverage while maximizing the sum of QoSs requirements of ground users.

In addition to the line of research on UAV-based wireless access discussed above, it is also possible to utilize UAVs as backhaul links to the ground base station. Rotary-wing UAVs have the capability of hovering and might be particularly attractive for small cell backhauling. They can be positioned as a complementary solution to the terrestrial backhaul links in dense areas with high-peak traffic demands. For UAV-based backhauling,

the operation frequency can be selected from RF band [34–36] or optical band (in particular, infrared) [26, 37–39]. In RF-based solutions, either out-of-band or in-band frequencies can be used for backhauling connectivity [40, 111]. While the use of out-of-band frequency avoids interference, it becomes a more costly approach. On the other hand, in in-band backhauling, robust interference management becomes critical.

FSO has emerged as an alternative backhauling technology. It uses laser transmitters operating at infrared wavelengths and provides a LOS link with a capacity comparable to fiber optics and much higher than those that can be supported by RF counterparts. In addition, since they operate in optical spectrum, they are immune to interference. Furthermore, unlike RF backhaul links which require either area or link license for operation, no licensing fee is required. In [37], with the goal of minimizing the capital cost of the FSO-based aerial backhaul network, the problem of minimizing the number of UAVs is investigated. In [38], to improve the energy efficiency of the UAV-based backhaul networks, a hybrid RF-FSO system is proposed with simultaneous harvesting capability. In [39], to improve the energy efficiency of the UAV-based backhaul network, a modulating retro-reflector based FSO system is proposed which leads to an increase in the maneuverability and flight time of UAVs. In [40], solar-powered rotary-wing UAVs are considered and the problem of UAV placement in a dense urban environment is investigated to ensure backhaul connectivity. To maximize the harvested energy, the UAVs are placed in sunny spots between the buildings.

In an urban area with many buildings, the operation altitude of a solar-powered UAV plays an important role in the energy efficiency of the aerial backhaul link. It has a significant effect on the endurance of the solar-powered UAV (which can be quantified in terms of net energy defined as the difference between energy consumption and harvesting) as well as the probability of establishing the LOS link. Some earlier works on RF-based UAV backhauling discussed the optimal selection of altitude. For example, in [35], a mathematical model is presented to determine an optimal altitude with the goal of providing maximum

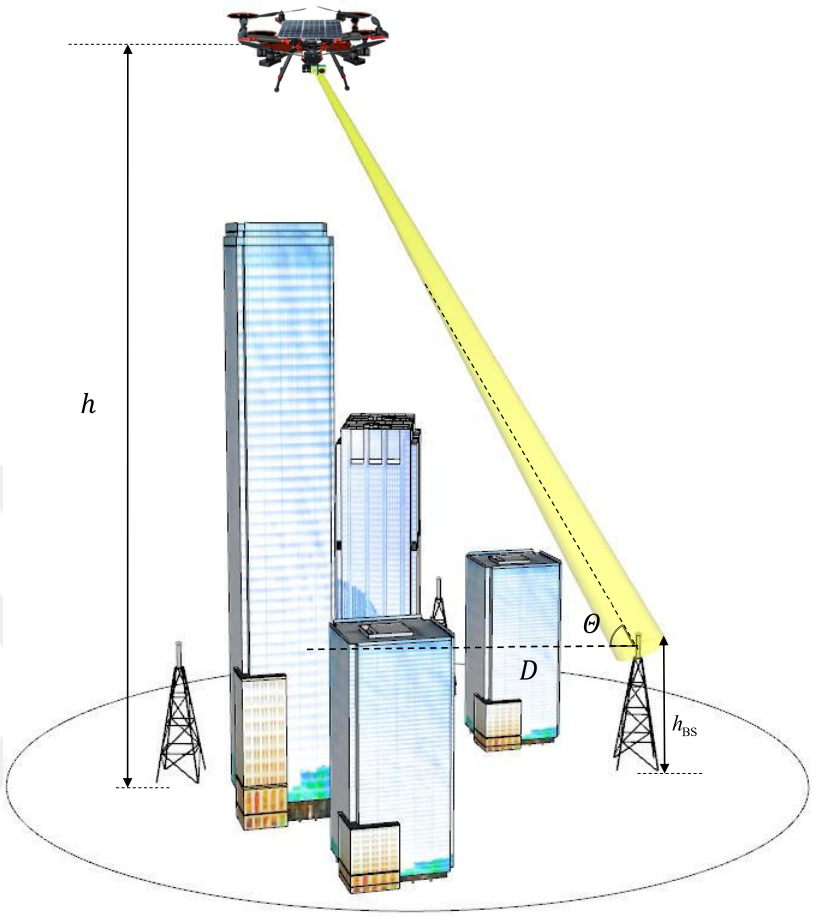


Figure 26: LOS link between the solar-powered rotary-wing UAV and the ground base station in an urban area.

radio coverage on the ground assuming an in-band frequency of 2 GHz. In [41], optimal altitude is selected to maximize the coverage area for a targeted outage probability.

We consider a solar-powered rotary-wing UAV equipped with an FSO terminal that provides backhaul link to a ground base station in an urban area. We first quantify the energy consumption and energy harvesting of a rotary-wing solar-powered UAV. Then, we formulate an optimization problem to determine the optimal operation altitude with the goal of maximizing the net energy of UAV while satisfying the LOS requirements critical for the FSO link.

4.2.1 Energy Consumption Model

The energy consumption of rotary-wing UAVs varies across different phases of operation, necessitating a comprehensive model to understand and optimize their power usage. In our analysis, we present a detailed energy consumption model for rotary-wing UAVs, considering three distinct modes of operation:

- **Ascending Flight**: This mode encompasses the UAV's ascent to reach the desired altitude. During this phase, energy consumption is influenced by factors such as climb rate, payload weight, and aerodynamic forces. Understanding the power requirements in ascending flight is crucial for mission planning and resource allocation.

- **Straight and Level Flight**: Once the desired altitude is achieved, rotary-wing UAVs transition into straight and level flight. This phase is characterized by sustained, forward motion at a constant altitude. Energy consumption in this mode is primarily determined by airspeed, altitude, and environmental conditions. Optimizing energy usage during straight and level flight is vital for extending mission duration and coverage.

- **Hovering**: Rotary-wing UAVs have the unique capability to hover in place, making them versatile for tasks that require stationary observation or precise positioning. Hovering demands a different energy profile compared to forward flight, as the UAV must counteract gravity and maintain its position. Accurate modeling of energy consumption during hovering is essential for applications such as surveillance, monitoring, and data collection.

The closed-form expression of a rotary wing UAV power consumption in vertical ascending flight consists of three components, namely blade profile to overcome the profile drag of the blades, induced power to overcome the induced drag of the blades, and altitude gain to overcome the gravity in ascending. Mathematically speaking, it is given by [110]

$$P_{\text{rotary,a}} = \underbrace{P_0}_{\text{blade profile}} + \underbrace{P_{\text{i}}}_{\text{induced}} + \underbrace{\frac{1}{2}T_{\text{a}}v_{\text{a}} + \frac{T_{\text{a}}}{2}\sqrt{{v_{\text{a}}}^2 + \frac{2T_{\text{a}}}{\rho_{\text{a}}A}}}_{\text{altitude gain}} \tag{4.1}$$

where v_{a} is the velocity in ascending flight, A is the rotor disc area, P_0 is a constant representing the blade profile power in hovering status and is given by

$$P_0 = \frac{\Im}{8}\rho_{\text{a}} s A \Omega^3 {R_{\text{d}}}^3, \tag{4.2}$$

where $\Im$ is the profile drag coefficient, Ω is the blade angular velocity, R_{d} is the rotor radius, s is the rotor solidity. In Eq. (4.1), P_i represents the induced power in hovering status and is given by [110]

$$P_i = (1+k)\frac{W^{3/2}}{\sqrt{2\rho_{\text{a}}A}}, \tag{4.3}$$

where k is incremental correlation factor to induced power, $W = mg$, is the weight of the UAV. In Eq. (4.1), T_{a} is the rotor thrust and is given by

$$T_{\text{a}} = W + \frac{1}{2}S_{\text{FP}\perp}\rho_{\text{a}}{v_{\text{a}}}^2 \tag{4.4}$$

where $S_{\text{FP}\perp}$ is fuselage equivalent flat plate area in the vertical status. ρ_{a} is the average air density required is the one that accounts for the entire range from the ground to the intended UAV altitude. It can be expressed as follows

$$\rho_{\text{a}} = \frac{\int_0^h \frac{p_0\mu}{\varpi t_0}\left(1 - \frac{\sigma h}{t_0}\right)^{\frac{g\mu}{\varpi\sigma}-1}}{h} \tag{4.5}$$

where p_0 is sea level standard atmospheric pressure, μ is molar mass of dry air, ϖ is ideal gas constant, t_0 is sea level standard temperature, and σ is temperature lapse rate.

If the time that it takes (in hours) to reach the desired altitude in the vertical direction is $t_{\text{a}} = h/3600v_{\text{a}}$, the energy consumption in ascending flight in (in Watt-hour) is calculated as

$$E_{\text{rotary,a}} = P_{\text{rotary,a}}t_{\text{a}} \tag{4.6}$$

The propulsion power consumption of the rotary wing UAV in a straight and level flight consists of three components including blade profile to overcome the profile drag of the blades, induced power to overcome the induced drag of the blades, and parasite power to overcome the fuselage drag [110]. Mathematical speaking, it is given by

$$P_{\text{rotary,f}} = \underbrace{P_0\left(1+\frac{3{v_{\text{f}}}^2}{{v_{\text{tip}}}^2}\right)}_{\text{blade profile}} + \underbrace{P_{\text{i}}\left(\sqrt{1+\frac{{v_{\text{f}}}^4}{4{v_0}^4}}-\frac{{v_{\text{f}}}^2}{2{v_0}^2}\right)^{1/2}}_{\text{induced}} + \underbrace{\frac{1}{2}S_{\text{FP}}\rho{v_{\text{f}}}^3}_{\text{parasite}} \tag{4.7}$$

where v_{tip} is the tip speed of the rotor blade, v_0 is the mean rotor induced velocity in hover, v_{f}, S_{FP} is the fuselage equivalent flat plate area in horizontal status, and ρ denotes air density and is given by [112]

$$\rho = \frac{p_0\mu}{\varpi t_0}\left(1-\frac{\sigma h}{t_0}\right)^{\frac{g\mu}{\varpi\sigma}-1}, \tag{4.8}$$

If the time that it takes to reach a specific location is $t_{\text{r,f}} = d_{\text{f}}/3600v_{\text{f}}$ hours, The energy consumption in straight level flight is therefore calculated as

$$E_{\text{rotary,f}} = P_{\text{rotary,f}}t_{\text{r,f}} \tag{4.9}$$

The energy consumption of a rotary-wing UAV in hovering status (in Watt-hour) can be calculated by

$$E_{\text{out}} = P_{\text{hovering}}T, \tag{4.10}$$

where P_{hovering} is the required power for the UAV to maintain aloft. It is given by [110]

$$P_{\text{hovering}} = P_0 + P_{\text{i}} \tag{4.11}$$

In Eq. (4.11), P_0 is a constant representing the blade profile power in hovering status and is earlier defined in Eq. (4.2) on the preceding page, and P_i represents the induced power in hovering status and is earlier defined in Eq. (4.3) on the previous page.

4.2.2 Communication Model

We consider an urban area in cellular networks where a solar-powered rotary-wing UAV provides FSO-based backhaul connectivity to a ground base station as shown in Fig. 26 on page 72. Due to the small divergence angle of a laser transmitter, this requires the establishment of a LOS link between the UAV and the base station. Here, h_{BS} denotes the height of the receiving unit (located on the top of the base station) from the ground, and h is the operation altitude of the UAV. Θ and D denote, respectively, the elevation angle and horizontal distance between the UAV and the base station.

In the urban area scenario under consideration, the tall buildings might obstruct the FSO links which require LOS availability. The Probability Density Function (PDF) of the LOS link is given by [35]

$$\begin{aligned} &P_{\mathrm{LOS}}(\alpha,\beta,D,h,h_{\mathrm{BS}}) \\ &= \prod_{k=0}^{\left\lfloor D\sqrt{\alpha\beta}\right\rfloor-1}\left[1-\exp\left(-\frac{1}{2\upsilon^2}\left[h-\frac{\left(k+\frac{1}{2}\right)(h-h_{\mathrm{BS}})}{\left\lfloor D\sqrt{\alpha\beta}\right\rfloor}\right]^2\right)\right], \end{aligned} \tag{4.12}$$

where $\lfloor\cdot\rfloor$ is the floor function that maps the inner argument to the maximum integer that is smaller than or equal to it, i.e., $\lfloor x\rfloor = \max(m\in\mathbb{R}\,|m\leqslant x)$, α is a dimensionless unit representing the ratio of built-up area to the total area, and β is the average number of buildings per km^2. In Eq. (4.4) on page 74, υ is a scaling parameter that describes the buildings' height distribution. In [113], the PDF of building height distribution (H) is given by

$$f_H(H) = \left(\frac{H}{\upsilon^2}\right)\exp\left(-\frac{H^2}{2\upsilon^2}\right). \tag{4.13}$$

The mean of buildings' heights is therefore $\mu_{\mathrm{H}} = E[H]$, where $E[\cdot]$ denotes the expectation operator. The scaling parameter can then be defined in terms of the mean as $\upsilon = \mu_{\mathrm{H}}\sqrt{2/\pi}$.

4.2.3 Optimization Problem Formulation

In this section, we formulate an optimization problem to determine the UAV operation altitude. We aim to maximize the net energy defined as

$$E_{\text{net}} = E_{\text{in}} - E_{\text{out}}. \tag{4.14}$$

where E_{in} is the overal input energy of the UAV. We assume that the UAV becomes airborne $T/2$ hours before solar noon (Solar noon is the moment when the Sun reaches its highest position in the sky which is typically observed at 12:00 pm), i.e., $t_{\text{start}} = 12 - T/2$. The overall input energy of the UAV can be then written as

$$E_{\text{in}} = E_{\text{h}} + E_{\text{b}}, \tag{4.15}$$

where E_{h} is the harvested energy during the mission time, and E_{b} is the initial battery capacity.

The optimization is carried out under the constraints of achieving an acceptable probability of LOS while respecting the aerodynamic specifications of the UAV which imposes a maximum operation altitude for the UAV. Mathematically speaking, we have

$$\begin{aligned} h_{\text{opt}} &= \arg\max_{h} \; E_{\text{net}} \\ \text{s.t.} \;\; & \text{C1} : P_{\text{LOS}} > P_{\text{LOS,th}} \\ & \text{C2} : h \leqslant h_{\max} \end{aligned} \tag{4.16}$$

The constraint C1 imposes a minimum required altitude for the UAV to satisfy a targeted acceptable probability of LOS denoted by $P_{\text{LOS,th}}$. The minimum operation altitude (i.e., $h_{\min}$) to achieve this is obtained by numerically solving Eq. (4.4) on page 74 for h. Constraint C2 imposes a maximum operation altitude for the rotary-wing UAV (i.e., $h \leqslant h_{\max}$) dictated by the UAV aerodynamic design.

It can be readily checked that the second derivative of E_{net} with respect to the altitude gives negative values for practical values of the altitude. Therefore, the function is concave,

and it always has one single optimum solution which we aim to obtain in the following. Replacing Eq. (4.10) on page 75 and Eq. (4.15) on the preceding page in Eq. (4.14) on the previous page, we obtain E_{net} as

$$\begin{aligned} E_{\text{net}} =& E_{\text{b}} + \frac{E_{\text{h}}}{\psi}\left(0.8978 - 0.2804\exp\left(-\frac{h}{3500}\right)\right) \\ & - \frac{\left(2\varpi t_0 W^3\right)^{\frac{1}{2}} T}{\left(A\rho_0\mu\right)^{\frac{1}{2}}\eta_{\text{rotor}}} t_0^{\,0.5\left(\frac{g\mu}{\varpi\sigma}-1\right)}\left(t_0-\sigma h\right)^{-0.5\left(\frac{g\mu}{\varpi\sigma}-1\right)}. \end{aligned} \tag{4.17}$$

where η_{rotor} is the rotor's efficiency. We take the derivative of Eq. (4.17) with respect to the altitude and set the resulting expression to zero. Under the assumption of $\sigma h << t_0$ (which can be justified for low altitude UAVs (in numerical results, the maximum altitude is considered to be 3 km), the optimum altitude can be obtained as

$$h_{\text{opt}} \approx -3500\ln\left(\frac{6241\,\psi\sigma\left(\frac{g\mu}{\varpi\sigma}-1\right)T\sqrt{\left(\frac{2\varpi t_0 W^3}{A\rho_0\mu}\right)}}{E_{\text{h}} t_0 \eta_{\text{rotor}}}\right). \tag{4.18}$$

The above solution was obtained without taking into account the constraints of C1 and C2. Recall that these constraints basically dictate the minimum and maximum values allowed for the operation altitude. If h_{opt} calculated from Eq. (4.10) on page 75 is within the allowable range of $h_{\min} \le h_{\text{opt}} \le h_{\max}$, h_{opt} is indeed the optimum altitude. If h_{opt} is lower than the minimum altitude imposed by constraint C1, $h_{\min}$ becomes the optimum solution, i.e., $h_{\text{opt}} = h_{\min}$. On the other hand, if h_{opt} is higher than the maximum altitude imposed by constraint C2, $h_{\max}$ becomes the optimum solution, i.e., $h_{\text{opt}} = h_{\max}$.

4.2.4 Results and Discussions

In this section, we present numerical results to demonstrate the benefits of optimization of the UAV operation altitude as well as discuss the effect of various system parameters on this optimization. The amount of harvested energy by the solar-powered UAV is obviously dependent on the time of the day and the geographical location. To assess the energy harvested by the UAV, we consider Ankara, Turkey with latitude of $L = 39.86$, and $d = 150^{\text{th}}$

Table 10: Specifications of the solar-powered rotary-wing UAV

Parameter	Variable	Value
Total Mass of the UAV	$m\,(\mathrm{kg})$	8
Solar Area	$\mathrm{A_s}\ (\mathrm{m^2})$	4
Rotor Disk Area	$A\ (\mathrm{m^2})$	0.503
Acceleration	$g\ (\mathrm{m/s^2})$	9.8
Solar Constant	$G_{\mathrm{sc}}\ (\mathrm{W/m^2})$	1366.1
Efficiency of the Solar Cell	η_{sc}	37.5 (%)
Horizontal Distance between the UAV and Base Station	$D\ (\mathrm{m})$	1000
Height of Base Station	$h_{\mathrm{BS}}\ (\mathrm{m})$	50
Maximum Altitude of the UAV	$h_{\mathrm{max}}\ (\mathrm{m})$	3000
Rotor's Efficiency	η_{rotor}	90 (%)
The initial battery capacity	$E_{\mathrm{b}}\ (\mathrm{Wh})$	500 [114]

Table 11: Air density variables

Parameter	Variable	Value
Sea Level Standard Atmospheric pressure	$p_0\ (\mathrm{J/m^3})$	101325
Molar Mass of Dry Air	$\mu\ (\mathrm{kg/mol})$	0.0289
Ideal Gas Constant	$\varpi\ (\mathrm{J/mol.K})$	8.3144
Sea Level Standard Temperature	$t_0\ (\mathrm{K})$	288.15
Temperature Lapse Rate	$\sigma\ (\mathrm{K/m})$	0.0069

day of the year. We assume a GaAs solar panel with an efficiency of $\eta_{\mathrm{sc}} = 37.5\%$ [115] and a battery capacity of $E_{\mathrm{b}} = 500\,\mathrm{Wh}$. Unless otherwise stated, the UAV specifications in Table 10 are used in our study. The air density variables for the calculation of Eq. (4.3) on page 74 are provided in Table 11.

In Fig. 27 on the next page, we present the probability of LOS with respect to different altitudes of the UAV to determine the minimum allowable altitude. We assume an urban area with the ratio of built-up area to the total area $\alpha = 0.4$, the average number of buildings per $\mathrm{km^2}$, $\beta = 1000$, and the mean building's heights $\mu_{\mathrm{H}} = 50\,\mathrm{m}$. Based on Eq. (4.12) on page 76, for the given parameters, if the targeted probability of LOS is set as $P_{\mathrm{LOS,th}} = 0.95$, the required minimum altitude is found as $h_{\mathrm{min}} = 1960$ m. For $P_{\mathrm{LOS,th}} = 0.9$ and 0.85, the minimum altitude reduces to respectively $h_{\mathrm{min}} = 1480\,\mathrm{m}$, and $h_{\mathrm{min}} = 1180\,\mathrm{m}$. It is obvious that the higher the operation altitude of the UAV, the higher the probability of establishing an unobstructed link with base stations. In the following, we use $P_{\mathrm{LOS,th}} = 0.9$ which is

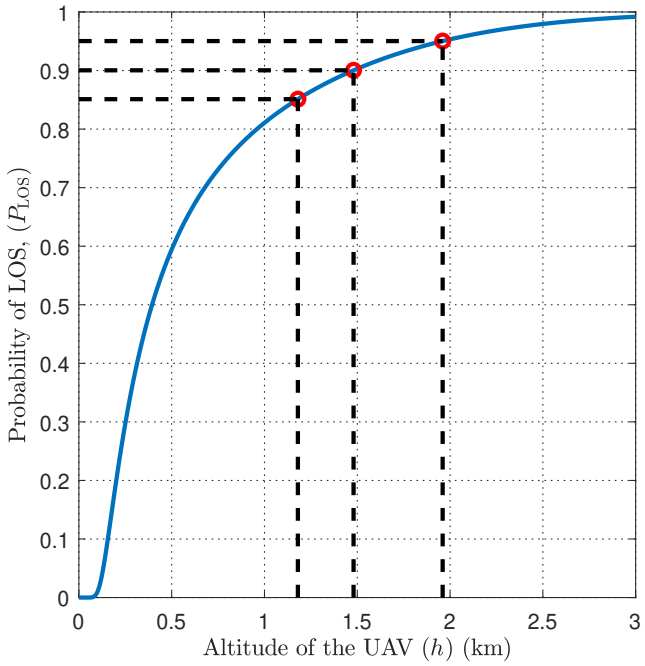


Figure 27: Probability of LOS with respect to the altitude of the UAV

reasonably high for most practical cases.

In Fig. 28 on the next page, we present the net energy with respect to altitude for various UAV weights based on Eq. (4.17) on page 78 assuming an airborne time of $T = 1$ hour. As discussed above, the minimum altitude is dictated by the LOS requirements and given by $h_{\min} = 1480\,\mathrm{m}$ for the scenario under consideration. The maximum allowable operation altitude is related to the aerodynamic specifications of the UAV. It is dependent on its weight, type of motors, propulsion configurations, and type of battery. For typical rotary-wing UAVs, the maximum altitude is around $h_{\max} = 3000\,\mathrm{m}$ [116]. Therefore, we need to stay within the range of 1480 m up to 3000 m, (shown in dashed vertical lines in Fig. 28 on the next page). In Fig. 28 on the following page, we consider a wider range of altitudes between $h = 0$ m and $h = 10000$ m to demonstrate that the net energy is indeed a concave function. It is observed that there is always one point (shown in red) that maximizes the net energy. From Eq. (4.18) on page 78, the optimum altitudes are respectively obtained as $h = 2612\mathrm{m}$, $h = 1500\mathrm{m}$, and $h = 992\mathrm{m}$, for the UAV weights of

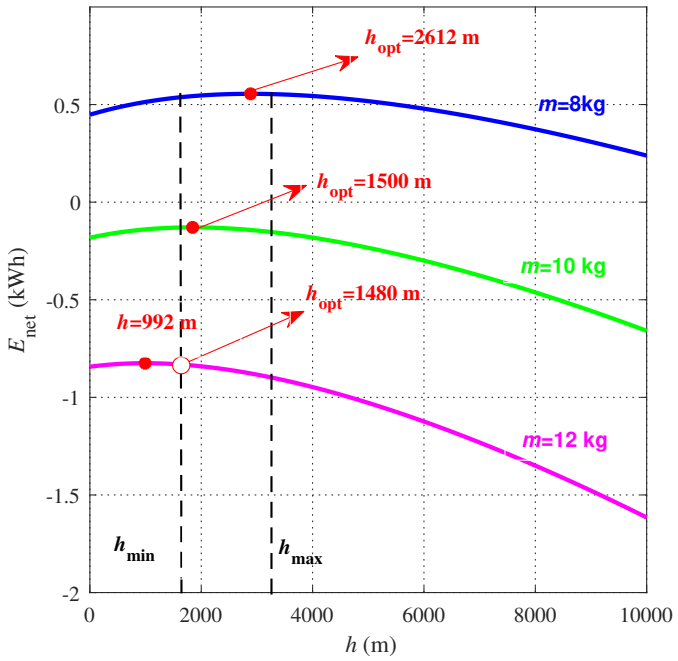


Figure 28: Net energy with respect to altitude for rotary-wing UAVs with different weights.

$m = 8\,\text{kg}$, $m = 10\,\text{kg}$, and $m = 12\,\text{kg}$. It can be readily checked that all these values are higher than the minimum allowable altitude and lower than the maximum altitude of 3000 m. However, for $m = 12\,\text{kg}$, the optimal value determined from Eq. (4.18) on page 78 is $h = 992\,\text{m}$ which is lower than the minimum altitude. Therefore, the minimum altitude imposed by LOS constraints, $h = 1480\,\text{m}$ should be selected as the operation altitude.

In Fig. 29 on the next page, we present the optimal altitude with respect to the UAV's weight. We consider a solar panel with a surface area of $A_s = 4\,\text{m}^2$ and assume different solar efficiencies of $\eta_{sc} = 37.5\%$, $\eta_{sc} = 25\%$, and $\eta_{sc} = 15\%$. It can be observed that the optimal altitude decreases as the solar efficiency decreases for a fixed weight. For example, consider a solar-powered UAV with a weight of $m = 8\,\text{kg}$. While its optimum altitude is $h = 2612\,\text{m}$ for $\eta_{sc} = 37.5\%$, it decreases to $h = 1480\,\text{m}$ for $\eta_{sc} = 25\%$, and $\eta_{sc} = 15\%$. The optimal value from Eq. (4.18) on page 78 for $\eta_{sc} = 25\%$, and $\eta_{sc} = 15\%$ is actually lower and given by $h = 1193\,\text{m}$, and $h = 13\,\text{m}$, respectively. Here, the minimum altitude

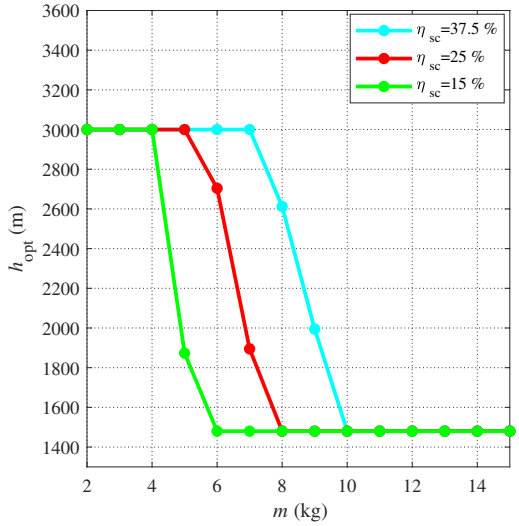


Figure 29: Optimum altitude versus UAV weight for different values of solar panel efficiency.

dictated by the LOS requirement is used. Similarly, for $\eta_{sc} = 25\%$, the optimum altitude for the UAVs for weights larger than $m = 8\,\text{kg}$ is determined by this minimum altitude and hence given by $h = 1480\,\text{m}$. For $\eta_{sc} = 15\%$, the minimum altitude becomes the optimal altitude for UAVs for weights higher than $m = 6\,\text{kg}$.

In Fig. 30 on the next page, we present the optimal altitude with respect to the solar panel area. We consider an UAV with a weight of $m = 8\,\text{kg}$ and assume different solar efficiencies of $\eta_{sc} = 37.5\%$, $\eta_{sc} = 25\%$, and $\eta_{sc} = 15\%$. It is observed that the optimum altitude increases as the solar surface area increases for a fixed value of solar efficiency (GaAs solar panels weigh approximately 200g per meter square [115]. The extra weight will affect the overall weight of the UAV and consequently result in an increase in energy consumption. This issue was taken into account in our calculations). For example, assume that UAV is equipped with a solar panel having a solar efficiency of $\eta_{sc} = 25\%$, The optimum altitude for the solar panel size of $A_s = 4\,\text{m}^2$ is $h = 1480\,\text{m}$. This increases to $h = 2612\,\text{m}$ for $A_s = 6\,\text{m}^2$.

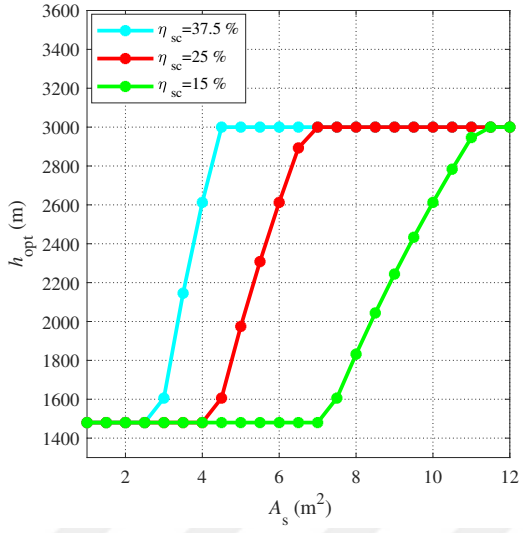


Figure 30: Optimum altitude versus solar panel size for different values of solar panel efficiency.

4.2.5 Comprehensive Energy Assessment of Solar Powered UAVs

In the following, we show how the the total power consumption of a rotary wing UAV is distributed in different modes of operation including ascending flight, straight and level flight, and hovering.

In Fig. 31(a) on page 85, we show how the total power consumption for ascending flight of a rotary wing UAV is distributed in three terms. The percentage of the blade profile power, which primarily accounts for aerodynamic drag associated with the rotor blades, experiences a steady reduction as velocity increases (dropping from 48.84% at $v_a = 1\,\text{m/s}$ to 4.11% at $v_a = 40\,\text{m/s}$). The percentage of the induced power, associated with the generation of rotor thrust to counteract the induced downwash also decreases with increasing the velocity (dropping from 4% at $v_a = 1\,\text{m/s}$ to 0.34% at $v_a = 40\,\text{m/s}$). On the other hand, the altitude gain power, which represents the energy required to lift the UAV against gravity as it climbs, exhibits a substantial increase as velocity rises (rises from 47.1% at $v_a = 1\,\text{m/s}$ to 95.54% at $v_a = 40\,\text{m/s}$). The trend suggests that as the UAV's velocity increases, it requires more energy to overcome gravitational forces during the ascent and is a direct result of

the UAV needing greater thrust to climb faster and counteract the increasing gravitational force. Blade profile power and induced power are associated with the aerodynamics and thrust generation of the rotary wing, and they tend to remain relatively constant across different velocities. On the other hand, the power needed for altitude gain, which is directly related to climbing against gravity, becomes the dominant factor as the UAV's velocity increases.

Fig. 31 on the next page illustrates the percentages of power consumption distribution for blade profile power, induced power, parasite power, and the overall power consumption at various velocities in straight and level flight of a rotary wing UAV. Upon analysing equation Eq. (4.9) on page 75 as well as the figure, it becomes apparent that the blade profile power, which accounts for the aerodynamic drag experienced by the aircraft's airfoils, exhibits an increasing trend as velocity rises. This increase is expected, as higher velocities demand more energy to overcome the aerodynamic resistance posed by the airfoil's profile. Induced power, associated with the creation of lift by the aircraft's wings, decreases as velocity increases. This phenomenon is consistent with the inverse relationship between induced power and airspeed, as higher velocities allow the aircraft to generate lift more efficiently. Parasite power, representing non-aerodynamic sources of drag, becomes increasingly dominant as velocity rises. This rise in parasite power is closely tied to the square of the airspeed in the formula, highlighting the exponential nature of drag increase at higher velocities. System parameters influencing parasite power include aircraft shape, surface roughness, and external components. Streamlined designs and surface treatments can help mitigate the impact of parasite power. At lower velocities, blade profile power and induced power are relatively significant, while parasite power contributes less. As velocity increases, parasite power becomes the dominant factor, showcasing the importance of minimizing non-aerodynamic drag sources.

Fig. 31(c) on the next page illustrates the distribution of the percentage of power consumption in hovering status considering different masses of the UAV from $m = 1\,\mathrm{kg}$ to

$m = 40\,\text{kg}$. Blade profile power is more affected by rotor speed, while induced power is more influenced by weight. As mass increases, the UAV needs to generate more thrust to support its weight, and as a result, induced power percentage becomes a larger component of total power consumption while blade profile power percentage becomes relatively smaller. This is why, at a relatively high mass of $m = 40\,\text{kg}$, the induced power contributes significantly, accounting for 99.1% of the total power consumption, while blade profile power becomes a relatively smaller portion.

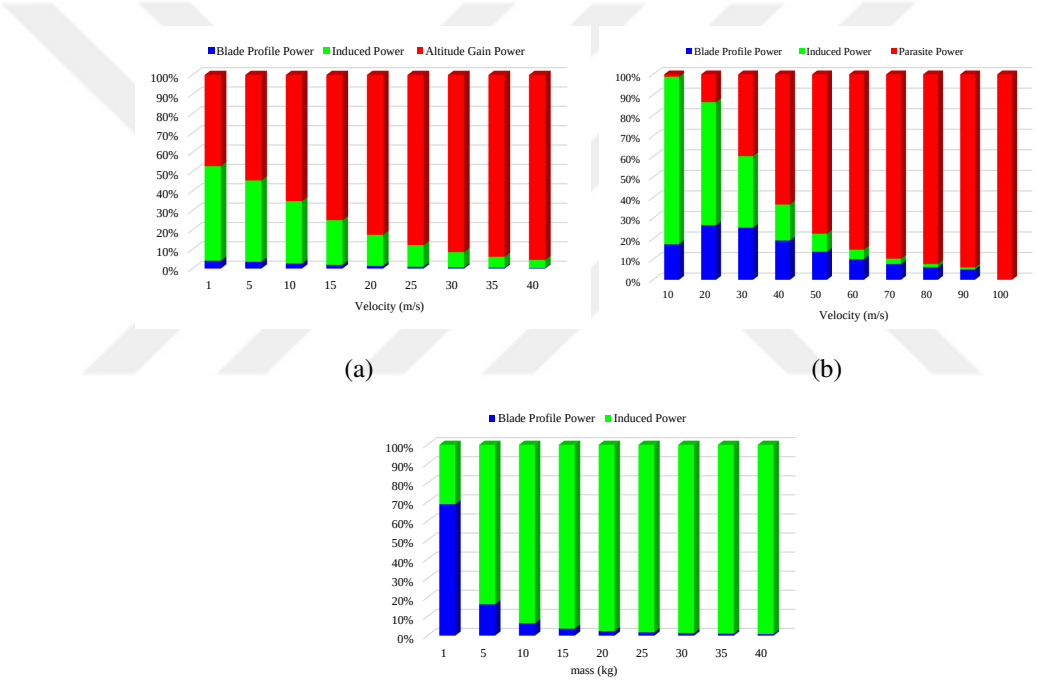


Figure 31: Percentage of power distribution of rotary wing UAV in (a) Ascending, (b) straight and level, and (c) hovering flight status.

Rotary-wing UAVs are commonly deployed to establish temporary connectivity during large events, and they may be situated at a considerable distance from the telecommunication operator's headquarters. To establish this connectivity, the UAV initially ascends to reach the desired altitude. We have considered different altitude ranges for these UAVs, including low-altitude rotary-wing UAVs capable of ascending to 100 meters, middle-altitude

rotary-wing UAVs capable of ascending up to 1 kilometer, and high-altitude rotary-wing UAV with the capacity to ascend up to 5 kilometers. After reaching the desired altitude, the UAV transitions into straight and level flight to reach the designated area where connectivity is required. We have categorized these flight distances as low (up to 1 km), middle (up to 10 km), and high (up to 90 km) horizontal distances. Upon reaching its destination, the UAV remains in a hovering status for one hour to fulfill its mission. We have designated different modes of operation based on various flight specifications, which are categorized as low specifications (L1, L2, L3), middle specifications (M1, M2, ..., M6), and high specifications (H1, H2, ..., H6) as outlined in Table 12. The results of these modes of operation, including energy consumption data of the $m = 10\,\text{kg}$ rotary wing UAVs for ascending in vertical flight with velocity of $v_\text{a} = 20\,\text{m/s}$, horizontal forward flight with a velocity of $v_\text{f} = 30\,\text{m/s}$, hovering for 1 hour, and the overall energy consumption, are provided in Table 12.

Table 12: Energy consumption of rotary-wing UAV in different modes of operation

Modes	h	d_f	$E_\text{rotary,a}$ (Wh)	$E_\text{rotary,f}$ (Wh)	E_out (kWh)	E_total(kWh)
L1	100m	100m	8.3	0.34	1.043	1.051
L2	100m	500m	8.3	1.72	1.043	1.053
L3	100m	1000m	8.3	3.4	1.043	1.054
M1	500m	2km	41.45	6.85	1.046	1.094
M2	500m	4km	41.45	13.71	1.046	1.101
M3	500m	6km	41.45	20.57	1.046	1.108
M4	1km	6km	82.79	20.46	1.051	1.154
M5	1km	8km	82.79	27.28	1.051	1.161
M6	1km	100km	82.79	34.1	1.051	1.167
H1	3km	10km	246.98	33.38	1.071	1.351
H2	3km	20km	246.98	66.76	1.071	1.384
H3	3km	30km	246.98	100.15	1.071	1.418
H4	5km	30km	409.3	98.03	1.092	1.599
H5	5km	60km	409.3	196.07	1.092	1.697
H6	5km	90m	409.3	294.11	1.092	1.795

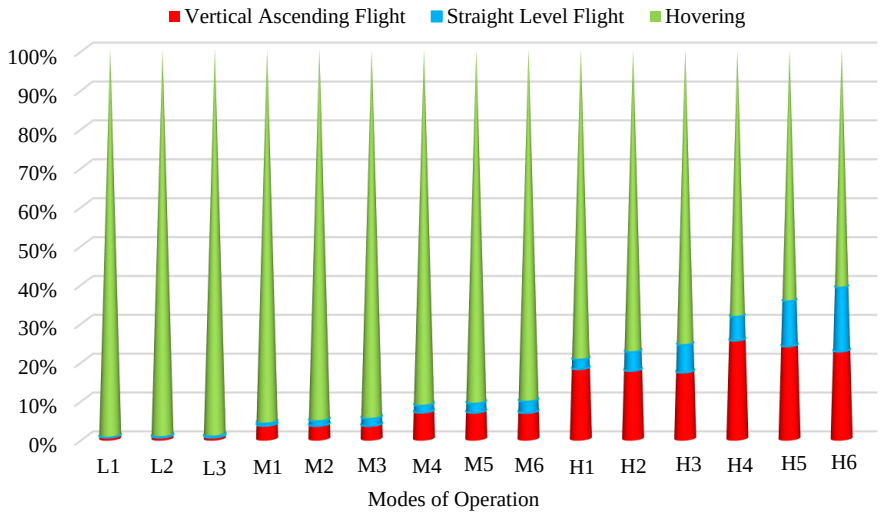


Figure 32: Distribution of energy consumption in vertical ascent flight, straight and level flight and hovering in different modes of operation.

Fig. 32 summarizes the results in Table 12 on the previous page visually. In the case of a low-specification operation, the most significant energy consumption is observed during hovering, accounting for as much as 99.23%. For middle specification operations, the dominant components of energy consumption are vertical ascent flight, which can reach up to 7.17%, and hovering, which can account for as much as 95.6% of the total energy consumption. In high specification operations, the distribution of energy consumption varies. Vertical ascent flight contributes a minimum of 17.84% to 37.8%, horizontal flight ranges from 2.47% to 16.38%, and hovering ranges from 60.83% to 79.27%. In high-altitude operations when the operation altitude is $h = 3\,\text{km}$ and $h = 5\,\text{km}$, the overall energy consumption increases primarily due to additional energy required for vertical ascent flight. Hovering remains the highest contributor to overall energy consumption, followed by energy consumed during vertical ascent.

Considering a mission that includes all the flight modes including ascending, straight level, and hovering and comparing these results with Fig. 6 on page 18, which illustrates the energy harvesting values for a rotary wing UAV in different altitudes, we conclude that

at the altitude of $h = 100$m, the energy harvested from the Sun on the best-case scenario in midlatitude climate type, on $d = 173$rd day of the year, and at noon, is not sufficient to power a rotary wing UAV's mission. For the rotary-wing UAV at the altitude of $h =$ 5km, the energy harvested from the Sun in midlatitude climate type, on the $d = 173$rd and $d = 266$th days of the year, specifically at noon are relatively high; however, they are not sufficient to meet the energy requirements for a mission with high specifications such as a mission at an altitude of $h = 5$km and with high horizontal distances in the order of several tens of kilometers. Overall, we conclude that for all the cases and scenarios irrespective of low-specification missions, middle specifications, or high specifications, the energy harvested from the Sun falls short and in most cases is significantly lower than the energy consumption of the UAV, however, it can extend the operation time period.

Considering the laser power beaming as a charging method to charge the rotary wing UAVs wirelessly, we provide a summary of the energy harvested by rotary-wing UAV operating at an altitude of h=100m with laser power beaming, considering a transmit power of $P_{\mathrm{L}} =$4 kW.

By comparing these energy harvesting values to the overall energy consumption of the rotary-wing UAVs, we can draw conclusions. According to Fig. 11 on page 28 in Section 2.3.1, with a fixed charging station when the laser source is located on top of a building, when the rotary wing UAV is at an altitude of $h =$100m, the harvested energy from laser power beaming in clear weather, rainy, and foggy conditions, is equal to $E_{\mathrm{h,laser}}$=2.7kWh , $E_{\mathrm{h,laser}}$=2.6 kWh, and $E_{\mathrm{h,laser}}$=1.94 kWh, respectively which is found to adequately compensate for the total energy consumption of the UAV. However, at an altitude of $h =$5km, the harvested energy from the laser power beaming in rainy and foggy conditions which are equal to $E_{\mathrm{h,laser}}$=0.68 kWh, and $E_{\mathrm{h,laser}}$=0.5 kWh are insufficient to fully offset the energy consumption at that altitude.

In scenarios involving mobile charging stations, the harvested energy from the mobile charging station which is $E_{\mathrm{h,laser}}$=2.75 kWh during the 1-hour operation is sufficient to

compensate for the energy consumption of the UAV currently on a mission and in a hovering state. It is worth noting that to store this amount of energy we need a high battery density (battery density, also known as energy density, measures how much energy a battery can store in a given mass, i.e., Wh/kg. It's crucial for portable devices and electric vehicles because higher density means longer usage without increasing weight). For example, with a battery density of 1000 Wh/kg, as referenced in [117], storing the energy obtained from laser power beaming requires nearly three batteries. This, in turn, leads to increased weight and subsequently higher energy consumption for the UAV. Researchers are striving to enhance battery density in order to improve energy storage capabilities within UAVs.

In the scenario of power harvesting via SLIPT, as elucidated in Chapter 2, a comparative analysis of the harvested energy against the energy consumption of the rotary-wing UAV leads to the clear conclusion that the energy acquired through SLIPT is notably insufficient. It fails to offset the energy demands of the UAV in any circumstance. This inadequacy stems from the limited transmit power of commercial FSO transmitters, which max out at 5W, making them unable to sufficiently meet the energy requirements of the UAV.

4.3 HAP Based Communication Systems

Recent advances in autonomous avionics and the development of lightweight composite materials have ushered in a new era in the realm of aerial technology. Among the remarkable innovations born of these advancements are HAPs. These fixed-wing UAVs are poised at the forefront of modern aviation, operating at altitudes between 17 and 22 kilometers, comfortably nestled within the stratospheric layer. This altitude range adopted for the HAP's operation is motivated by the fact that in this altitude the wind speed is less intense, and as a consequence, the HAP requires less power to maintain position. Compared to their rotary-wing UAVs counterparts, which predominantly cover lower and middle altitudes, typically up to a few kilometers, HAPs have captured the imagination of the aerospace community for several compelling reasons. One of their most striking attributes

is their potential to deliver significantly lower latency and higher data rate capacity per unit area, making them an appealing alternative to traditional LEOs satellites.

In the realm of airborne networks, there has been a surge of interest, as evidenced by recent comprehensive surveys (references [27–29]). These surveys have delved into various aspects of airborne networks, including network topology, routing protocols, and security. However, one critical factor that has been conspicuously absent from these discussions is energy efficiency, a paramount consideration that can profoundly impact the operational capabilities of airborne networks.

Airborne wireless networks, whether comprising HAPs or rotary-wing UAVs, demand a continuous and reliable supply of energy to remain functional during flight. Energy efficiency is therefore a pivotal aspect that deserves careful attention in the design and operation of these systems. Yet, despite the remarkable strides made in technology and the increasing popularity of airborne networks, the predominant focus has been on enhancing speed, range, and reliability, often overlooking the crucial dimension of energy efficiency.

To address this apparent gap in research and development, there is an urgent need to raise awareness about the pivotal role of energy efficiency in airborne networks and encourage further exploration in this domain. Researchers have already begun to address this challenge, with innovative methods such as integrating solar panels into the design of HAPs (as exemplified in reference [43]) to harness solar energy for sustained operations.

It's worth noting that HAPs can be further categorized into two distinct groups: aerostatic HAPs and aerodynamic HAPs. Aerostatic HAPs, such as balloons and airships, employ buoyancy generated by lifting gases within their envelopes to maintain altitude. On the other hand, aerodynamic HAPs rely on aerodynamic lift forces to stay aloft. Notable examples of these HAPs categories include Google's Loon, Aerostar's Thunderhead Balloon Systems, Aalto's Zephyr, Softbank's Sunglider, and Stratospheric Platforms.

4.3.1 Energy Consumption Model

The energy consumption model of HAPs can be divided into three distinct phases of operation as depicted in Figure 33 on the following page as follows

- **Ascending Flight**: During the ascending flight phase, HAPs have a variety of ascent patterns to choose from. One commonly used pattern is the Spiral pattern, characterized by a spiral motion that gradually gains altitude through circling maneuvers. This pattern allows for a controlled ascent while conserving energy. Another ascent pattern employed by HAPs is the Vertical Takeoff and Landing (VTOL) pattern. VTOL enables precise maneuvering capabilities, allowing HAPs to perform vertical takeoffs and landings as needed. In cases where HAPs operate in the stratosphere, they predominantly utilize the Steady Climb pattern. This pattern involves a continuous and steady ascent to reach their desired operational altitude efficiently.

- **Straight and Level Flight**: After reaching the desired operational altitude, HAPs transition into the straight and level flight phase. During this phase, HAPs maintain a fixed altitude while moving horizontally to reach specific locations of interest. This phase is crucial for providing connectivity to rural and remote areas, as HAPs can effectively cover large areas while operating at a consistent altitude.

- **Circular level flight**: In certain scenarios, HAPs enter the circular level flight phase. During this phase, HAPs follow a circular trajectory with a specific radius and maintain this trajectory for an extended period, which can range from several days to weeks. Circular level flight allows HAPs to provide continuous connectivity to a specific area or follow the Earth's rotation, ensuring prolonged coverage for critical applications

Understanding the energy consumption patterns in these phases is vital for optimizing the performance and mission duration of HAPs in wireless communication systems. Efficient energy management is key to ensuring that HAPs can fulfill their roles effectively and

provide connectivity to various regions, including remote and underserved areas.

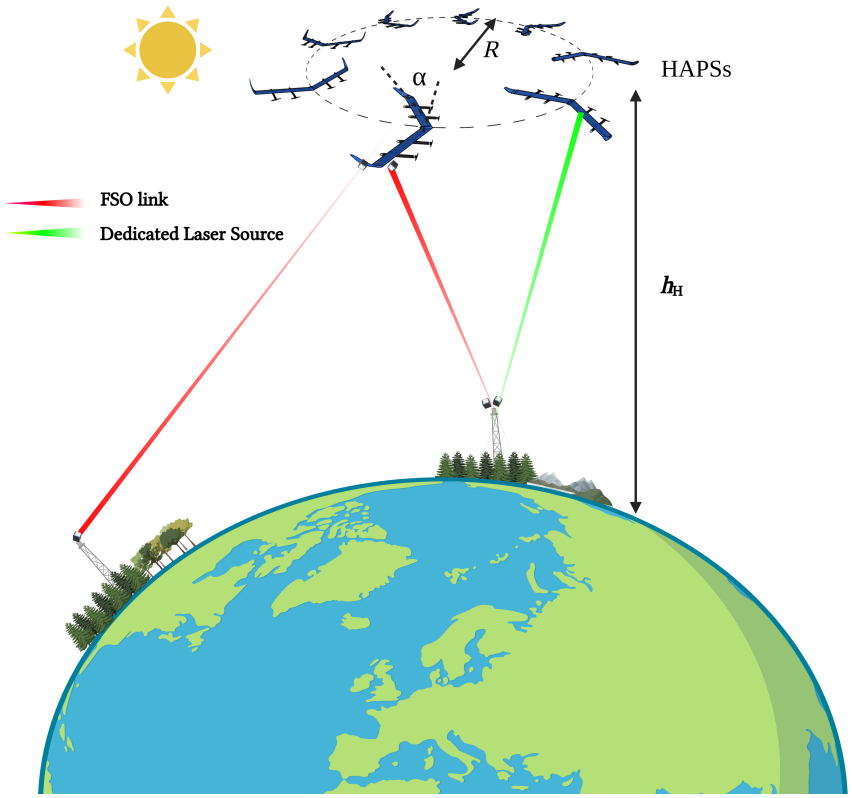


Figure 33: Circular trajectory of HAPs while providing backhauling connectivity.

Considering the flight path angle of γ, the power consumption in a steady climb pattern involves the parasitic power, the induced power, and the power for gaining altitude as given by [118]

$$P_{\text{ascending}} = \frac{1}{\eta_{\text{prop}}} \left(\underbrace{\frac{1}{2}\rho {v_a}^3 A_w C_D}_{\text{parasite}} + \underbrace{\frac{2W^2}{(\pi e_0 A_r)\,\rho A_w v_a}}_{\text{induced}} + \underbrace{W v_a \sin(\gamma)}_{\text{altitudegain}} \right) \tag{4.19}$$

where v_a is the climbing velocity in m/s, A_w is the wing area, C_D is the drag coefficient, A_r is the aspect ratio of the wings, e_0 is the Oswald efficiency, and γ is the flight path angle in degree.

The time (in hours) that it takes to reach the desired altitude of h in a steady climb is calculated by

$$t_{\mathrm{a}} = \frac{h}{3600 \sin(\gamma)\, v_{\mathrm{a}}} \tag{4.20}$$

Therefore, energy consumption in Wh to reach a specific altitude is

$$E_{\mathrm{HAP,ascending}} = P_{\mathrm{ascending}} t_{\mathrm{a}} \tag{4.21}$$

In a straight and level flight, the power consumption of the HAP involves the parasitic power and the induced power as given by

$$P_{\mathrm{Level}} = \underbrace{\frac{\rho v^3 A_{\mathrm{w}} C_{\mathrm{D}}}{2\eta_{\mathrm{prop}}}}_{\text{parasite}} + \underbrace{\frac{2W^2}{\eta_{\mathrm{prop}} (\pi e_0 A_{\mathrm{r}}) \rho A_{\mathrm{w}} v}}_{\text{induced}} \tag{4.22}$$

where v is the velocity in straight and level flight, and other parameters are defined after Eq. (4.19) on the previous page. If the horizontal distance between the headquarter and the mission area is d_{f}, it takes $t_{\mathrm{l}} = {}^{d_{\mathrm{f}}}/_{3600v}$ hours to reach the mission area, and the energy consumption in level flight is

$$E_{\mathrm{HAP,Level}} = P_{\mathrm{Level}} t_{\mathrm{l}} \tag{4.23}$$

For the circular level flight, we assume that the HAP follows a circular trajectory with a radius R at a bank angle α (i.e., the angle between the wing in the lateral plane and the horizontal plane) as depicted in Figure 33 on the preceding page. The banking angle is dependent on the velocity v, circle of radius R, and acceleration due to gravity g, as [43]

$$\alpha = \tan^{-1}\left(\frac{v^2}{gR}\right) \tag{4.24}$$

The power consumption of the HAPs in circular motion is modeled like the power required for a steady and level flight in Eq. (4.22) with some modifications. In circular level flight, the effective weight is increased by the load factor (load factor is defined as the inverse of cosine of the bank angle, i.e., $n = 1/\cos(\alpha)$), i.e., $W_{\mathrm{eff}} = nW$, thus, the effective induced power required is increased by the load factor squared. Therefore, the power consumption

in circular motion is [43]

$$P_{\text{Circular}} = \underbrace{\frac{\rho v^3 A_{\text{w}} C_{\text{D}}}{2\eta_{\text{prop}} \cos^2(\alpha)}}_{\text{parasite}} + \underbrace{\frac{2W^2}{\eta_{\text{prop}} \cos^2(\alpha)(\pi e_0 A_{\text{r}}) \rho A_{\text{w}} v}}_{\text{induced}} \tag{4.25}$$

The time taken to complete one circular track in hours is

$$T_{\text{Circle}} = \frac{2\pi R \sqrt{\cos(\alpha)}}{3600 v} \tag{4.26}$$

The energy required (in Watt-hour) for maintaining a flight for one circular track is

$$E_{\text{Circle}} = T_{Circular} P_{\text{Circular}} \tag{4.27}$$

For 24-hour mission operations in a circular trajectory, the number of times that HAPs makes a circular track during the 24 hours is given by

$$N_{\text{circle}} = v \frac{43200}{\pi R \sqrt{\cos(\alpha)}} \tag{4.28}$$

The energy consumption during the considered 24-hour circular mission is

$$E_{\text{Circular}} = 24 P_{\text{Circular}} \tag{4.29}$$

4.3.2 Communication Model

Cellular backhauling for rural areas is a common application of HAPs. Let's consider a scenario where a mobile operator deploys a HAP to provide backhaul connectivity to base stations on the ground as shown in Figure 34 on the following page. The altitude of operation is supposed to be in the stratosphere and it is h. The radius of the circular flight is R.

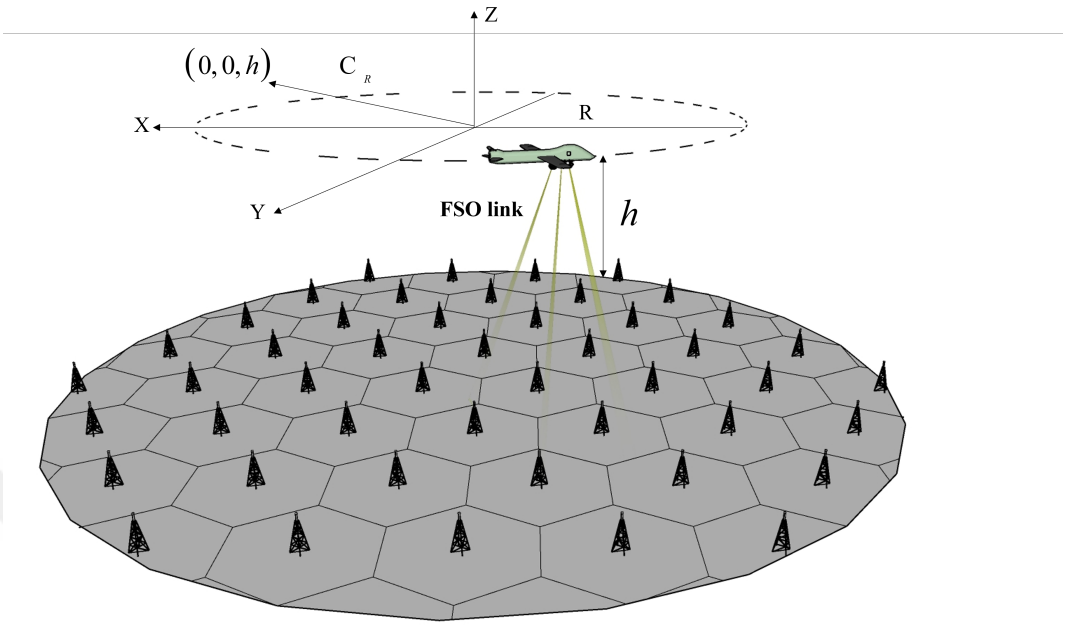


Figure 34: HAP-based FSO communications system.

For simplification of computations, we model the trajectory as a discrete time model. Let T denote the mission time of HAP to complete the circular trajectory. This is divided into N equal-length time slots each with a duration of $\delta t = T/N$. If δt is chosen sufficiently small (i.e., N is chosen sufficiently large), the location of the HAP can be assumed to be fixed during each time slot. We define $\mathbf{v}[n] = (v_x[n], v_y[n], v_z[n])$ as the velocity of the UAV during the n^{th} time slot, where $v_x[n], v_y[n]$, and $v_z[n]$ are the velocity components of $\mathbf{v}[n]$ in 3D Cartesian coordinates. We formulate the HAP's motion state in circular flight as [119]

$$\mathbf{p}[n] = \mathbf{p}[n-1] + \mathbf{v}[n]\,\delta t \quad n = 1, ..., N. \tag{4.30}$$

We further assume that the HAP is in a quasi-static equilibrium condition. This means that the HAP moves smoothly with a constant speed at each time slot. We assume a LOS communication link between the HAP and the base stations on the ground. Assume that the HAP can provide connectivity to base stations, each with a position vector of $\mathbf{Q}_i[n] = (q_{i,x}[n], q_{i,y}[n], q_{i,z}[n])$, $i \in \{1, .., F\}$. The data rate that can be supported is given by [120]

Table 13: Specifications of the solar-powered HAP

Parameter	Variable	Value
Total Mass of the HAP	m(kg)	75 and 300
Wing Area	A_{w} $\left(\mathrm{m}^2\right)$	75
Drag Coefficient	C_{D}	0.007
Propeller Efficiency (%)	η_{prop}	80 %
Air density	ρ $\left(\mathrm{kg/m}^3\right)$	0.088
Circle of Radius	R (km)	16
Aspect ratio of the wing	A_{r}	12.5
Altitude of operation	h (km)	20
Flight path angle	γ°	40
Velocity in ascending flight	v_{a} (m/s)	30

$$\Re_i[n] = \frac{B_{\mathrm{FSO}}}{2\ln 2} \ln\left(1 + k_1 e^{-2\beta_{\mathrm{FSO}} \cdot \|\mathbf{p}[n] - \mathbf{Q}_i[n]\|}\right) \tag{4.31}$$

where B_{FSO} is the bandwidth of FSO link and β_{FSO} is extinction coefficient in m^{-1}. In Eq. (4.31), k_1 is given by

$$k_1 = \begin{cases} \dfrac{e^{2\alpha\mu^*}}{2\pi e}\left(\dfrac{1-e^{-\mu^*}}{\mu^*}\right)\dfrac{\gamma^2}{\alpha^2} & (0 < \alpha < 0.5) \\ \dfrac{\gamma^2}{2\pi e \alpha^2} & (0.5 < \alpha < 1) \end{cases}, \tag{4.32}$$

where, γ is the average optical signal-to-noise-ratio.

4.3.3 Comprehensive Energy Assessment of Solar Powered HAPs

First, we analyze the distribution of power consumption in different phases of the flight including vertical ascend flight, straight level flight, and circular flight. In vertical ascending flight power consumption includes three key terms: induced power, parasite power, and altitude gain power. The results are visually represented in Figure 35 on the following page and Figure 36 on page 98 for m=300kg and m=75kg HAP, respectively. The main findings reveal a clear relationship between HAP velocity and power distribution. At lower velocities, the percentage of power consumption in the altitude gain power term is high, indicating significant energy allocation to gaining altitude. Induced and parasite powers

are present but less dominant. As HAP's velocity increases, there's a shift in power distribution. Parasite power becomes increasingly dominant, particularly at higher velocities around v=150 m/s, surpassing altitude gain power in terms of percentage contribution. Induced power exhibits a contrasting trend, decreasing as velocity increases and becoming relatively negligible at higher velocities. In conclusion, the analysis highlights the changing power consumption patterns during HAP ascending flight, with altitude gain power dominating at low velocities and parasite power taking precedence at higher velocities.

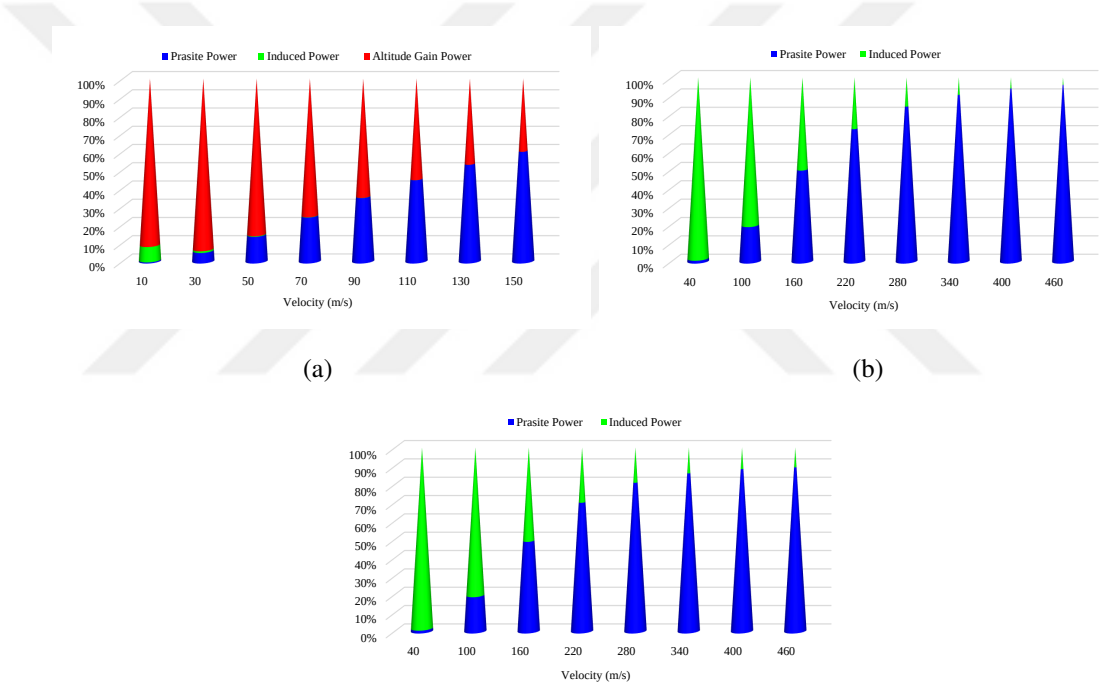


Figure 35: Percentage of power distribution of m=300kg HAP in (a) Ascending, (b) straight and level, and (c) circular flight status.

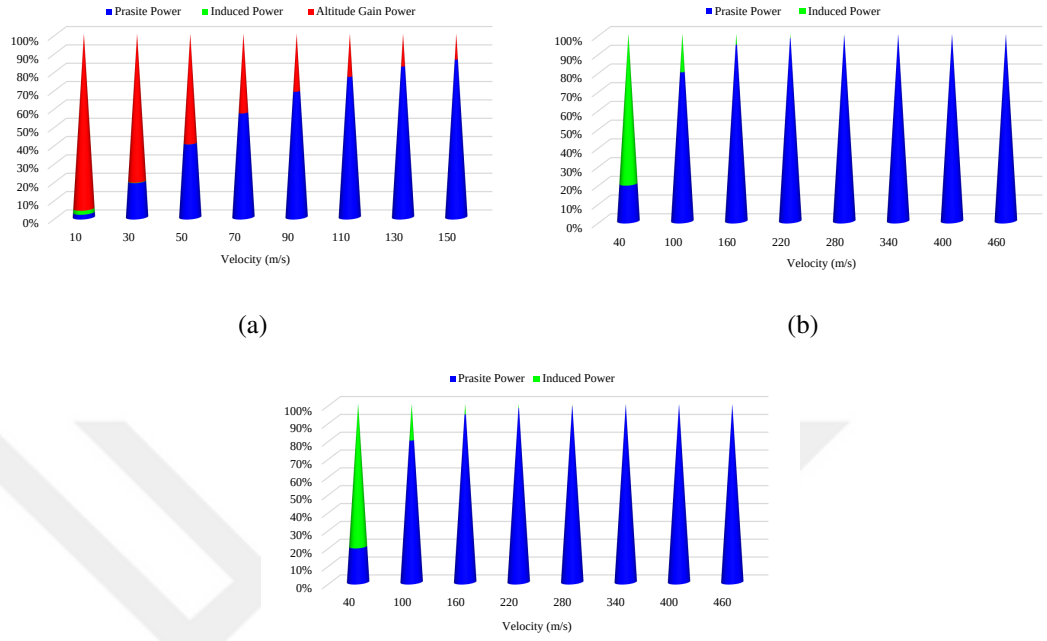


Figure 36: Percentage of power distribution of m=75kg HAP in (a) Ascending, (b) straight and level, and (c) circular flight status.

In our investigation of power consumption during steady and level flight of HAPs, we directed our attention toward two fundamental factors contributing to the overall power usage: induced power and parasite power. The principal findings elucidate a distinct correlation between HAP velocity and the distribution of power. During steady and level flight at lower speeds, induced power emerges as the predominant factor, responsible for a substantial proportion of energy consumption. It's worth noting that induced power plays a critical role in maintaining lift and altitude at these lower velocities, while parasite power also contributes, albeit to a lesser degree. As velocity increases during steady and level flight, there is a noticeable shift in power distribution. Parasite power begins to take precedence as the primary contributor to energy consumption. This rise in parasite power becomes particularly conspicuous at higher velocities, signifying its ascendancy as the principal driver of power consumption. A noteworthy trend emerges in the reduction of induced power as

velocity escalates. This reduction is especially pronounced at higher speeds, implying that less power is needed to sustain lift and altitude as the HAP gains momentum, with parasite power assuming greater significance. In summary, the analysis of steady and level flight for HAPs reveals a dynamic power consumption pattern: induced power prevails at lower velocities, ensuring lift and stability, while parasite power assumes prominence at higher speeds.

In our examination of power consumption during circular and level flight of HAPs, we focused on two primary elements contributing to the overall energy usage: induced power and parasite power. The primary findings illuminate a distinct association between HAP velocity and power distribution. During circular and level flight at lower speeds, induced power takes center stage as the dominant factor, accounting for a significant portion of power consumption. It is crucial to emphasize that induced power plays a vital role in maintaining lift and altitude at these lower velocities, with parasite power also playing a role, though to a lesser extent. As velocity increases during circular and level flight, there is a noticeable transition in power distribution. Parasite power begins to assume a dominant role as the primary contributor to energy consumption. This increase in parasite power is particularly pronounced at higher velocities, signifying its role as the primary driver of power consumption. An interesting trend emerges as induced power decreases with increasing velocity up to a certain point, after which it starts to increase. This is due to the fact that as velocity increases, the banking angle also increases, impacting induced power. In summary, induced power dominates at lower velocities, ensuring lift and stability, while parasite power takes precedence as the most significant factor at higher velocities.

Next, we provide energy consumption in different phases of the flight including vertical ascending flight, straight and level flight, and circular flight of the HAPs considering the specifications given in Table 13 on page 96. Figure 37(a) on the next page and Figure 37(b) on the following page illustrate the steady climb flight energy consumption of the HAP with a mass of $m = 75$kg and $m = 300$kg, respectively with a flight angle of $\gamma = 40^\circ$ as well

as the time taken to reach the altitude of $h = 20$km, with a focus on the relationship with velocity. The graph demonstrates that as velocity increases, energy consumption initially decreases until reaching a certain point. Beyond that point, energy consumption begins to increase.

In the case of HAPs, it is essential to uphold a minimum velocity to prevent descent and maintain stability. The data indicates that there exists an optimal velocity at which energy consumption is at its lowest. Specifically, when the HAP's mass is m=75kg, this optimal velocity measures 24 m/s. However, this optimal velocity rises to 60 m/s as the HAP's mass increases to m=300kg.

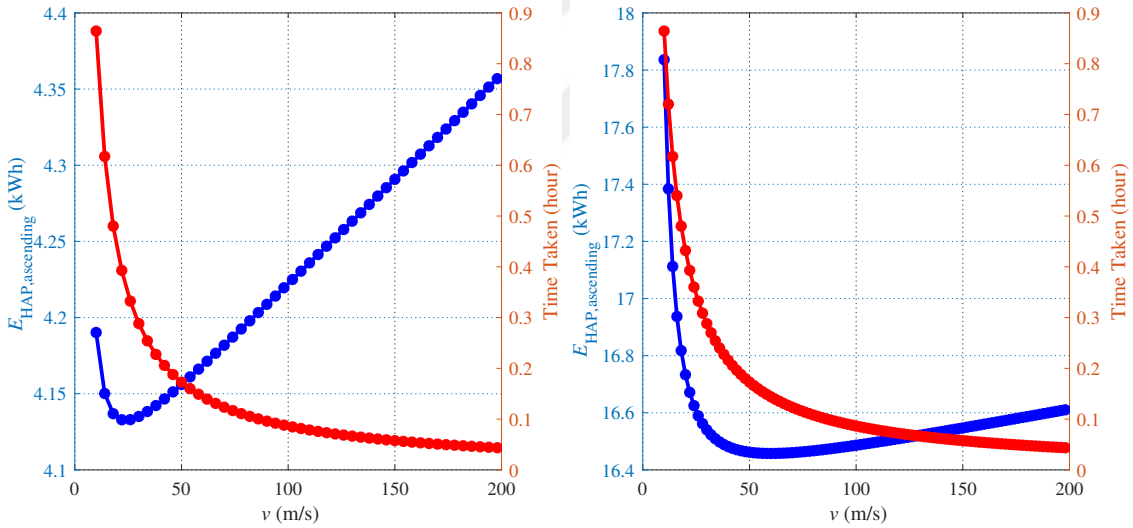


Figure 37: Energy consumption of the HAP in steady climb flight with respect to velocity (a) m=75kg, (b) m=300kg.

Next, we analyze the energy consumption of HAPs weighing m=75kg and m=300kg during steady level flight at an altitude of $h = 20$km to reach the desired destination located $d_{\text{f}} = 500$km away from its origin location as well as the time taken to reach there with respect to velocity provided in Figure 38 on the next page. As observed, the optimal velocity for the HAP is linked to its mass. When the HAP's mass is m=75kg, this optimal velocity measures 80 m/s. However, this optimal velocity rises to 200 m/s as the HAP's

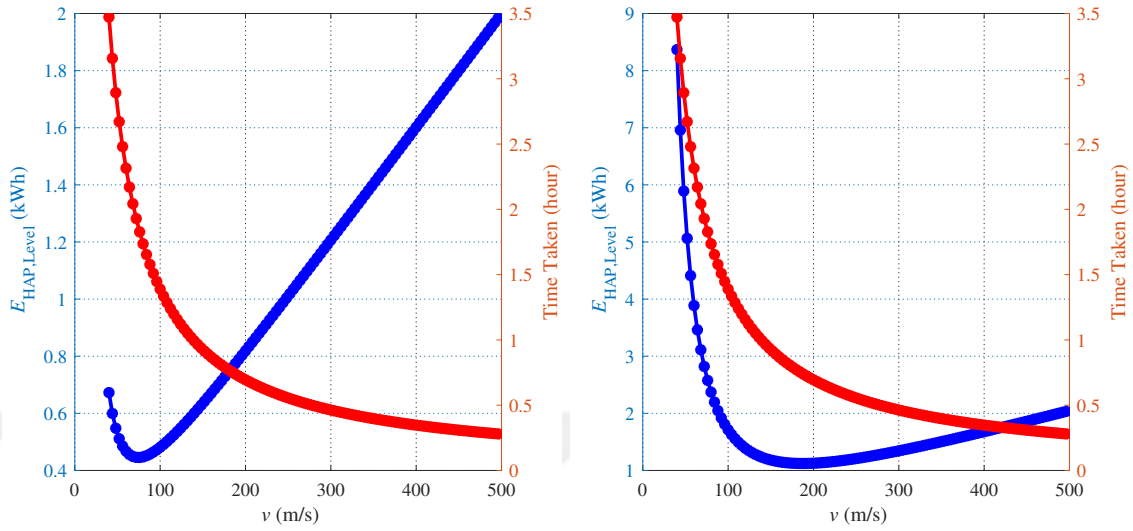


Figure 38: Energy consumption of the HAP in straight level flight with respect to velocity (a) m=75kg, (b) m=300kg.

mass increases to m=300kg.

Based on Equation (4.29) on page 94, the energy consumption of HAPs in circular flight with a radius of R=16km is shown in Figure 39 on the next page for two masses equal to m=75kg, and m=300kg. From the figure, energy consumption follows a similar trend as the other figures depicting the relationship between velocity and energy consumption. Initially, energy consumption decreases with increasing velocity until a certain point, after which it increases significantly. As mentioned earlier, HAPs require a minimum velocity to prevent descent and potential falls. Additionally, it is evident that increasing the weight of the HAP leads to higher energy consumption and higher optimum velocity. The optimum velocity in terms of energy consumption in circular flight for the HAP with m=75kg is 50 m/s, and for the one with m=300kg is 125 m/s.

Table 14 on the following page and Table 15 on page 103 demonstrate that the energy usage varies depending on the specific phase of the flight for two HAPs, one with a mass of $m = 75$kg and the other with a mass of $m = 300$kg. The lowest percentage of energy consumption belongs to straight level flight, with values of 5.21% and 6.73% for the $m =$

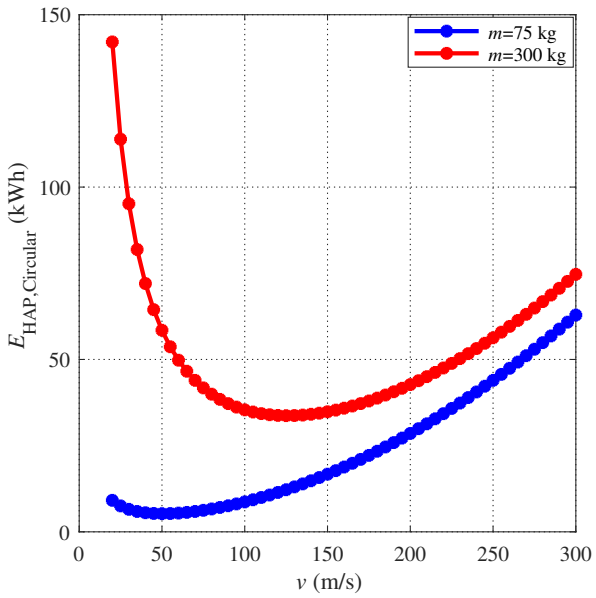


Figure 39: Energy consumption of the HAP in circular flight with respect to velocity

75kg and $m = 300$kg HAPs, respectively. On the other hand, the highest percentage of energy consumption occurs during circular motion, with values of 53.73% for the $m = 75$kg HAP and 70% for the $m = 300$kg HAP. When comparing the energy consumption percentages of the $m = 75$kg HAP with the $m = 300$kg HAP across different phases, the energy consumption during vertical ascending flight decreases from 41.09% to 23.25%. However, the percentage increases for straight level flight from 5.21% to 6.73% and for circular flight phases from 53.73% to 70%.

Table 14: Energy consumption of a m=75kg HAP in different modes

Flight Mode	**Time Taken** (hour)	**Energy Consumption** (kWh)	**Percentage**
Ascending	0.28	4.13	41.04 %
Straight level	2.31	0.524	5.21 %
Circular	24	5.4	53.73 %
Total	26.59	10.05	100 %

Table 15: Energy consumption of a m=300kg HAP in different modes

Flight Mode	**Time Taken** (hour)	**Energy Consumption** (kWh)	**Percentage**
Ascending	0.28	16.54	23.35 %
Straight level	2.31	4.79	6.73 %
Circular	24	49.78	70 %
Total	26.59	71.11	100 %

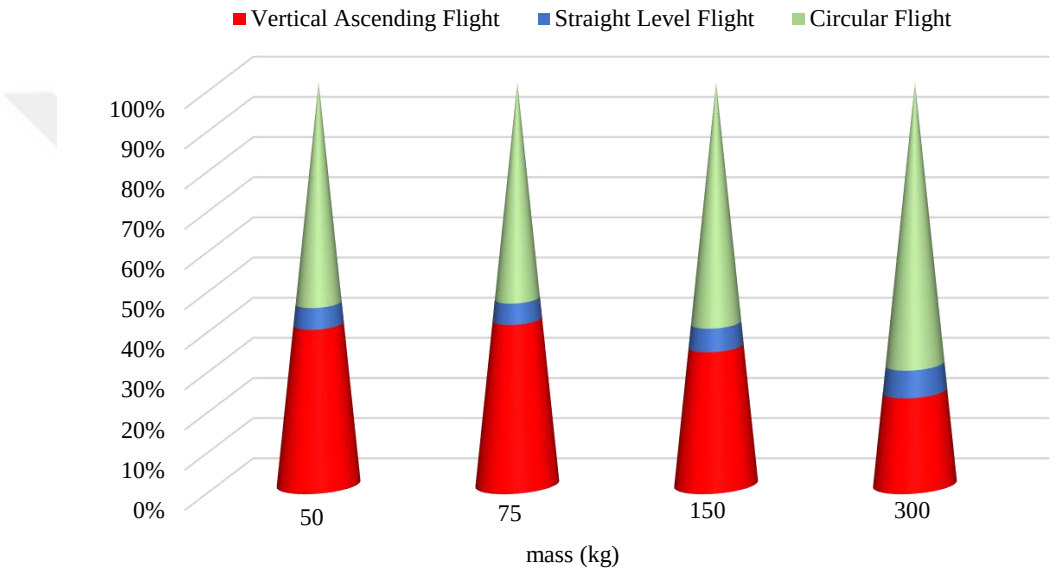


Figure 40: Distribution of energy consumption in three phases of flight of the HAP

Drawing insights from the data presented in Figure 40, our conclusion is that an increase in mass leads to a decrease in the proportion of energy allocated to vertical ascending flight and an increase in that assigned to straight level flight and circular flight. While vertical ascending flight is the most power-consuming phase, it's worth noting that the time spent on this phase is relatively small compared to the total mission time assigned to the HAP.

For the HAP with the mass of m=75kg, and m=300kg, the total energy consumption is 10.05 kWh, and 71.11 kWh, respectively. Except for one special case of energy harvesting on 357th day of the year (which is $E_{\text{in}} = 48$kWh), other values for energy consumptions for both cases of HAPs are consistently lower than the energy harvested by the HAP over its 24-hour operational mission. Specifically, on the 80th, 173rd, 266th, and 357th days

of the year, the energy harvested from the Sun amounts to 81.6 kWh, $E_{\text{in}} = 243.35$kWh, $E_{\text{in}} = 196.7$kWh, and $E_{\text{in}} = 48$kWh respectively. Notably, these values are in most cases higher than the overall energy consumption of the HAPs for the given scenario.

It is worth nothing that energy storage is a crucial aspect for HAPs reliant on solar power. With a battery density of 1000 Wh/kg, each kilogram of batteries can store 1000 watt-hours of energy. For example, to store 200 kWh of energy, 200 kilograms of batteries are required, leading to an overall HAP mass increase of 200 kg. Therefore, to decide on the number of batteries a HAP can handle, we need to consider the payload capacity of the HAP. This additional weight can impact the HAP's flight performance. Advancements in battery technology hold the potential to improve the overall performance and capabilities of these HAPs in the future.

In the case of laser power beaming provided in Chapter 2, when comparing the harvested energy to the energy consumption of the HAPs over 24 hours, it is evident that the harvested energy from the laser power beaming is sufficient only in the case when the mass is m=75kg and the angular spread of the laser beam is low enough like when it is $\Delta\theta = 1 \times 10^{-5}$, and $\Delta\theta = 1 \times 10^{-6}$, the harvested energy will be $E_{\text{h,laser}} = 46.4$ kWh, and $E_{\text{h,laser}}$ =54.3kWh, respectively, which is sufficient to compensate for the energy consumption of HAP with m=75kg mass which is about 10.05 kWh.

For the case when the mass of the HAP is m=300kg, this amount of harvested energy from laser power beaming can significantly prolong the lifetime of the HAPs but cannot completely compensate for all the energy consumption required for the whole mission.

In the case of a mobile charging station where another dedicated HAP is used to provide power to the HAP currently on its mission, the harvested energy over 24 hours amounts to $E_{\text{h,Laser}} = 66$kWh. This energy is indeed sufficient to charge a m=75kg HAP but falls short for a HAP with a mass of m=30kg. However, it can still notably extend the operational lifespan of the latter.

In the case of SLIPT when the angular spread is $\Delta\theta = 1 \times 10^{-5}$, and $\Delta\theta = 1 \times 10^{-6}$,

the energy harvesting from SLIPT are $E_{\mathrm{h,SLIPT}} = 0.415\mathrm{kWh}$, and $E_{\mathrm{h,SLIPT}} = 0.458\mathrm{kWh}$, respectively, which are extremely low to compensate the energy consumption of the HAPs.

CHAPTER V

CONCLUSIONS AND FUTURE WORK

In this chapter, we comprehensively examine the objectives and outcomes of the entire dissertation, with a particular focus on highlighting the significant contributions of this research. Additionally, we outline potential avenues for future research to build upon the findings and extend the scope of this study.

5.1 Conclusions

In this thesis, we have embarked on a journey to explore and address the critical issue of energy efficiency in optical wireless communication systems deployed in challenging environments, encompassing both USNs and airborne networks. Our investigation spanned various aspects, from optimizing trajectories to harnessing renewable energy sources, ultimately aiming to prolong mission duration and enhance network sustainability.

In the realm of underwater sensor networks, we tackled the energy consumption challenge by devising optimal trajectories for AUVs. These trajectories considered VLC-based data retrieval from sensor nodes while factoring in the dynamic influence of ocean currents. Our results demonstrated that our proposed trajectories reactively adapted to ocean currents, yielding significant energy savings and reduced mission times. Importantly, these improvements became more pronounced as the number of sensor nodes increased. Furthermore, our study shed light on the critical role of AUV speed in optimizing the trade-off between mission time and energy consumption.

To delve deeper into energy efficiency, we introduced a solar-powered AUVs capable of data collection in underwater environments. By optimizing its 3D trajectory, we ensured an energy-aware approach to data retrieval. The results of this endeavor illustrated the advantages of our energy-aware trajectory, as it extended the autonomous operation duration

considerably, reducing the need for frequent battery recharging visits to the home base.

Shifting our focus to airborne networks, we explored energy-efficient solutions involving solar-powered rotary-wing UAVs and HAPs. In the case of rotary-wing UAVs, we concentrated on altitude optimization, an endeavor crucial for efficient FSO backhauling to ground base stations. Our findings highlighted the critical interplay between operation altitude, solar panel efficiency, and UAV weight. By carefully selecting the operation altitude, we harnessed the potential to significantly enhance UAV airborne time through energy optimization.

Within the domain of HAPs, we introduced solar-powered HAPs and assessed energy efficiency. We explored diverse methods for remote charging, eliminating the need for these platforms to return to the home base for recharging. This approach promises to extend mission durations and enhance network resilience.

Collectively, this thesis advances our understanding of energy-efficient optical wireless communication systems in challenging environments. Our research contributes solutions that not only conserve energy but also enhance network sustainability, making it possible to maintain critical communication links in hard-to-reach areas for extended periods. By optimizing trajectories, harnessing renewable energy sources, and considering dynamic environmental factors, we have laid the foundation for more efficient and resilient optical wireless communication systems in both underwater and airborne networks.

As the demand for reliable and energy-efficient communication in these environments continues to grow, the findings and methodologies presented in this thesis offer valuable insights and practical solutions, ultimately contributing to the advancement of communication technology in challenging and remote settings.

5.2 Future Work

The research presented in this thesis has paved the way for a multitude of exciting avenues for future investigation, as we continue to address the challenges of energy-efficient optical

wireless communication systems in hard-to-reach areas of both underwater and airborne networks. In the quest for sustainable and resilient communication, several promising directions emerge for further exploration:

One promising area for future research is the exploration of laser power beaming in underwater environments. By investigating the feasibility of laser-based energy transfer to AUVs and other submerged sensor nodes, we aim to unlock new possibilities for extended mission durations and enhanced operational capabilities. This research could involve developing efficient laser power beaming systems tailored to the unique characteristics of underwater communication.

In both airborne networks and solar-powered underwater sensor nodes, energy management remains a critical challenge, especially in environments where power resources are scarce and intermittently available. Future work will delve into the application of Reinforcement Learning (RL) techniques to address this challenge comprehensively.

RL can be employed to optimize the energy consumption and harvesting strategies of solar-powered UAVs and HAPs. By dynamically adapting to changing environmental conditions, RL algorithms can make real-time decisions on altitude, flight path, and energy harvesting methods, maximizing the utilization of available energy sources and extending mission durations.

In the context of underwater sensor networks, RL can play a pivotal role in managing energy resources efficiently. RL algorithms can learn to adapt AUV trajectories and data retrieval schedules based on real-time energy availability, data rate constraints, and mission objectives. This adaptive approach can significantly enhance the autonomy and energy sustainability of underwater sensor networks, reducing the need for manual intervention.

One of the key advantages of RL is its ability to adapt and optimize strategies in response to the dynamic energy landscape. By integrating RL-based energy management systems into optical wireless communication networks, we can mitigate the impact of energy scarcity, thereby ensuring the continuity of critical communication links.

Furthermore, RL algorithms can enhance the resilience of these networks by enabling autonomous decision-making in the face of unforeseen challenges, such as unexpected energy fluctuations or changing environmental conditions. This adaptability ensures that communication systems remain operational even in the harshest and most unpredictable conditions.

In conclusion, the future work outlined here represents a natural extension of our current research efforts. By exploring laser power beaming and adopting Reinforcement Learning for energy management in both underwater and airborne networks, we aim to push the boundaries of energy efficiency and sustainability in optical wireless communication systems. These advancements hold the potential to revolutionize communication capabilities in hard-to-reach areas, ultimately benefiting a wide range of applications, from environmental monitoring to disaster response and beyond.

As we embark on these exciting research trajectories, we anticipate contributing further to the development of energy-efficient and resilient communication technologies for challenging environments.

REFERENCES

[1] P. H. Pathak, X. Feng, P. Hu, and P. Mohapatra, "Visible light communication, networking, and sensing: A survey, potential and challenges," *IEEE Communications Surveys Tutorials*, vol. 17, no. 4, pp. 2047–2077, 2015.

[2] A. Al-Kinani, C.-X. Wang, L. Zhou, and W. Zhang, "Optical wireless communication channel measurements and models," *IEEE Communications Surveys Tutorials*, vol. 20, no. 3, pp. 1939–1962, 2018.

[3] M. A. Khalighi and M. Uysal, "Survey on free space optical communication: A communication theory perspective," *IEEE Communications Surveys Tutorials*, vol. 16, no. 4, pp. 2231–2258, 2014.

[4] Z. Zeng, S. Fu, H. Zhang, Y. Dong, and J. Cheng, "A survey of underwater optical wireless communications," *IEEE Communications Surveys Tutorials*, vol. 19, no. 1, pp. 204–238, 2017.

[5] J. Ren, Y. Zhang, K. Zhang, A. Liu, J. Chen, and X. S. Shen, "Lifetime and energy hole evolution analysis in data-gathering wireless sensor networks," *IEEE Transactions on Industrial Informatics*, vol. 12, no. 2, pp. 788–800, 2016.

[6] A. Celik, N. Saeed, B. Shihada, T. Y. Al-Naffouri, and M.-S. Alouini, "End-to-end performance analysis of underwater optical wireless relaying and routing techniques under location uncertainty," *IEEE Transactions on Wireless Communications*, vol. 19, no. 2, pp. 1167–1181, 2020.

[7] N. Javaid, N. Ilyas, A. Ahmad, N. Alrajeh, U. Qasim, Z. A. Khan, T. Liaqat, and M. I. Khan, "An efficient data-gathering routing protocol for underwater wireless sensor networks," *Sensors*, vol. 15, no. 11, pp. 29149–29181, 2015.

[8] A. Ahmad, A. Wahid, and D. Kim, "Aeerp: Auv aided energy efficient routing protocol for underwater acoustic sensor network," in *Proceedings of the 8th ACM workshop on Performance monitoring and measurement of heterogeneous wireless and wired networks*, pp. 53–60, 2013.

[9] N. Wang and J. Wu, "Trajectory scheduling for timely data report in underwater wireless sensor networks," in *2015 IEEE Global Communications Conference (GLOBECOM)*, pp. 1–6, IEEE, 2015.

[10] N. Ilyas, N. Javaid, Z. Iqbal, M. Imran, Z. A. Khan, U. Qasim, and M. Shoaib, "Aaeerp: Advanced auv-aided energy efficient routing protocol for underwater wsns," in *2015 IEEE 29th International Conference on Advanced Information Networking and Applications*, pp. 77–83, IEEE, 2015.

[11] X. Zhuo, M. Liu, Y. Wei, G. Yu, F. Qu, and R. Sun, "Auv-aided energy-efficient data collection in underwater acoustic sensor networks," *IEEE Internet of Things Journal*, 2020.

[12] C. Qin, J. Du, J. Wang, and Y. Ren, "A hierarchical information acquisition system for auv assisted internet of underwater things," *IEEE Access*, vol. 8, pp. 176089–176100, 2020.

[13] F. A. Khan, S. A. Khan, D. Turgut, and L. Bölöni, "Scheduling multiple mobile sinks in underwater sensor networks," in *2015 IEEE 40th Conference on Local Computer Networks (LCN)*, pp. 149–156, IEEE, 2015.

[14] G. A. Hollinger, S. Choudhary, P. Qarabaqi, C. Murphy, U. Mitra, G. S. Sukhatme, M. Stojanovic, H. Singh, and F. Hover, "Underwater data collection using robotic sensor networks," *IEEE Journal on Selected Areas in Communications*, vol. 30, no. 5, pp. 899–911, 2012.

[15] P. Gjanci, C. Petrioli, S. Basagni, C. A. Phillips, L. Bölöni, and D. Turgut, "Path finding for maximum value of information in multi-modal underwater wireless sensor networks," *IEEE Transactions on Mobile Computing*, vol. 17, no. 2, pp. 404–418, 2017.

[16] M. Soulignac, "Feasible and optimal path planning in strong current fields," *IEEE Transactions on Robotics*, vol. 27, no. 1, pp. 89–98, 2010.

[17] A. A. R. Al Makdah, N. Daher, D. Asmar, and E. Shammas, "Three-dimensional trajectory tracking of a hybrid autonomous underwater vehicle in the presence of underwater current," *Ocean Engineering*, vol. 185, pp. 115–132, 2019.

[18] X. Yao, F. Wang, J. Wang, and X. Wang, "Bilevel optimization-based time-optimal path planning for auvs," *Sensors*, vol. 18, no. 12, p. 4167, 2018.

[19] J. G. Bellingham, *Platforms: autonomous underwater vehicles*, vol. 6. San DIego, CA: Academic Press, 2008.

[20] J.-M. Tung, M.-F. Guo, J. Guo, F.-C. Chiu, and S.-W. Cheng, "Design of an underwater glider with fore and aft buoyancy engines," in *2007 Symposium on Underwater Technology and Workshop on Scientific Use of Submarine Cables and Related Technologies*, pp. 446–450, IEEE, 2007.

[21] J. Cao, D. Lu, D. Li, Z. Zeng, B. Yao, and L. Lian, "Smartfloat: A multimodal underwater vehicle combining float and glider capabilities," *IEEE Access*, vol. 7, pp. 77825–77838, 2019.

[22] A. A. R. Al Makdah, N. Daher, D. Asmar, and E. Shammas, "Three-dimensional trajectory tracking of a hybrid autonomous underwater vehicle in the presence of underwater current," *Ocean Engineering*, vol. 185, pp. 115–132, 2019.

[23] K. A. Mahmoodi and M. Uysal, "Auv trajectory optimization for an optical underwater sensor network in the presence of ocean currents," in *2021 IEEE International Black Sea Conference on Communications and Networking (BlackSeaCom)*, pp. 1–6, IEEE, 2021.

[24] D. R. Blidberg, S. Chappell, and J. C. Jalbert, "Long endurance sampling of the ocean with solar powered auv's," *IFAC Proceedings Volumes*, vol. 37, no. 8, pp. 561–566, 2004.

[25] D. M. Crimmins, C. T. Patty, M. A. Beliard, J. Baker, J. C. Jalbert, R. J. Komerska, S. G. Chappell, and D. R. Blidberg, "Long-endurance test results of the solar-powered auv system," in *OCEANS 2006*, pp. 1–5, IEEE, 2006.

[26] S. Janji, A. Samorzewski, M. Wasilewska, and A. Kliks, "On the placement and sustainability of drone FSO backhaul relays," *IEEE Commun. Lett.*, vol. 11, no. 8, pp. 1723–1727, 2022.

[27] X. Cao, P. Yang, M. Alzenad, X. Xi, D. Wu, and H. Yanikomeroglu, "Airborne communication networks: A survey," *IEEE Journal on Selected Areas in Communications*, vol. 36, no. 9, pp. 1907–1926, 2018.

[28] T. Naous, M. Itani, M. Awad, and S. Sharafeddine, "Reinforcement learning in the sky: A survey on enabling intelligence in ntn-based communications," *IEEE Access*, 2023.

[29] A. Baltaci, E. Dinc, M. Ozger, A. Alabbasi, C. Cavdar, and D. Schupke, "A survey of wireless networks for future aerial communications (facom)," *IEEE Communications Surveys & Tutorials*, vol. 23, no. 4, pp. 2833–2884, 2021.

[30] C. Zhang *et al.*, "3D deployment of multiple UAV-mounted base stations for UAV communications," *IEEE Trans. Commun.*, vol. 69, no. 4, pp. 2473–2488, 2021.

[31] J. Lyu, Y. Zeng, R. Zhang, and T. J. Lim, "Placement optimization of UAV-mounted mobile base stations," *IEEE Commun. Lett*, vol. 21, no. 3, pp. 604–607, 2017.

[32] Y. Zeng, X. Xu, and R. Zhang, "Trajectory design for completion time minimization in UAV-enabled multicasting," *IEEE Trans Wireless Commun.*, vol. 17, no. 4, pp. 2233–2246, 2018.

[33] P. Yang *et al.*, "Three-dimensional continuous movement control of drone cells for energy-efficient communication coverage," *EEE Trans. Veh. Technol.*, vol. 68, no. 7, pp. 6535–6546, 2019.

[34] Y. Sun *et al.*, "Optimal 3D-trajectory design and resource allocation for solar-powered UAV communication systems," *IEEE Trans. Commun.*, vol. 67, no. 6, pp. 4281–4298, 2019.

[35] A. Al-Hourani *et al.*, "Optimal LAP altitude for maximum coverage," *IEEE Commun. Lett.*, vol. 3, no. 6, pp. 569–572, 2014.

[36] S. Sekander, H. Tabassum, and E. Hossain, "Statistical performance modeling of solar and wind-powered UAV communications," *IEEE Trans. Mob. Comput.*, vol. 20, no. 8, pp. 2686–2700, 2021.

[37] Y. Zhou, Z. Gu, J. Zhang, and Y. Ji, "Efficient deployment of aerial relays in FSO-based backhaul networks," *J. Opt. Commun. Netw.*, vol. 15, no. 1, pp. 29–42, 2023.

[38] Y. L. Che, W. Long, S. Luo, K. Wu, and R. Zhang, "Energy-efficient UAV multicasting with simultaneous FSO backhaul and power transfer," *IEEE Commun. Lett.*, vol. 10, no. 7, pp. 1537–1541, 2021.

[39] M. T. Dabiri *et al.*, "Modulating retroreflector based free space optical link for UAV-to-ground communications," *IEEE Trans. Wireless Commun.*, vol. 21, no. 10, pp. 8631–8645, 2022.

[40] B. Tezergil and E. Onur, "Wireless backhaul in 5G and beyond: Issues, challenges and opportunities," *IEEE Commun. Surv. Tutor.*, vol. 24, no. 4, pp. 2579–2632, 2022.

[41] M. M. Azari, F. Rosas, K.-C. Chen, and S. Pollin, "Optimal UAV positioning for terrestrial-aerial communication in presence of fading," in *2016 IEEE Global Communications Conference (GLOBECOM)*, pp. 1–7, 2016.

[42] N. Elmeseiry, N. Alshaer, and T. Ismail, "A detailed survey and future directions of unmanned aerial vehicles (UAVs) with potential applications," *Aerospace*, vol. 8, no. 12, 2021.

[43] J. Wu, H. Wang, Y. Huang, Z. Su, and M. Zhang, "Energy management strategy for solar-powered uav long-endurance target tracking," *IEEE Transactions on Aerospace and Electronic Systems*, vol. 55, no. 4, pp. 1878–1891, 2019.

[44] M. Ageev and D. Blidberg, "Current progress in the development of a solar powered autonomous underwater vehicle (auv)," in *Proceedings of 1998 International Symposium on Underwater Technology*, pp. 145–149, 1998.

[45] N. Wang, Y. Zhu, W. Wei, J. Chen, S. Liu, P. Li, and Y. Wen, "One-to-multipoint laser remote power supply system for wireless sensor networks," *IEEE Sensors Journal*, vol. 12, no. 2, pp. 389–396, 2012.

[46] M.-A. Lahmeri, M. A. Kishk, and M.-S. Alouini, "Stochastic geometry-based analysis of airborne base stations with laser-powered uavs," *IEEE Communications Letters*, vol. 24, no. 1, pp. 173–177, 2020.

[47] S. Sepehrvand, L. N. Theagarajan, and S. Hranilovic, "Rate-power trade-off in simultaneous lightwave information and power transfer systems," *IEEE Communications Letters*, vol. 25, no. 4, pp. 1249–1253, 2021.

[48] Y. L. Che, W. Long, S. Luo, K. Wu, and R. Zhang, "Energy-efficient uav multicasting with simultaneous fso backhaul and power transfer," *IEEE Wireless Communications Letters*, vol. 10, no. 7, pp. 1537–1541, 2021.

[49] X. Yao, F. Wang, J. Wang, and X. Wang, "Bilevel optimization-based time-optimal path planning for auvs," *Sensors*, vol. 18, no. 12, p. 4167, 2018.

[50] A. A. R. Al Makdah, N. Daher, D. Asmar, and E. Shammas, "Three-dimensional trajectory tracking of a hybrid autonomous underwater vehicle in the presence of underwater current," *Ocean Engineering*, vol. 185, pp. 115–132, 2019.

[51] H. Nam, "Data-gathering protocol-based auv path-planning for long-duration cooperation in underwater acoustic sensor networks," *IEEE Sensors Journal*, vol. 18, no. 21, pp. 8902–8912, 2018.

[52] J. Lyu, Y. Zeng, R. Zhang, and T. J. Lim, "Placement optimization of UAV-mounted mobile base stations," *IEEE Commun. Lett*, vol. 21, no. 3, pp. 604–607, 2017.

[53] S. Das, E. Poves, J. Fakidis, A. Sparks, S. Videv, and H. Haas, "Towards energy neutral wireless communications: Photovoltaic cells to connect remote areas," *Energies*, vol. 12, no. 19, p. 3772, 2019.

[54] A. M. Bagher, M. M. A. Vahid, and M. Mohsen, "Types of solar cells and application," *American Journal of optics and Photonics*, vol. 3, no. 5, pp. 94–113, 2015.

[55] M. Yamaguchi, "High-efficiency gaas-based solar cells," in *Post-Transition Metals* (M. M. Rahman, A. M. Asiri, A. Khan, Inamuddin, and T. Tabbakh, eds.), ch. 7, Rijeka: IntechOpen, 2020.

[56] A. Jenkins, "The sun's position in the sky," *European Journal of Physics*, vol. 34, pp. 633 – 652, 2012.

[57] S. C. Arum, D. Grace, P. D. Mitchell, M. D. Zakaria, and N. Morozs, "Energy management of solar-powered aircraft-based high altitude platform for wireless communications," *Electronics*, vol. 9, no. 1, p. 179, 2020.

[58] J.-S. Lee and K.-H. Yu, "Optimal path planning of solar-powered UAV using gravitational potential energy," *IEEE Trans. Aerosp. Electron. Syst.*, vol. 53, no. 3, pp. 1442–1451, 2017.

[59] M. Paulescu, E. Paulescu, P. Gravila, and V. Badescu, *Modeling Solar Radiation at the Earth Surface*, pp. 127–179. London: Springer London, 2013.

[60] G. G. Hahn, L. A. Adoram-Kershner, H. P. Cantin, and M. W. Shafer, "Assessing solar power for globally migrating marine and submarine systems," *IEEE Journal of Oceanic Engineering*, vol. 44, no. 3, pp. 693–706, 2018.

[61] J. Lin, Z. Du, C. Yu, W. Ge, W. Lü, H. Deng, C. Zhang, X. Chen, Z. Zhang, and J. Xu, "Machine-vision-based acquisition, pointing, and tracking system for underwater wireless optical communications," *Chin. Opt. Lett.*, vol. 19, p. 050604, May 2021.

[62] M.-A. Lahmeri, M. A. Kishk, and M.-S. Alouini, "Laser-powered uavs for wireless communication coverage: A large-scale deployment strategy," *IEEE Transactions on Wireless Communications*, vol. 22, no. 1, pp. 518–533, 2023.

[63] P. G. Duynkerke and P. Hignett, "Simulation of diurnal variation in a stratocumulus-capped marine boundary layer during fire," *Monthly weather review*, vol. 121, no. 12, pp. 3291–3300, 1993.

[64] H. G. Sandalidis, A. Vavoulas, T. A. Tsiftsis, and N. Vaiopoulos, "Illumination, data transmission, and energy harvesting: the threefold advantage of vlc," *Appl. Opt.*, vol. 56, pp. 3421–3427, Apr 2017.

[65] P. D. Diamantoulakis and G. K. Karagiannidis, "Simultaneous lightwave information and power transfer (slipt) for indoor iot applications," in *GLOBECOM 2017-2017 IEEE Global Communications Conference*, pp. 1–6, IEEE, 2017.

[66] G. Pan, P. D. Diamantoulakis, Z. Ma, Z. Ding, and G. K. Karagiannidis, "Simultaneous lightwave information and power transfer: Policies, techniques, and future directions," *IEEE Access*, vol. 7, pp. 28250–28257, 2019.

[67] Z. Wang, D. Tsonev, S. Videv, and H. Haas, "On the design of a solar-panel receiver for optical wireless communications with simultaneous energy harvesting," *IEEE Journal on Selected areas in Communications*, vol. 33, no. 8, pp. 1612–1623, 2015.

[68] A. Phillips, M. Haroutunian, A. J. Murphy, S. Boyd, J. Blake, and G. Griffiths, "Understanding the power requirements of autonomous underwater systems, part i: An analytical model for optimum swimming speeds and cost of transport," *Ocean Engineering*, vol. 133, pp. 271–279, 2017.

[69] M. E. Furlong, S. D. McPhail, and P. Stevenson, "A concept design for an ultra-long-range survey class auv," in *OCEANS 2007-Europe*, pp. 1–6, IEEE, 2007.

[70] J. G. Bellingham and J. S. Willcox, "Optimizing auv oceanographic surveys," in *Proceedings of Symposium on Autonomous Underwater Vehicle Technology*, pp. 391–398, IEEE, 1996.

[71] C. D. Mobley, B. Gentili, H. R. Gordon, Z. Jin, G. W. Kattawar, A. Morel, P. Reinersman, K. Stamnes, and R. H. Stavn, "Comparison of numerical models for computing underwater light fields," *Applied Optics*, vol. 32, no. 36, pp. 7484–7504, 1993.

[72] A. A. Farid and S. Hranilovic, "Upper and lower bounds on the capacity of wireless optical intensity channels," in *2007 IEEE International Symposium on Information Theory*, pp. 2416–2420, IEEE, 2007.

[73] J.-B. Wang, Q.-S. Hu, J. Wang, M. Chen, and J.-Y. Wang, "Tight bounds on channel capacity for dimmable visible light communications," *Journal of Lightwave Technology*, vol. 31, no. 23, pp. 3771–3779, 2013.

[74] X. Chen, Y. Liu, X. Li, Z. Wang, S. Wang, and C. Gao, "A new evolutionary multiobjective model for traveling salesman problem," *IEEE Access*, vol. 7, pp. 66964–66979, 2019.

[75] V. Dwivedi, T. Chauhan, S. Saxena, and P. Agrawal, "Travelling salesman problem using genetic algorithm," *IJCA proceedings on development of reliable information systems, techniques and related issues (DRISTI 2012)*, vol. 1, p. 25, 2012.

[76] J.-S. Lee and K.-H. Yu, "Optimal path planning of solar-powered uav using gravitational potential energy," *IEEE Transactions on Aerospace and Electronic Systems*, vol. 53, no. 3, pp. 1442–1451, 2017.

[77] M. Elamassie, F. Miramirkhani, and M. Uysal, "Channel modeling and performance characterization of underwater visible light communications," in *2018 IEEE International Conference on Communications Workshops (ICC Workshops)*, pp. 1–5, IEEE, 2018.

[78] "http://www.teledynemarine.com/gavia-auv?brandid=9."

[79] H. Nam, "Data-gathering protocol-based auv path-planning for long-duration cooperation in underwater acoustic sensor networks," *IEEE sensors journal*, vol. 18, no. 21, pp. 8902–8912, 2018.

[80] N. Javaid, N. Ilyas, A. Ahmad, N. Alrajeh, U. Qasim, Z. A. Khan, T. Liaqat, and M. I. Khan, "An efficient data-gathering routing protocol for underwater wireless sensor networks," *Sensors*, vol. 15, no. 11, pp. 29149–29181, 2015.

[81] A. Ahmad, A. Wahid, and D. Kim, "Aeerp: Auv aided energy efficient routing protocol for underwater acoustic sensor network," in *Proceedings of the 8th ACM workshop on Performance monitoring and measurement of heterogeneous wireless and wired networks*, pp. 53–60, 2013.

[82] N. Wang and J. Wu, "Trajectory scheduling for timely data report in underwater wireless sensor networks," in *2015 IEEE Global Communications Conference (GLOBECOM)*, pp. 1–6, IEEE, 2015.

[83] N. Ilyas, N. Javaid, Z. Iqbal, M. Imran, Z. A. Khan, U. Qasim, and M. Shoaib, "Aaeerp: Advanced auv-aided energy efficient routing protocol for underwater wsns," in *2015 IEEE 29th International Conference on Advanced Information Networking and Applications*, pp. 77–83, IEEE, 2015.

[84] X. Zhuo, M. Liu, Y. Wei, G. Yu, F. Qu, and R. Sun, "Auv-aided energy-efficient data collection in underwater acoustic sensor networks," *IEEE Internet of Things Journal*, vol. 7, no. 10, pp. 10010–10022, 2020.

[85] C. Qin, J. Du, J. Wang, and Y. Ren, "A hierarchical information acquisition system for auv assisted internet of underwater things," *IEEE Access*, vol. 8, pp. 176089–176100, 2020.

[86] F. A. Khan, S. A. Khan, D. Turgut, and L. Bölöni, "Scheduling multiple mobile sinks in underwater sensor networks," in *2015 IEEE 40th Conference on Local Computer Networks (LCN)*, pp. 149–156, IEEE, 2015.

[87] G. A. Hollinger, S. Choudhary, P. Qarabaqi, C. Murphy, U. Mitra, G. S. Sukhatme, M. Stojanovic, H. Singh, and F. Hover, "Underwater data collection using robotic sensor networks," *IEEE Journal on Selected Areas in Communications*, vol. 30, no. 5, pp. 899–911, 2012.

[88] P. Gjanci, C. Petrioli, S. Basagni, C. A. Phillips, L. Bölöni, and D. Turgut, "Path finding for maximum value of information in multi-modal underwater wireless sensor networks," *IEEE Transactions on Mobile Computing*, vol. 17, no. 2, pp. 404–418, 2017.

[89] P. P. Jenkins, S. Messenger, K. M. Trautz, S. I. Maximenko, D. Goldstein, D. Scheiman, R. Hoheisel, and R. J. Walters, "High-bandgap solar cells for underwater photovoltaic applications," *IEEE Journal of Photovoltaics*, vol. 4, no. 1, pp. 202–207, 2013.

[90] "https://evologics.de/."

[91] "https://www.km.kongsberg.com/ks/web/nokbg0240.nsf."

[92] Y. Weng, T. Matsuda, Y. Sekimori, J. Pajarinen, J. Peters, and T. Maki, "Pointing error control of underwater wireless optical communication on mobile platform," *IEEE Photonics Technology Letters*, vol. 34, no. 13, pp. 699–702, 2022.

[93] X. Yao, F. Wang, J. Wang, and X. Wang, "Bilevel optimization-based time-optimal path planning for auvs," *Sensors*, vol. 18, no. 12, p. 4167, 2018.

[94] M. E. Furlong, S. D. McPhail, and P. Stevenson, "A concept design for an ultra-long-range survey class auv," in *OCEANS 2007-Europe*, pp. 1–6, IEEE, 2007.

[95] Y. Song, H. Ye, Y. Wang, W. Niu, X. Wan, and W. Ma, "Energy consumption modeling for underwater gliders considering ocean currents and seawater density variation," *Journal of Marine Science and Engineering*, vol. 9, no. 11, 2021.

[96] A. Phillips, M. Haroutunian, A. J. Murphy, S. Boyd, J. Blake, and G. Griffiths, "Understanding the power requirements of autonomous underwater systems, part i: An analytical model for optimum swimming speeds and cost of transport," *Ocean Engineering*, vol. 133, pp. 271–279, 2017.

[97] X. Sun, C. H. Kang, M. Kong, O. Alkhazragi, Y. Guo, M. Ouhssain, Y. Weng, B. H. Jones, T. K. Ng, and B. S. Ooi, "A review on practical considerations and solutions in underwater wireless optical communication," *Journal of Lightwave Technology*, vol. 38, no. 2, pp. 421–431, 2020.

[98] J. Lin, Z. Du, C. Yu, W. Ge, W. Lü, H. Deng, C. Zhang, X. Chen, Z. Zhang, and J. Xu, "Machine-vision-based acquisition, pointing, and tracking system for underwater wireless optical communications," *Chin. Opt. Lett.*, vol. 19, p. 050604, May 2021.

[99] R. Jiang, Z. Wang, Q. Wang, and L. Dai, "A tight upper bound on channel capacity for visible light communications," *IEEE Communications Letters*, vol. 20, no. 1, pp. 97–100, 2015.

[100] C. D. Mobley, B. Gentili, H. R. Gordon, Z. Jin, G. W. Kattawar, A. Morel, P. Reinersman, K. Stamnes, and R. H. Stavn, "Comparison of numerical models for computing underwater light fields," *Applied Optics*, vol. 32, no. 36, pp. 7484–7504, 1993.

[101] J. Stastnỳ, V. Skorpil, and L. Cizek, "Traveling salesman problem optimization by means of graph-based algorithm," in *2016 39th International Conference on Telecommunications and Signal Processing (TSP)*, pp. 207–210, IEEE, 2016.

[102] Z. Zeng, A. Lammas, K. Sammut, and F. He, "Optimal path planning based on annular space decomposition for auvs operating in a variable environment," in *2012 IEEE/OES Autonomous Underwater Vehicles (AUV)*, pp. 1–9, IEEE, 2012.

[103] L. Wang, L. Liu, J. Qi, and W. Peng, "Improved quantum particle swarm optimization algorithm for offline path planning in auvs," *IEEE Access*, vol. 8, pp. 143397–143411, 2020.

[104] Y.-N. Ma, Y.-J. Gong, C.-F. Xiao, Y. Gao, and J. Zhang, "Path planning for autonomous underwater vehicles: An ant colony algorithm incorporating alarm pheromone," *IEEE Transactions on Vehicular Technology*, vol. 68, no. 1, pp. 141–154, 2019.

[105] D. Corus and P. S. Oliveto, "Standard steady state genetic algorithms can hillclimb faster than mutation-only evolutionary algorithms," *IEEE Transactions on Evolutionary Computation*, vol. 22, no. 5, pp. 720–732, 2017.

[106] "https://www.uav-instruments.com/."

[107] M. Arima, T. Okashima, and T. Yamada, "Development of a solar-powered underwater glider," in *2011 IEEE Symposium on Underwater Technology and Workshop on Scientific Use of Submarine Cables and Related Technologies*, pp. 1–5, 2011.

[108] N. Elmeseiry, N. Alshaer, and T. Ismail, "A detailed survey and future directions of unmanned aerial vehicles (UAVs) with potential applications," *Aerospace*, vol. 8, no. 12, 2021.

[109] M. Mozaffari *et al.*, "A tutorial on UAVs for wireless networks: Applications, challenges, and open problems," *IEEE Commun. Surv. Tutor.*, vol. 21, no. 3, pp. 2334–2360, 2019.

[110] Y. Zeng, J. Xu, and R. Zhang, "Energy minimization for wireless communication with rotary-wing uav," *IEEE Transactions on wireless communications*, vol. 18, no. 4, pp. 2329–2345, 2019.

[111] P. Bhardwaj and S. M. Zafaruddin, "Performance of dual-hop relaying for THz-RF wireless link over asymmetrical α-μ fading," *EEE Trans. Veh. Technol.*, vol. 70, no. 10, pp. 10031–10047, 2021.

[112] C. Peng, J. Wang, and D. Wu, "Impacts of air density fluctuations toward the mass measurements of a 1 kg silicon sphere," *IEEE Access*, vol. 8, pp. 140840–140847, 2020.

[113] R. Series, "Propagation data and prediction methods required for the design of terrestrial line-of-sight systems," *Recommendation ITU-R*, pp. 530–12, 2015.

[114] E. M. Sozer, M. Stojanovic, and J. G. Proakis, "Underwater acoustic networks," *IEEE journal of oceanic engineering*, vol. 25, no. 1, pp. 72–83, 2000.

[115] "https://www.alibaba.com/product-detail/gallium-arsenide-solar-cells [accessed january 23, 2023]."

[116] "https://www.aeroexpo.online/prod/slidx/product-175273-15858.html [accessed june 30, 2022]."

[117] "http/softbank's next-generation battery development — softbank research institute of advanced technology — about us — softbank."

[118] Ö. Dündar, M. Bilici, and T. Ünler, "Design and performance analyses of a fixed wing battery vtol uav," *Engineering Science and Technology, an International Journal*, vol. 23, no. 5, pp. 1182–1193, 2020.

[119] Y. Zeng and R. Zhang, "Energy-efficient uav communication with trajectory optimization," *IEEE Transactions on Wireless Communications*, vol. 16, no. 6, pp. 3747–3760, 2017.

[120] A. Lapidoth, S. M. Moser, and M. A. Wigger, "On the capacity of free-space optical intensity channels," *IEEE Transactions on Information Theory*, vol. 55, no. 10, pp. 4449–4461, 2009.

VITA

Khadijeh Ali Mahmoodi began her academic journey at the Optoelectronics and Optical Communications Research Laboratory (OOCRL) research center in 2016, where she pursued her M.Sc. degree in electrical and electronics engineering at Isfahan University of Technology, Isfahan, Iran. Under the supervision of Dr. Gholami and co-supervision of Professor Zabih Ghassemlooy, she delved into the fascinating world of research. In 2019, Khadijeh successfully completed her M.Sc., marking a significant milestone in her academic pursuits.

Seeking new challenges and opportunities, Khadijeh's passion for advancing communication technologies led her to join the Communication Theory and Technologies (CT&T) Research Group in 2020. At Ozyegin University, located in the vibrant city of Istanbul, Turkiye, she embarked on a Ph.D. journey under the mentorship of Professor Murat Uysal. Here, she further honed her research skills and contributed to cutting-edge developments in the field.

In addition to her academic endeavors, Khadijeh is also actively involved in the prestigious ENLIGHTEM project, where she serves as a Marie Curie Early-Stage Researcher. This remarkable opportunity has allowed her to collaborate with leading experts and researchers, broadening her perspective and fostering international collaboration.

Khadijeh's research interests encompass a diverse range of topics within the realm of communication networks. She is particularly fascinated by low-energy visible light communication systems, underwater sensor networks, energy harvesting techniques, and the optimization of trajectories for AUVs and UAVs in communication networks.